

Two-dimensional Bose-Einstein Condensate in an optical surface trap

Dissertation

zur Erlangung des Doktorgrades an der
naturwissenschaftlichen Fakultät
der Leopold-Franzens-Universität Innsbruck

vorgelegt von

David Rychtařík

aus Rakovnik

durchgeführt am Institut für Experimentalphysik
unter der Leitung von
Univ.-Prof. Dr. Rudolf Grimm

April 2004

Abstract

This thesis reports on the realization of a two-dimensional Bose-Einstein Condensate of cesium atoms in an optical surface trap, where the condensate is produced a few micrometers above a dielectric surface.

The optical trap is a combination of a repulsive evanescent wave created on a horizontal dielectric surface and a focussed 1064 nm-laser beam. Vertically the atoms are confined by a combination of the optical and gravitational potential, horizontally by the 1064 nm light. To load the surface trap we release the cesium atoms from a magneto-optical trap into the gravito-optical surface trap which first prepares a cold atom reservoir. The atoms are then loaded by thermalization into the conservative trap potential generated by the red-detuned 1064 nm laser beam. After loading we optically pump the atoms in the lowest spin state $F = 3, m_F = 3$, where cesium offers very favorable scattering properties and the scattering length can be tuned to positive values. To introduce forced evaporative cooling we ramp down the power of the red-detuned beam from 5 W by more than three orders of magnitude to a few milliwatts within 5 seconds.

After the evaporation we observe a vertical release energy of $\frac{1}{2}k_B \times 16$ nK which is well below the vibrational energy quantum $\hbar\omega = k_B \times 26$ nK and close to the zero point energy of $\frac{1}{2}\hbar\omega$. Thus a two-dimensional gas is realized. To prove the presence of a condensate we use a method which relies on a controlled collapse of the condensate when the scattering length is tuned to negative values. A second method relies on the horizontal expansion of the sample which is slowed down when a condensate is present.

With these two methods we can observe the onset of condensation. We observe the transition at approximately 100 nK in a 3D regime, where about 5 quantum states of the vertical motion are occupied. For lower final values of the evaporation a two-dimensional condensate is realized. The vertical motion is then dominated by the zero-point energy.

Zusammenfassung

Im Rahmen dieser Arbeit berichte ich über die Realisierung eines zwei-dimensionalen Bose-Einstein Kondensats in einer optischen Oberflächenfalle, in der die Atome wenige Mikrometer über der dielektrischen Oberfläche gefangen werden.

Die Oberflächenfalle ist eine Kombination aus einer repulsiven evaneszenten Lichtwelle auf einer horizontalen dielektrischen Oberfläche und einem fokussierten 1064 nm Laser, der für den horizontalen Einschluß sorgt. Vertikal werden die Atome durch eine Kombination aus dem optischen Potential und der Gravitation gehalten. In einer magneto-optischen Falle werden die Atome zuerst gefangen, dann in die gravito-optische Oberflächenfalle transferiert, die dann als Reservoir mit kalten Atomen dicht über der Oberfläche dient. Das konservative Potential der Mikrofalle wird über elastische Stöße mit Atomen aus dem Reservoir geladen. Um die günstigen Streueigenschaften der Cäsiumatome ausnutzen zu können, die Größe und das Vorzeichen der Streulänge ändern zu können, werden die Atome in den tiefsten Spinzustand $F = 3, m_F = 3$ gepumpt. Danach wird 5 Sekunden lang evaporativ gekühlt, indem man die Leistung des rot-verstimmten Lasers von 5 W um mehr als drei Dekaden bis auf wenige mW absenkt.

Am Ende der Evaporation beobachten wir eine vertikale Expansionsenergie von $\frac{1}{2}k_B \times 16$ nK, die deutlich unterhalb der Energie des Vibrationsquantums $\hbar\omega = k_B \times 26$ nK und sehr nah an der Grundzustandsenergie $\frac{1}{2}\hbar\omega$ liegt, was eindeutig die Realisierung eines zwei-dimensionalen Quantengases zeigt. Um zu zeigen, daß es sich bei diesem Quantengas auch um ein Kondensat handelt, haben wir die Eigenschaft des Kondensats ausgenutzt, bei einer negativen Streulänge zu kolabieren. Eine zweite Nachweismethode beruht auf Messungen der horizontalen Expansion, bei denen die Expansion für eine kondensierte Wolke deutlich langsamer von statten geht.

Mit diesen beiden Methoden sind wir in der Lage die Bedingungen auszumessen, unter welchen die Kondensation stattfindet. Wir beobachten, daß die Atome bei einer Temperatur von etwa 100 nK anfangen zu kondensieren. Dabei sind etwa 5 Quantenzustände der vertikalen Bewegung besetzt, so daß der Phasenübergang im 3D-Regime stattfindet, erst bei einer weiteren Absenkung des horizontalen Potentials wird das Regime der Zwei-Dimensionalität erreicht, in welchem die vertikale Bewegung durch die Grundzustandsenergie gegeben ist.

Contents

| | | |
|----------|---|-----------|
| 1 | Introduction | 9 |
| 2 | Bose-Einstein Condensation and the Cesium Atom | 11 |
| 2.1 | Bose-Einstein Condensation | 11 |
| 2.1.1 | Basic Features | 12 |
| 2.1.2 | Bose-Einstein Condensation of a Trapped Ideal Gas | 15 |
| 2.1.3 | Collapse of a Condensate | 18 |
| 2.2 | Ultracold Gases in 2D | 19 |
| 2.2.1 | Crossover into the 2D-regime | 19 |
| 2.2.2 | Bose-Einstein Condensation | 20 |
| 2.3 | Cesium Atom | 23 |
| 2.3.1 | Basic Properties | 23 |
| 2.3.2 | Long way to the first cesium BEC | 24 |
| 2.3.3 | Cesium Specialities | 24 |
| 2.3.4 | Feshbach Resonances | 26 |
| 3 | Theoretical background | 29 |
| 3.1 | Optical Dipole Force | 29 |
| 3.2 | Evanescant Waves | 33 |
| 3.3 | Magnetic Force | 38 |
| 3.4 | Inelastic Collisions | 39 |
| 3.4.1 | Two-body Collisions | 39 |
| 3.4.2 | Three-body Recombination | 41 |
| 3.5 | Evaporative cooling | 43 |
| 3.5.1 | Plain and Forced Evaporation | 43 |
| 3.5.2 | Evaporation Efficiency | 45 |
| 3.5.3 | Dimensionality of the Evaporation | 46 |
| 4 | Experimental Setup | 48 |
| 4.1 | Vacuum System | 48 |
| 4.2 | Magnetic Fields | 50 |

| | | |
|----------|--|------------|
| 4.3 | Laser Setup | 51 |
| 4.3.1 | MOT Lasers | 51 |
| 4.4 | The Gravitational-optical Surface Trap | 54 |
| 4.5 | Dimple Trap | 57 |
| 5 | Trap Properties and Measurement Procedures | 60 |
| 5.1 | Gravitational-optical Surface Trap | 60 |
| 5.2 | Dimple trap | 65 |
| 5.2.1 | The Dimple Trick and Loading the Dimple Trap | 65 |
| 5.2.2 | Ensemble Properties | 69 |
| 5.2.3 | Storage | 70 |
| 5.3 | Measurement Procedures | 72 |
| 5.3.1 | Experimental Control | 72 |
| 5.3.2 | Measurement Cycle | 72 |
| 5.3.3 | Atom Number Measurement | 73 |
| 5.3.4 | Temperature Measurement | 74 |
| 5.3.5 | Trap Frequencies | 78 |
| 5.3.6 | Polarized Atoms | 80 |
| 5.4 | Important Tools | 83 |
| 5.4.1 | Levitation | 83 |
| 5.4.2 | Feshbach Spectroscopy | 86 |
| 6 | Bose-Einstein Condensate in a highly anisotropic Surface Trap | 89 |
| 6.1 | Evaporative cooling | 89 |
| 6.2 | Two-dimensionality | 93 |
| 6.3 | Bose-Einstein condensation | 95 |
| 6.4 | Limitations | 105 |
| 6.4.1 | Evanescence Wave | 106 |
| 6.4.2 | Magnetic Field | 107 |
| 7 | Outlook | 109 |
| 7.1 | Technical Improvements | 109 |
| 7.2 | Future Experiments | 111 |
| | References | 114 |

Chapter 1

Introduction

In 1995, seven decades after Einstein's theoretical predictions, Bose-Einstein condensation (BEC) in a dilute atomic gas of rubidium was observed for the first time [And95]. Within a few months BEC in sodium was observed [Dav95] while and lithium followed shortly later [Bra95, Bra97]. These achievements attracted substantial attention both in the scientific community and the mass media who celebrated BEC as a “new state of matter”.

Since its conception, BEC has been observed by approximately 40 groups around the world in all stable alkalis [And95, Bra95, Cor00, Mod01, Web03a], hydrogen [Fri98b], metastable helium [Rob01a] and ytterbium [Tak03]. Very recently a molecular BEC of lithium and potassium molecules has been achieved [Joc03, Gre03]. The realization of a BEC enables the experimentalists to investigate novel effects such as superfluidity or coherent states of matter. In many experiments [And97] the BEC serves as a source of coherent matter waves. Interferometry setups are used to probe the condensate coherence length [Blo00], to give a signature for the Mott insulator in an optical lattice [Gre02] and to test the restricted geometry effect in a form of phase fluctuations [Det01].

In condensed matter physics a two-dimensional electron gas is a system leading a young and exciting research field where new effects such as fractional quantum hall effect [HS82] can be observed. Furthermore, new avenues in cold atom physics are being opened up due to the reduced dimension.

Earlier discussions of low-dimensional Bose gases were mostly academic because there was no possibility to realize such a system. However, the fast progress in the field of cold atoms and the observation of BEC stimulated a search for non-trivial trapping geometries. The present experiments, with special potential shapes, allow the production of dilute and cold gases in highly anisotropic configurations where the motion of the atoms is reduced to one or two directions - the strongly confined directions are “frozen out” and the particles undergo zero point oscillations. The presence of shallow confinement in the other direction(s) allows us to speak of a trapped 1D or 2D gas. The regimes of 1D or 2D degenerated quantum gases are drastically different from those in 3D. New phe-

nomena such as modified scattering properties have been predicted for low-dimensional quantum gases [Pet00]. Due to phase-fluctuations a BEC does not occur in 1D or 2D at any finite temperature, however a trapping potential leading to a finite sample size enables a realization of a condensate at a finite particle number [Ket96].

The first experiments investigating 2D dilute atomic systems were performed with spin-polarized hydrogen on a liquid-helium surface. In 1998 the first evidence for quantum degeneracy was the observation of a significant reduction in the three-body recombination probability. These results have been interpreted as a realization of a quasicondensate (BEC with fluctuating phase) [Saf98, Pet00]. A pure BEC in 1D and 2D was observed in 2001 [Gör01, Sch01]. In [Gör01] a 3D sodium BEC was first created in a magnetic trap and then transferred into a highly anisotropic disk-shaped optical trap. The 2D BEC was observed by a change in aspect ratio in expansion measurements at the crossover to the 2D-regime.

Other approaches to the realization of 2D confinement include integrated atomic optics [Fol00] and evanescent-wave traps. The magnetic microtraps are based on current-carrying micro-wires producing large magnetic gradients. They have been successfully used to produce BEC in quasi-1D geometries [Hän01b, Ott01]. Compared to magnetic traps, optical surface traps do not suffer from heating produced by the proximity of the magnetic fields above the metallic surface [For02]. An inhomogeneous optical surface trap in one direction is produced by a combination of a red- and blue-detuned evanescent waves. This scheme was proposed in 1991 [Ovc91] and an atomic gas close to two-dimensionality first was realized in 2002 [Ham02a]. Another favorable scheme for 2D-trapping is a surface trap using a combination of an evanescent wave and a laser beam for horizontal confinement [Ham02b].

In this work I will show how such an optical surface trap can be realized and which conditions have to be fulfilled in order to reach the quantum degeneracy regime in 2D. After evaporative cooling in the surface trap we observe release energies well below the vibrational energy quantum. We develop new techniques to prove the presence of the condensate. We have chosen a particular atom, cesium, with which to do our experiments and which, for the first time in 2002 [Web03a], formed a Bose-Einstein condensate. Cesium seemed, for a long time, to be a promising candidate for reaching quantum degeneracy but, due to its particular scattering properties, it was the last stable alkali atom which formed a condensate. To date, cesium has only formed a condensate in the absolute ground state while trapped in an optical trap.

The second Chapter will deal with theory of BEC, both in the three-dimensional and the two-dimensional regime before Chapter 3 describes the theory needed to understand the trap scheme and processes such as collisions and evaporative cooling. Chapter 4 describes the experimental setup and Chapter 5 introduces the properties of the trapped sample and the measurement procedures used in the experiment. Chapter 6 discusses the measurements related to the realization of a two-dimensional BEC before an outlook will be given in Chapter 7.

Chapter 2

Bose-Einstein Condensation and the Cesium Atom

In this chapter I will give a brief introduction into Bose Einstein condensation. First I will introduce the fundamental characteristics of a three-dimensional Bose-Einstein condensate before investigating the two-dimensional regime. Finally, I will describe the basic properties of the cesium atom and present the reasons why it is so difficult to create a condensate from cesium atoms. For further details of BEC theory and the appropriate experiments I refer the reader to the review articles and textbooks [Ket99, Dal99a, Pet02, Bon02].

2.1 Bose-Einstein Condensation

In 1924 Satyendranath Bose described black-body radiation statistically and one year later Albert Einstein generalized this theory for material particles. The result was Bose-Einstein statistics. Although the quantum theory had not been fully developed at this time while also the differences between bosons and fermions had not been revealed, the phenomenon of Bose-Einstein condensation was predicted. For a long time, there were no opportunity to observe this phenomena because the necessary temperature-density combination could not be experimentally achieved. It took 70 years until the combination of laser and evaporative cooling made the first Bose-Einstein Condensation (BEC) in a dilute atomic vapor of Rb-87 [And95] possible. Since then more than thirty groups in the world have created BEC, all stable alkali atoms, and have investigated this state extensively. The initial pioneering groups were awarded the Nobel Prize in Physics in 2001 for the first creation and observation of such a state of matter. Bose-Einstein condensation of dilute gas doesn't only confirm quantum statistics, but it also opens new windows in experimental physics for example, investigation of fundamental phenomena like bosonic stimulation, coherence, suprafluidity and many others.

In the recent years, degenerate quantum gases in lower dimensions (less than three) have attracted considerable interest since experiments demonstrating trapping schemes in which it is possible to study quantum gases with reduced dimensionality. A 1D or 2D degenerate gas exhibits many new effects which do not occur in a three-dimensional system.

In the following section I will first give a short overview about the phenomena Bose-Einstein condensation before I treating an ideal gas theoretically while also explaining some special features such as the collapse of a condensate. Finally, I will introduce BECs with reduced dimensionality while explaining details concerning the 2D-regime.

2.1.1 Basic Features

BEC is a consequence of quantum statistical mechanics and is based on the wave nature of the particles and their indistinguishability. The wave nature of particles can be explained in a simplified picture where the atoms are considered as quantum-mechanical wave packets with an extension in the order of the thermal de-Broglie wavelength

$$\lambda_{dB} = \sqrt{\frac{2\pi\hbar^2}{mk_B T}}, \quad (2.1)$$

where T is the temperature and m the mass of the atom. λ_{dB} can be regarded as the position uncertainty associated with the thermal momentum distribution. The wavelength of the particle is inversely proportional to temperature. If an ensemble is cooled to a point where the distance between the atoms is comparable to the de-Broglie wavelength, the wavepackets begin to overlap in space. At this point the atoms undergo a phase transition and form a Bose-Einstein condensate. In order to describe the course of the condensation it is useful to introduce the *phase-space density*

$$D = n\lambda_{dB}^3 \quad (2.2)$$

which relates the density n to the volume λ_{dB}^3 occupied by an atom. The condensation transition occurs at $D \simeq 1$. This transition takes place only for particles with integer spin, known as *bosons*. In a BEC, at very high density and/or very low temperature, the separation of the atoms can be even smaller than λ_{dB} , in this case λ_{dB} can reach values up to a micrometer. But the largest scale of an atom is determined by the confinement, which can be characterized by the size of the ground state function $a_{ho} = \sqrt{\hbar/m\omega}$ in a harmonic potential with the frequency ω . The particle/wave nature of an atom and the condensation process is shown in figure 2.1.

To be able to calculate some important quantities characterizing the BEC one has to use the theory of quantum statistics. An important formula describing the behavior of non-interacting bosons in thermal equilibrium is the Bose-distribution

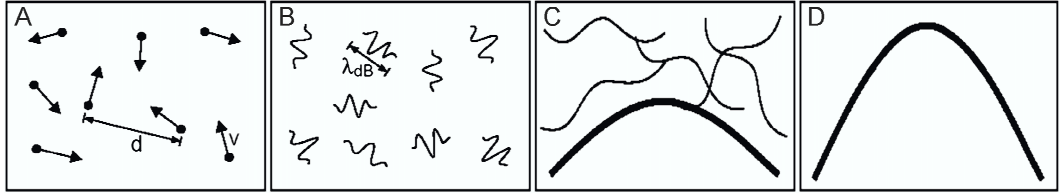


Figure 2.1: *Demonstrative description of a BEC. At high temperatures (A) the atoms in the weakly interacting gas can be treated as particles, whereas with lowering the temperature (B) the atoms develop a wavepacket character. When the temperature reaches the critical temperature (C) the de Broglie wave length becomes comparable with the distance between the atoms and the matter waves begin to overlap. For temperatures approaching zero (D), one obtains a pure condensate corresponding to a large matter wave.*

$$N_\nu = \frac{1}{e^{(\varepsilon_\nu - \mu)/(k_B T)} - 1}. \quad (2.3)$$

which gives the mean occupation number N_ν of a state ν with the energy ε_ν . The chemical potential μ of the atoms has to always stay below ε_ν to avoid negative occupation number. μ can be calculated in a given potential as a function of N and T . Condensation takes place when $\mu \rightarrow \varepsilon$, when the ground state occupation diverges. For decreasing temperature and fixed number of particles ($N = \sum_\nu N_\nu$) the chemical potential rises and for the limit $T \rightarrow 0$ $N_0 = N$ is expected. At high temperatures the mean occupation number N_ν of any single state is very small, since the high energy of the atoms allows them to reach higher levels and thus occupy many states.

The critical temperature T_c , where condensation occurs, can be calculated by the considering the number of particles occupying the excited states N_{ex} . When the temperature falls below T_c the maximum atom number $N_{ex,max} = \sum_1^\infty N(\mu_0 = \varepsilon_0)$ drops below N and the atoms enter the ground state. It is important to note that $k_B T_c$ is much higher than the energy quantum $\varepsilon_1 - \varepsilon_0$. This means that all atoms do not enter the ground state suddenly, but rather the fraction of atoms in the ground state increases with decreasing temperature.

After substituting the sum of the calculation of $N_{ex,max}$ by an integral over the density of states, which includes the shape of the potential, one can derive the critical temperature

$$T_c \approx 4.5 \left(\frac{\bar{\omega}/2\pi}{100 \text{ Hz}} \right) N^{1/3} \text{ nK}, \quad (2.4)$$

where $\bar{\omega} = \sqrt[3]{\omega_x \omega_y \omega_z}$ is the geometrically averaged trap frequency.

To calculate the critical phase-space density one has to use the formula 2.2, 2.4 and

the peak number density $\hat{n} = N\bar{\omega}^3(m/2\pi k_B T)^{3/2}$ for a thermal gas in a harmonic trap. We obtain the result that the BEC-transition occurs when the phase-space density of a sample in a harmonic trap reaches

$$D_c = N \left(\frac{\hbar\bar{\omega}}{k_B T} \right)^3 \approx 1.202 \quad (2.5)$$

This value is dependent from the shape of the potential, e.g. in a 3D box potential and for the free space we get $D_c \approx 2.612$.

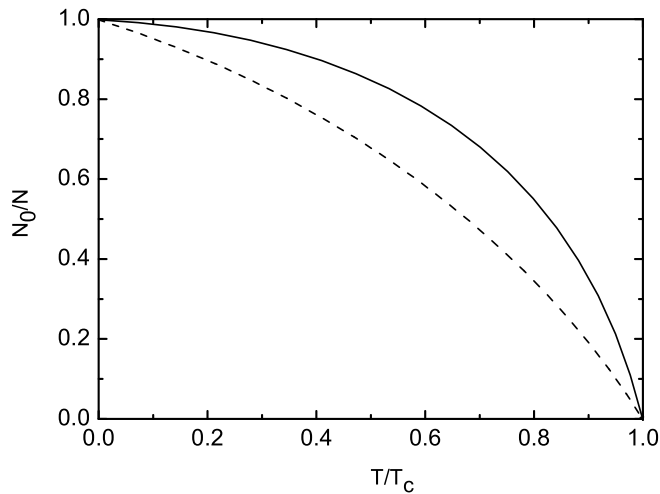


Figure 2.2: Comparison of the temperature dependence of ground state occupation below T_c for a BEC trapped in a box potential (dashed line) or in a harmonic potential (solid line).

Not only is the value of the critical phase-space density dependent on the shape of the potential, but also the evolution of the ground state population. Figure 2.2 shows the relative occupation of the ground state below T_c for two different potentials. The expression for the condensate fraction can be, for the case of an harmonic potential, written as

$$\frac{N_0}{N} = 1 - \left(\frac{T}{T_c} \right)^3. \quad (2.6)$$

As shown in figure 2.2 in the case of an harmonic potential, there is nearly 90% occupation of the the ground state at $T = T/2$ while at $T = 0$ all atoms are in the ground state. In potentials steeper than the harmonic example the occupation grows even faster. This can be explained by the fact that the larger slope leads to lower number of states at low energies.

2.1.2 Bose-Einstein Condensation of a Trapped Ideal Gas

Most condensates to date have been realized in a three-dimensional harmonic trapping potential

$$U(\vec{r}) = \frac{m}{2}(\omega_x^2 x^2 + \omega_y^2 y^2 + \omega_z^2 z^2). \quad (2.7)$$

To obtain the wave function one must solve the Schrödinger equation with the hamiltonian $H = -\hbar^2/(2m)\nabla^2 + U(\vec{r})$. This results in the ground state wavefunction

$$\Phi(\vec{r}) = \left(\frac{m\bar{\omega}}{\pi\hbar}\right)^{3/4} \exp\left(-\frac{m}{2\hbar}(\omega_x^2 x^2 + \omega_y^2 y^2 + \omega_z^2 z^2)\right). \quad (2.8)$$

with the geometric mean frequency $\bar{\omega} = \sqrt[3]{\omega_x\omega_y\omega_z}$. For an ideal gas this describes exactly the Bose-Einstein condensate wave function. The wavefunction has a gaussian profile and is given by the harmonic oscillator length $a_{HO} = \sqrt{\hbar/m\bar{\omega}}$.

In the case of real gas, where the wave function is influenced by the atom-atom interaction, one must use the mean-field approach allowing one to characterize the many-body system using relatively few parameters. To include excitation, the atom field operator can be written as

$$\hat{\Psi}(\vec{r}, t) = \Phi(\vec{r}, t) + \hat{\Psi}'(\vec{r}, t), \quad (2.9)$$

where $\Phi(\vec{r}, t) \equiv \langle \hat{\Psi}(\vec{r}, t) \rangle$ is the expectation value of the boson field operator. $\hat{\Psi}'(\vec{r}, t)$ describes the first-order perturbation which represents the excitation. This approach is called the Bogoliubov approximation [Bog47]. For temperatures far below the critical temperature the first-order perturbation can be neglected because the higher states have a low probability of being occupied. For this case the "zero-order"-theory describes the wave function of a pure condensate.

The Gross-Pitaevskii Equation

The Gross-Pitaevskii equation [Gro61, Pit61] describes the condensate wave function assuming temperatures close to $T = 0$, where the occupation of the excited states can be neglected. Other effects such as collective excitations or condensate expansion can be described by the Gross-Pitaevskii-equation. The derivation of the equation relies on the approximation of the ensemble as a dilute gas ($n|a|^3 \ll 1$) in the weakly interacting regime. Replacing $\hat{\psi}$ by the condensate wave function in the many-particle Schrödinger equation results in the Gross-Pitaevskii equation

$$i\hbar\frac{\partial}{\partial t}\Phi(\vec{r}, t) = \left(-\frac{\hbar^2\nabla^2}{2m} + U(\vec{r}) + g|\Phi(\vec{r}, t)|^2\right)\Phi(\vec{r}, t). \quad (2.10)$$

To obtain the time independent version, one has to use the ansatz $\Phi(\vec{r}, t) = \phi(\vec{r}, t) \exp(-i\mu t/\hbar)$, which results in

$$\left(-\frac{\hbar^2 \nabla^2}{2m} + U(\vec{r}) + g\phi^2(\vec{r}) \right) \phi(\vec{r}) = \mu\phi(\vec{r}). \quad (2.11)$$

where $g = 4\pi\hbar^2 a/m$ is a coupling constant representing the interparticle interactions and is dependent on the scattering length a and μ . One can choose $\phi(\vec{r})$ to be an real function, normalized to the total number of particles with $N = \int d\vec{r} \phi^2$.

The total energy of the ensemble which is dependent on the particle density is given by

$$E = \int d\vec{r} \left(\frac{\hbar^2}{2m} |\nabla\sqrt{n}|^2 + nU(\vec{r}) + \frac{gn^2}{2} \right) = E_{kin} + E_{ho} + E_{int}. \quad (2.12)$$

The total energy of the particles in a potential contains of three contributions: E_{kin} is the kinetic energy of the particle and corresponds to the uncertainty relation within the trap confinement, E_{ho} is the potential energy due to the potential of the trap and E_{int} is the mean field energy of the atoms. The effect of these three terms can be revealed in the following example. If the trap potential is switched off suddenly, the potential energy vanish will disappear and the expansion of the atoms will depend on E_{kin} and E_{int} . In the following subsection the importance of both fractions to the total kinetic energy after the atoms have been released will be considered.

Thomas-Fermi Approximation

In the case when the scattering length is positive and the confinement is weak, the condensate wave function is essentially dominated by the interaction energy. By neglecting the kinetic energy term in the Gross Pitaevskii equation 2.11, one gets the Thomas Fermi approximation which results in the following condensate density:

$$n(\vec{r}) = \phi^2(\vec{r}) = \frac{\mu - U(\vec{r})}{g} \quad \text{for} \quad \mu - U(\vec{r}) > 0. \quad (2.13)$$

For all other cases of $\mu - U(\vec{r})$ is $n(\vec{r}) = 0$. In a harmonic trapping potential the density distribution has a shape of an inverted parabola and leads to a mean field energy which is the inverse of the external trapping potential. Figure 2.3 shows the typical parabolic shape of the condensate in a harmonic trap in the Thomas-Fermi approximation. The parabolic shape of the density distribution leads to a mean field energy, which is inverse of the potential.

Since the interaction between the atoms in this regime becomes important, it is worth to explain the term *weakly interacting* atomic gas. The interaction energy E_{int} has to be compared to the kinetic energy E_{kin} of the atoms in the trap. The ratio E_{int}/E_{kin}

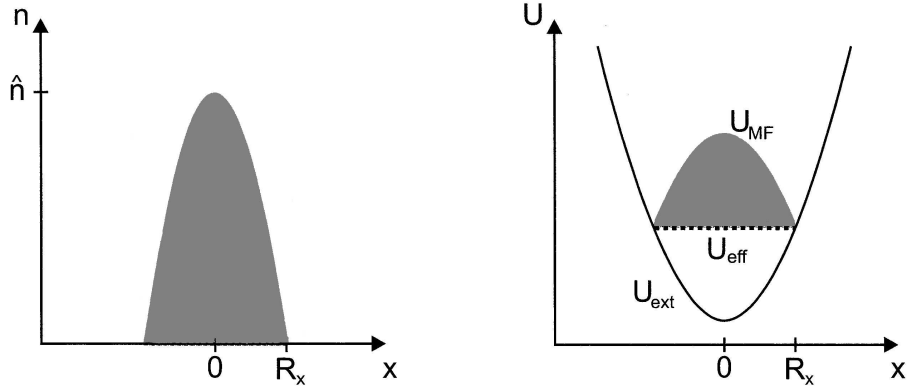


Figure 2.3: In the Thomas-Fermi approximation the density distribution gets its typical parabolic shape. The mean field energy (right hand) is the inverse of the trapping potential.

can be estimated by

$$\frac{E_{int}}{E_{kin}} \propto \frac{N|a|}{a_{ho}}. \quad (2.14)$$

This parameter expresses the importance of the atom-atom interaction compared to the kinetic energy and decides whether we can use the Thomas-Fermi approximation or not. In the first BEC experiment [And95] the ratio was approximately 1. In very large condensates [Dav95] where $N = 10^6 - 10^7$ the ratio is approximately $10^3 - 10^4$.

Using the expression 2.13 we can calculate some important quantities. The peak density and the chemical potential are respectively given by

$$\hat{n} = \frac{\mu}{g} = \frac{\mu m}{4\pi\hbar^2 a}, \quad (2.15)$$

$$\mu = \frac{\hbar\bar{\omega}}{2} \left(\frac{15Na}{a_{ho}} \right)^{2/5}. \quad (2.16)$$

In the parabola-shaped profile the density vanishes at the classical turning point \vec{R} defined by the condition $\mu = V_{ext}(\vec{R})$. For a spherical trap, this implies $\mu = m\omega_i^2 R^2/2$. Using equation 2.16 we find for the radius of the condensate

$$R = \sqrt{\frac{2\mu}{m\omega_i^2}} = a_{ho} \frac{\omega_{ho}}{\omega_i} \left(\frac{15Na}{a_{ho}} \right)^{1/5}, \quad i = x, y, z. \quad (2.17)$$

The radius of the wave function is called Thomas-Fermi radius and can become much larger than the oscillator length. In the case of cigar-shaped traps and large atom numbers the radius becomes macroscopically large (~ 0.3 mm).

The expansion behavior, characterized by the so-called release energy $E_{rel} = E_{kin} + E_{int}$, is very important since it mirrors the energy distribution of the particles. During the first phase of the expansion both energy contributions are rapidly converted into kinetic energy of motion which remains constant during the expansion. In the Thomas-Fermi regime the release energy is dominated by the interaction energy whose distribution follows the inverted parabola form of the density distribution. The condensate remains parabolic during expansion. This leads one to conclude that the expansion of a thermal cloud differs from the expansion of a condensate. In most BEC-experiments this expansion behavior is a telltale sign that a condensate has been achieved. For a partly condensed ensemble one observes a two-component distribution composed of a large thermal Gaussian and a small parabola sitting inside which corresponds to the condensed fraction. In the case of cesium, where one can “switch off” the interaction by tuning the scattering length to zero, we can create so-called “frozen” condensates which almost do not expand [Web03a].

2.1.3 Collapse of a Condensate

Although the density of a condensate is typically five orders of magnitude lower than the density of air, the interactions between the atoms greatly affect the condensate properties such as size, shape and stability. Tuning the strength and sign of the interaction can change the condensate properties dramatically. Such a dramatic change can be easily realized by changing the sign of scattering length a . As we already know for $a > 0$ the interactions are repulsive. In contrast, when $a < 0$, the interactions are attractive causing the gas to contract and thus increase its density in order to minimize the interaction energy. In a trap the contraction competes with the zero-point energy, which tends to spread out the condensate and increases with decreasing size of the spatial extension. If the attractive force is larger than the stabilizing force, the kinetic energy doesn't reach to stabilize the condensate and it collapses. The stabilization effect is an effect of the quantum pressure induced by the spatial localization. But the collapse can be avoided for condensates with less than the critical number of atoms

$$N_{cr} = k \frac{a_{HO}}{|a|}. \quad (2.18)$$

The dimensionless constant k is called the stability coefficient and its size depends on the trap frequency. Its typical value is $k = 0.574$, but for anisotropic traps this value can strongly deviate from this number [Rob01b]. The typical value of the critical number of atoms is about one thousand. For large scattering length, like in the case for cesium, the critical number can be even much smaller. If the condensate is unconfined, the stabilizing term disappears and the condensate is always unstable for an attractive interaction.

The loss mechanism which occurs during the collapse is a result of three-body recombination. This effect is density dependent and thus the loss rate is sensitive to the

dynamics of the shape of the condensate. A deeper study of the collapse might provide a test of a mean-field theory. A detailed treatment of the rich spectrum of condensate dynamics and reactions to perturbations of the condensate wave function can be found in [Pet02].

2.2 Ultracold Gases in 2D

In the most BEC experiments the atoms are trapped in three-dimensional traps where at low energies, the atoms can move three-dimensionally. However if the trap is anisotropic, it is possible that the motion of the atoms is restricted to less dimensions. In this way one can generate an atomic gas confined in one or two dimensions.

If the thermal energy $k_B T$ of the gas is much smaller than the discrete energy steps of atomic motion in the tightly confined direction, then a two-dimensional gas is created. In a degenerate gas in the Thomas-Fermi regime the thermal energy is negligible and the mean field energy, which in 3D corresponds to the chemical potential μ (equation 2.16) dominates, and the condition for a 2D-regime can be expressed as $\mu \ll \hbar\omega_0$. The majority of BEC experiments operate in a 3D-regime where the chemical potential greatly exceeds the level spacing of the trap. In a two-dimensional atomic gas the atoms do not possess enough energy to be excited into higher states, therefore this degree of freedom is not available for the atoms. This means that, geometrically, the atoms cannot travel in this direction, although their extension is dependent from the vibrational frequency ω_0 of the strongly confined direction, given by the ground-state wave function $l_0 = \sqrt{\hbar/m\omega_0}$.

The extension of the ground-state and the temperature play a crucial role in the behavior of the atoms. At temperatures $T \sim \hbar\omega_0/k_B$ we have a confinement-dominated 3D-regime where the scattering length $|a| > l_0$. In order to observe 2D-characteristics in the rates of interatomic collisions, one has to reach temperatures much smaller than $\hbar\omega_0$. In the following paragraphs I will treat the case of the boundary to 2D and the case of a degenerate gas in a two-dimensional regime.

2.2.1 Crossover into the 2D-regime

In order to reach the crossover regime, one has to cool the atoms to release energies comparable to the vibrational energy, $k_B T \leq \hbar\omega_0$. This condition is, in anisotropic trap experimentally accessible without large effort and has been reached in several experiments [Vul99] and [Bou02]. This temperature regime can be considered as a confinement-dominated 3D regime because the strong confinement can influence the energy dependence of the scattering processes. The wave vector p of the relative motion

of the colliding atoms does not decrease with the temperature due to the zero-point oscillation, but corresponds to $p \sim 1/l_0$. If the 3D scattering length is momentum dependent at these p , which is the case for all $|a| \geq l_0$, then the temperature dependence of the elastical processes becomes much weaker. For a large 3D scattering length the tight confinement suppresses the resonant enhancement of the elastic cross section at low energies. Compared to the 3D-case where in the unitarity regime ($|a| \rightarrow \infty$) the cross section strongly increases with decreasing temperature, the reduced cross section leads to reduced thermalization between the tight confined direction and the remaining degree of freedom where the atom populates many vibrational states. The thermalization rate is thus strongly dependent on the ratio between the vibrational quantum energy and the temperature as following:

$$\Omega_{th} \propto \exp\left(-\frac{\hbar\omega_0}{T}\right). \quad (2.19)$$

This exponential dependence can be understood by the fact that only collisions of atoms with sufficient energy to change the vibrational quantum number are allowed. Due to the quantum character of the tight confined particle motion, such decoupling of the degrees of freedom appears also in the hydrodynamical regime where the collisional frequency exceeds the trap frequency. This fact has to be taken into account by considering the temperature when using a cooling method which cools only certain degrees of freedom. In such case the temperature of the uncooled degrees of freedom may be orders of magnitude larger than that of the cooled one.

2.2.2 Bose-Einstein Condensation

All results for the temperature dependence of the condensate in section 2.1.2 have been obtained assuming that the chemical potential is much larger than the motional quantum of the trap. The statistical behavior of a two-dimensional gas exhibits very peculiar features. In a uniform gas, Bose-Einstein condensation cannot occur in 2D at finite temperature because thermal fluctuations would destabilize the condensate. In the presence of a harmonic trap the effect of thermal fluctuations is strongly quenched due to the different behavior exhibited by the density of states $\rho(\varepsilon)$, i.e. the trapping potential introduces a finite size of the sample which sets a lower bound for momentum of excitations. While in the uniform gas we have $\rho(\varepsilon) \propto \varepsilon^{(d-2)/2}$, where d is the dimensionality of the space, in a harmonic trap, the density of states is proportional to ε^{d-1} , and consequently, in the 2D case the integral $N - N_0 = \int \rho(\varepsilon)d\varepsilon/(\exp(\beta\varepsilon) - 1)$ diverges. Considering the critical temperature T_{2D} , we see a difference to the 3D case in the dependence of the atom number [Dal99a, Mul97]

$$T_{2D} \simeq \frac{\hbar\omega_{2D}N^{1/2}}{k_B} \quad (2.20)$$

where $\omega_{2D} = \sqrt{\omega_x \omega_y}$ is the 2D trapping frequency, consisting of the trap frequencies in the both not tightly confined directions.

A two-dimensional condensate compared to the 3D-case exhibits a different density distribution. As has already been described, in the 3D Thomas-Fermi regime the density-distribution gets its typical parabolic shape. If, in the 2D-system, the axial confinement becomes tight then the Thomas-Fermi regime in this direction is not further valid - the axial energy is then dominated by the zero-point energy $\hbar\omega_z$. The two-dimensional chemical potential is given by [Pit03]

$$\mu = \frac{\hbar\omega_z}{2} + g_2 n_2, \quad (2.21)$$

where $g_2 = \sqrt{8\pi}\hbar^2 a / (m a l_z)$ describes the two-dimensional coupling constant and ω_z represents the trap frequency in the tightly confined direction.

The axial dependence of the wave function is Gaussian as

$$\Psi(\vec{r}) = \frac{1}{\pi^{1/4} \sqrt{a l_z}} e^{-z^2/2l_z^2} \Psi_2(\vec{r}_\perp) \quad (2.22)$$

where the oscillator length

$$l_z = \sqrt{\hbar/m\omega_z} \quad (2.23)$$

describes the width of the wave function. The wave function $\Psi_2(\vec{r}_\perp)$ is related to the two-dimensional density as $n_2 = |\Psi_2|^2$. We can use the expression $n(z) = n \exp(-z^2/l_z^2)$ for the three dimensional density profile to calculate $n_2 = \int n(z) dz = \sqrt{\pi} n l_z$. For harmonic trapping $V_{ext}(r_\perp) = \frac{1}{2} m \omega_\perp^2 r_\perp^2$, the density distribution remains parabolic in the x-y-plane and the Gross-Pitaevskii equation takes the following form

$$\left(-\frac{\hbar^2 \vec{\nabla}_\perp^2}{2m} + V_{ext}(\vec{r}_\perp) + g_2 |\Psi_2(\vec{r}_\perp)|^2 \right) \Psi_2(\vec{r}_\perp) = \mu'_{2D} \Psi_2(\vec{r}_\perp) \quad (2.24)$$

where $\mu'_{2D} = \mu_{2D} - \hbar\omega_z/2$ describes the actual two-dimensional chemical potential. Here we have to mention that for very low densities the coupling constant g_2 becomes incorrect and has to be replaced by the exact density-dependent value given in [Pet00].

An important consequence of the vertical density distribution is the fixed extension of the sample in the tight confined direction. While in the three dimensional case the size of a thermal cloud is given by $Z = \sqrt{2k_B T / (m\omega_z^2)}$, which corresponds for a condensed sample to the Thomas-Fermi radius $R = \sqrt{2\mu / (m\omega_z^2)}$, in a 2D-regime the vertical size is given by $Z_{2D} = \sqrt{\hbar / (m\omega_z)}$. In the three-dimensional regime the vertical extension decreases with decreasing temperature and in this way the atoms are compressed, but upon reaching the 2D regime, where the motion in the tightly confined direction is

dominated by the ground-state energy, the size of the cloud stops to decrease at the fixed size of Z_{2D} , then the density decreases with decreasing temperature whereas the size in the x-y-plane keeps its previous three-dimensional character.

Another peculiarity of a two-dimensional system is its coherence behavior. While in a 3D-case the phase coherence, which is the characteristic property of a condensate, has a global character, in a system with reduced dimensionality the atomic gas exhibits spatial phase fluctuations in a degenerate state, that is called *quasi-condensate* [Pet00]. The coherence length of such quasi-condensate is smaller than the extension of the ground state wave function. Such a system can be divided in many blocks with a characteristic size much larger than the healing length $\xi = 1/\sqrt{8\pi na}$ but smaller than the radius of phase fluctuations. Then, there is a true condensate in each block but the phases of the different blocks are not correlated with each other. A true condensate, whose size corresponds to the extension of the ground state, can be created only at temperatures well below the critical temperature.

Experimental realization

According to the equation 2.16, the chemical potential depends on the atom number, the scattering length and the trap frequency. One can vary these parameters in order order to reach the 2D-regime. The cesium atom is an ideal candidate to create a 2D-system because the criterion for a transition into a 2D regime with $\mu \ll \hbar\omega_0$ can be reached by tuning the scattering length via the Feshbach resonance. In our experiment we use a highly anisotropic optical dipole trap to reach the low-dimensional regime (see chapter 6).

The first experimental indication of a quasi-condensate was the observation of a reduction in three-body recombination probability in a two-dimensional system of atomic hydrogen absorbed on liquid helium surface [Saf98]. In an other later experiment the condensate was created in a 3D harmonic trap and then subsequently loaded into a 2D and 1D trap [Gör01]. In order to generate a 2D quantum gas, the BEC was transferred into a disk-shaped optical trap, whereas for the 1D regime the BEC was trapped by a highly elongated magnetic trap. In order to observe the transition from the 3D-regime into 2D, the atom number in the condensate was decreased. The crossover into the two- and one-dimensional regime was observed by a change in aspect ratio and by release energy converging to a non-zero value when the low-dimensional regime was reached.

In our experiment we observe that the release energy cannot be further decreased below the ground state energy of the vertical motion. The phase transition takes place in a regime where about five quantum states are occupied and thus the vertical motion is not yet "frozen out", but further decreasing of the trap depth leads to release energies of the ensemble well below the vibrational quantum energy and the condensed sample becomes two-dimensional.

2.3 Cesium Atom

For almost 40 years the frequency standard has been based on the hyperfine transition of the cesium atom and the second is defined as 9192631770 periods of this transition. Although its properties have been known for many years, it was the last alkali atom to form a Bose-Einstein condensate [Web02]. The reasons for this fact is the scattering properties of cesium making it difficult to trap cesium at higher densities. In this section I will first describe the basic properties and then explain the special behavior of cesium and its scattering properties.

2.3.1 Basic Properties

Cesium was discovered by Robert Bunsen and Gustav Kirchhoff in Heidelberg in 1860 while it received its name because of its blue spectral line. With an atomic mass number of $Z=55$, Cs-133 is the heaviest stable alkali atom. It is the softest of all metals and has a melting point of 28.5°C . The cesium atom has the lowest ionization energy and the strongest Van-der-Waals interaction strength among all elements in the periodic table.

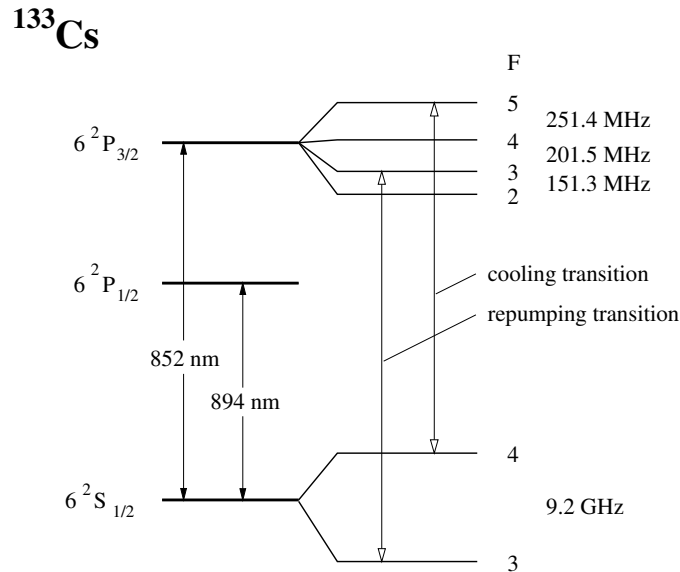


Figure 2.4: Relevant part of the cesium level scheme. The left arrows indicate both D-lines with the corresponding wave lengths. The arrows on the right hand side show the transitions used for the optical cooling in the Magneto-optical trap.

The spin orbit coupling of the one valence electron leads to the well known D line doublet $6^2S_{1/2} \rightarrow 6^2P_{1/2}, 6^2P_{3/2}$. The transition to the $6^2P_{3/2}$ state (D₂ line) is used for laser cooling and has a natural line width of $\Gamma_2 = 2\pi \cdot 5.22\text{ MHz}$, which corresponds to

a lifetime of the excited state of 30 ns. The coupling of the nuclear spin $I=7/2$ leads to the hyperfine structure of the ground and the excited state. The hyperfine splitting of the ground state is 9.2 GHz. Since 1967 the definition of the second has been based on this microwave transition. The hyperfine splitting of the $6^2P_{3/2}$ state is between 150-250 MHz.

For dipole traps an important number is the recoil energy $k_B T_{rec}$. Due to the relatively large mass cesium has a very low recoil temperature of only 200 nK making it very practical for laser cooling and trapping.

2.3.2 Long way to the first cesium BEC

Although the cesium atom was considered to be very good candidate for the first BEC [Mon93] it was the last stable alkali atom to achieve Bose-Einstein condensation. The reason being that it differs from other alkali atoms in many respects and so does not lend itself to forming a BEC.

The early attempts were pursued in magnetic traps in the upper hyperfine ground double polarized (electron and nucleus) state $|F=4, m_F=4\rangle$. However, strong spin-dipole relaxation prevented reaching a regime for efficient evaporative cooling. The measured relaxation rates for this inelastic process were orders of magnitude higher than for other alkali atoms [Söd98]. To avoid the hyperfine-changing collisions the following experiments were made in the lower hyperfine state $|F=3, m_F=-3\rangle$. Since the atoms in this Zeeman substate still possess internal energy, it was not possible to reach quantum degeneracy even at low magnetic fields [Hop00, GO98a].

In order to avoid such inelastic collisions one had to store the atoms in the absolute ground state $F=3, m_F=3$. Since the atoms in this state cannot be trapped magnetically, several groups used optical traps, which trap the atoms independent of their magnetic substate [Vul99, Han01a]. Despite avoiding the "old" problems and cooling the sample very close to phase transition by either Raman-Sideband cooling [Vul99] or evaporative cooling, it appears to be very difficult to reach quantum degeneracy. However, in 2002 the first Bose-Einstein condensation of cesium was realized by using evaporative cooling in a 1064 nm-laser trap [Web03a]. To date no other group has been successful in creating Bose-Einstein condensate of cesium atoms.

2.3.3 Cesium Specialities

The reason behind the long delay in achieving the first cesium condensate is the very special scattering behavior caused by the presence of a virtual molecular state close to the dissociation threshold of the cesium dimer, leading to so-called a zero-energy resonance [Arn97], which in turn results in a large values for the singlet (a_s) and the triplet (a_t) scattering lengths.

To understand the scattering behavior of the cesium atoms, we have to explain some of scattering theory's important parameters. The scattering behavior of a cold atom is completely described by the *scattering length*

$$a = - \lim_{k \rightarrow 0} \frac{\tan \delta_0(k)}{k}, \quad (2.25)$$

where k denotes the collision wave vector of the relative motion of the atoms and δ_0 the phase shift between the incoming and outgoing s -wave. The sign of the scattering length plays a crucial role in the stability of a condensate. Negative scattering length leads to an attractive interaction between the particles. In contrast a positive sign corresponds to repulsive interaction and on stable condensate. If the scattering length is zero, the incoming and outgoing wave functions cancel and there is no interaction.

In scattering theory [Sak94] the total cross section of two non-identical atoms colliding in an arbitrary potential in the low-energy limit is given by $\sigma = 4\pi a^2$. For polarized atoms (when the atoms are in a single m_F -state) we have to take in account that the particles appear as identical leading to a doubling of the s -wave scattering cross section.

$$\sigma = 8\pi a^2 \quad (2.26)$$

Note that all information about the potential, such as its depth, is included in the scattering length. a becomes large and negative for a potential depth which is slightly smaller than the threshold for the appearance of a new bound state. For slightly larger potential depths, a is large and positive [Dal99b]. At the threshold between these two states a diverges, this behavior is called a *zero-energy resonance*. Due to this resonance the expression for the scattering cross section 2.26 has to be modified:

$$\sigma = \frac{8\pi a^2}{1 + k^2 a^2} \quad (2.27)$$

For this expression there are two limiting cases depending on the size of ka

$$ka \ll 1 : \quad \sigma(k) \approx 8\pi a^2 \quad \text{low-energy limit} \quad (2.28)$$

$$ka \gg 1 : \quad \sigma(k) \approx \frac{8\pi}{k^2} \quad \text{unitarity limit} \quad (2.29)$$

If the scattering length a is small compared to the de-Broglie wave length ($a \ll \lambda_{dB}$), then we obtain for the scattering cross section an a^2 -scaling in the low energy limit. For $a \gg \lambda_{dB}$ the scattering cross section reaches its maximum, the so-called *unitarity limit*.

Here arises the fundamental difference between cesium and the other alkali atoms. While for the other alkali atoms the low-energy limit is valid to a temperature of a few microkelvin, (the scattering length is for other alkali atoms typically around a few ten a_0) for cesium, the transition between these two regimes i.e. when $k^2 a^2 = 1$, takes place at around $T \approx 1 \mu\text{K}$ due to the large scattering length (in the range of few thousand a_0).

2.3.4 Feshbach Resonances

The Feshbach resonance belongs to the scattering resonances which play an important role in understanding the cesium atom and its scattering behavior. There are two kinds of

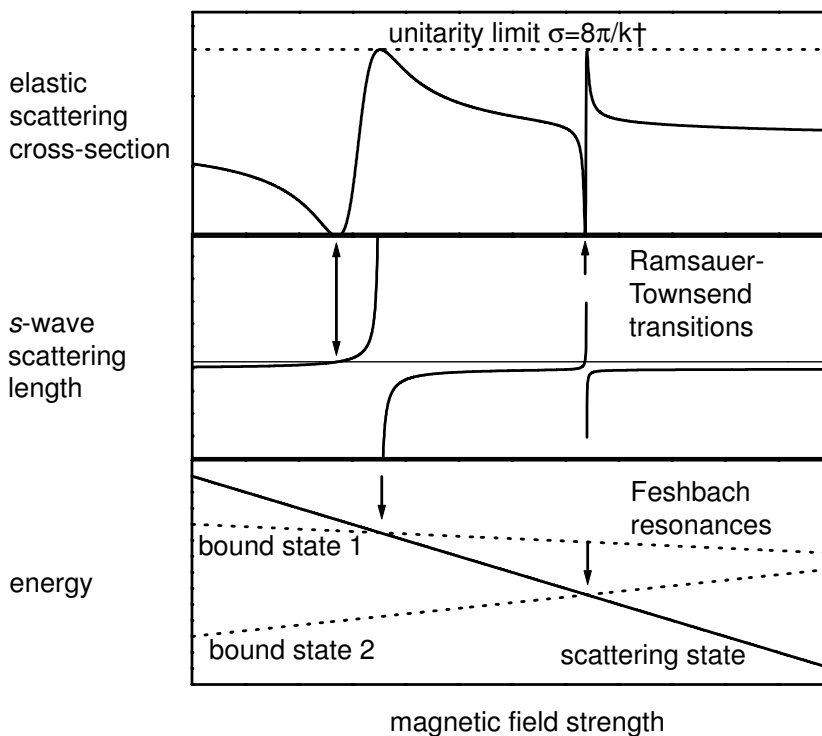


Figure 2.5: In the lowest graph the dotted lines describe the energy of two bound states while the solid line describes the scattering state with varying applied magnetic field. At their crossings the scattering length diverges and the elastic cross section becomes unitary limited as depicted in the upper graphs.

resonances that are significant. The first is called *shape resonance* due to its shape of a single potential energy curve. The quasi bound states confined in centrifugal barriers of attractive potentials decay by tunneling through the barriers. The second kind of resonance is the *Feshbach resonance*, which makes it possible to modify the collisional properties.

Feshbach resonances in interatomic interactions arise from the fact that the energies of an unbound scattering state and a bound state of a different molecular potential are close to each other. If both states are coupled by some mechanism, one can observe a similar effect occurring in the zero-energy resonance, where the scattering length diverges, when the molecular state and the incident state are degenerated. As depicted in figure 2.5, when the molecular state is energetically slightly higher, the scattering length

is large and positive. Conversely the scattering length becomes large and negative if the molecular state is slightly lower in energy. If both states have different magnetic moments, it is possible to shift them against each other by applying an external magnetic field. This fact makes it possible to change the scattering length by varying the magnetic field. Figure 2.5, taken from [Chi01b], shows schematically the behavior of the

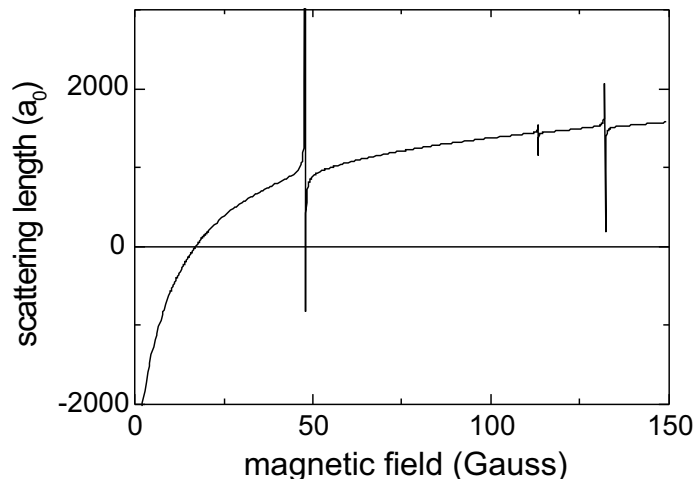


Figure 2.6: Diagram showing the calculated scattering length for atoms in the lowest spin-state $m_F = 3$ versus the applied magnetic field. At 17 G the scattering length exhibits a zero-crossing.

energy levels of the scattering and the bound states, the s-wave scattering length and the corresponding elastic cross section of the $|F = 3, m_F = 3\rangle$ -state with respect to the applied magnetic field. At certain magnetic field, where the bound state and the scattering state cross, the scattering length diverges, while the elastic cross section reach the unitarity limit. When the scattering length is tuned to zero, the elastic cross section vanishes; while on resonance the scattering length diverges and the cross section reach its maximum. Comparing the both resonances shows that the width of the resonances depends on the difference in magnetic moments between the bound and scattering state.

Figure 2.6 shows a calculated scattering length against magnetic field [Leo00]. We see that the scattering length varies strongly with the applied magnetic field and numerically varies between about $-3000 a_0$ and more than $2500 a_0$. At 17 G the scattering length is zero due to a broad resonance with a s-wave molecular state. This zero-crossing makes it possible to change the sign of the interactions between the atoms which plays a crucial role in the proof of the presence of a condensate in our experiment. The relatively weak dependence around zero makes it easy to control the scattering length precisely.

There are many other resonances which are not visible in the scattering length curve. These are, for example, resonances in d-wave or g-wave molecular states which can be

observed in a radiative loss curve as very narrow resonances with a width of about a few mG. Due to the coupling of the s -wave to higher angular momentum states, there is a rich spectrum of Feshbach resonances. Experimentally there have been found around 60 resonances in both elastic and inelastic processes [Chi00]. All of the observed resonances can be explained theoretically [Leo00]. In our experiment we observe all $|3, 3\rangle + |3, 3\rangle$ and several $|3, 3\rangle + |3, 2\rangle$ resonances.

Chapter 3

Theoretical background

Laser cooling experiments have connected many fields in physics. In the past twenty years especially, laser physics have achieved many breakthroughs which, in turn, have led to the development of laser cooling techniques. The trapping of neutral atoms enabled physicists to study new phenomena in the quantum-mechanical dynamics of the atom. The following chapter gives an overview of how these different disciplines interact in context to this particular experiment. A concise overview of laser cooling and trapping is given in the textbook [Met99].

Section 3.1 will focus on the basic principle of the optical dipole force. This is needed in the following section which addresses evanescent waves. Section 3.3 details the interaction of an magnetic dipole moment and a magnetic field. Section 3.4 is dedicated to atom-atom and atom-laser interactions occurring in our experiment. Finally, a very important cooling method, evaporative cooling, is discussed in Section 3.5.

3.1 Optical Dipole Force

The interaction between a laser field and an atom leading to optical forces has been studied and developed for some time. The exploitation of this interaction has become a standard way to trap and cool neutral atoms around the world. The force between the atom and the laser depends on several quantities, but especially the detuning between the atomic transition frequency and the frequency of the laser field.

At very small detunings the so-called *radiation pressure* force is important. This does not belong to the "family" of dipole forces. The radiation pressure force arises from repetitive absorption and spontaneous re-emission of a photon. For directional light, the atoms will experience a directional force from the laser photons because the spontaneous emission occurs isotropically and therefore the recoil from the emitted photons will average to zero. The radiation pressure force can be determined by the product of the spontaneous photon scattering rate and the photon recoil and can create accelerations

up to $10^6 m/s^2$. Atoms can therefore decelerate within few ten milliseconds to very small velocities. How quickly this happens depends on the detuning δ . The smaller it is, the larger is the scattering rate and thus the force to the atom. In our experiment the radiation pressure force plays a role only in the magneto-optical trap (MOT) [Raa87], where it is used in a combination with a magnetic field, the Zeeman decelerating beam and the five trapping beams as described in Section 4.3. This trapping and cooling technique is described in [Met99] in more detail.

At large detunings, the radiative force becomes very weak and the optical dipole force takes over the atom-atom interaction. The other point is, that due to the photon-scattering nature of the radiative force it limits the temperature attainable in such trap based on this force. The lowest temperature is in the range close to the photon recoil which, for the case of cesium atoms corresponds to a temperature of 200 nK. To reduce, or almost eliminate photon scattering, the atoms have to be transferred into a conservative trap, such as an optical dipole trap or magnetic trap.

In order to get a intuitive picture of the dipole force it is useful to use the classical picture of an atom with a harmonically bound electron. All important effects can be studied with this model and they are, for alkali atoms, very accurate [Ask62, Kaz73].

When a polarizable atom is injected to an electric field \vec{E} the interaction between the field and the electron induces a dipole moment \vec{p} . The same effect occurs in a oscillating laser field, but there the dipole moment is driven by the oscillating laser field. The potential energy of the atomic dipole inside this field can be written as

$$U_{dip} = -\frac{1}{2}\langle\vec{p}\vec{E}\rangle \quad (3.1)$$

The factor $1/2$ comes from the fact that the induced dipole moment of the atom comes from the same electric field. There are three different cases for the resulting potential. First, when the driving laser frequency is below the atomic resonance (*red detuned*), the dipole moment will oscillate in phase with the electric field, the potential is attractive and takes a negative value. Second, for a laser frequency above the resonance (*blue detuned*) the potential takes a positive value and is repulsive. Finally, in the case of resonant excitation the dipole oscillates with a phase of $\pi/2$ with respect to the laser field and thus $\langle\vec{p}\vec{E}\rangle$ vanishes. In our experiment the Gravito-optical surface is based on repulsive fields and also the horizontal confinement of the dimple trap is realized with red-detuned laser beam. The intensity gradient of the laser field determines the size of the dipole force $-\nabla U_{dip}$ and the sign of the potential is determined by the detuning of the laser field.

The derivation from the potential makes the dipole force conservative, but in addition to this dispersive part an absorptive component leads to photon-scattering and either leads to heating due to transfer of photon momentum, or to cooling through a dissipative mechanism, such as the Sisyphus cooling described in Section 5.1. To implement the absorptive part in the calculations, one has to include damping into the classical Lorentz

model. The dipole potential and the photon scattering rate can be calculated as following [Gri00]:

$$U_{dip}(\vec{r}) = -\frac{3\pi c^2}{2\omega_0^3} \cdot \left(\frac{\Gamma}{\omega_0 - \omega} + \frac{\Gamma}{\omega_0 + \omega} \right) \cdot I(\vec{r}), \quad (3.2)$$

$$\Gamma_{sc}(\vec{r}) = \frac{3\pi c^2}{2\hbar\omega_0^3} \cdot \left(\frac{\omega}{\omega_0} \right)^3 \cdot \left(\frac{\Gamma}{\omega_0 - \omega} + \frac{\Gamma}{\omega_0 + \omega} \right)^2 \cdot I(\vec{r}). \quad (3.3)$$

where $I(\vec{r})$ describes the position dependent laser intensity. The damping rate Γ can be written as a quantum mechanical transition rate

$$\Gamma = \frac{\omega_0^3}{3\pi\epsilon_0\hbar c^3} \cdot |\langle e|\hat{p}|g\rangle|^2. \quad (3.4)$$

with $\langle e|\hat{p}|g\rangle$ as the dipole matrix element for the transition, where the ground state $\langle e|$ and the excited state $\langle g|$ are coupled by the dipole operator \hat{p} .

Depending on the detuning of the laser field, there are different regimes for a optical dipole trap. In the following two paragraphs I will describe two cases which are relevant in our experiment.

Near-resonant Dipole Traps

In this case, the laser frequency is relatively near to the atomic resonance and thus the detuning δ is much smaller than the atomic resonance. Here the contribution from the so-called counter-rotating term $\Gamma/(\omega + \omega_0)$ can be neglected and equations 3.2 and 3.3 simplified to

$$U_{dip}(\vec{r}) = -\frac{3\pi c^2}{2\omega_0^3} \cdot \left(\frac{\Gamma}{\delta} \right) \cdot I(\vec{r}), \quad (3.5)$$

$$\Gamma_{sc}(\vec{r}) = \frac{3\pi c^2}{2\hbar\omega_0^3} \cdot \left(\frac{\Gamma}{\delta} \right)^2 \cdot I(\vec{r}). \quad (3.6)$$

All considerations up to now were limited to the case of a two-level system. Since the atoms have fine and hyperfine structure, a proper treatment of these is required. Working with a linearly polarized laser field with a detuning larger than the hyperfine structure splitting of the excited state (~ 200 MHz), but smaller than the fine structure splitting between the D_1 and D_2 lines (16.6 THz), the dipole potential is given by the expression

$$U_{dip}(\vec{r}) = \frac{\pi c^2}{2} \cdot \left(\frac{\Gamma_2}{\omega_2^3} \frac{2}{\delta_2} + \frac{\Gamma_1}{\omega_1^3} \frac{1}{\delta_1} \right) \cdot I(\vec{r}). \quad (3.7)$$

where $\delta_1(\delta_2)$, $\Gamma_1(\Gamma_2)$, and $\omega_1/2\pi$, $(\omega_2/2\pi)$ are the detunings, natural linewidths and frequencies of the D_1 and D_2 lines respectively. Due to the ω^3 -scaling of Γ we can approximate $\Gamma_1/\omega_1^3 \approx \Gamma_2/\omega_2^3$. If additionally, the laser frequency is much closer to the D_2 than to the D_1 line, we get the result for the near resonant case

$$U_{dip,nr}(\vec{r}) = -\frac{\pi c^2 \Gamma_2}{\omega_2^3 \delta_2} \cdot I(\vec{r}) \quad (3.8)$$

$$\Gamma_{dip,nr}(\vec{r}) = \frac{\pi c^2}{\omega_2^3} \left(\frac{\Gamma_2}{\delta_2}\right)^2 \cdot I(\vec{r}). \quad (3.9)$$

These assumptions can be used for the dipole potential generated by a low power laser operating close to the resonance, such as the laser fields used for the hollow beam (40 – 90 GHz) and the evanescent wave (2 GHz) in the GOST.

Far off-resonance Traps

At larger detunings another approximation must be used. For laser detunings much larger than the fine splitting ($\Delta\lambda_{FS} = 42$ nm), both fine-structure transitions have to be taken into account. To implement these into the model, one can assume a two-level atom with an effective transition defined by the weighted average of both D lines

$$\omega_{eff} = \frac{1}{3}\omega_1 + \frac{2}{3}\omega_2 \quad (3.10)$$

and a weighted line width defined by

$$\Gamma_{eff} = \frac{2}{3}\Gamma_2 + \frac{1}{3}\Gamma_1 = 2\pi \cdot 4.98 \text{ MHz}. \quad (3.11)$$

In this case the counter rotating term can not be neglected. We finally obtain

$$U_{dip,FORT}(\vec{r}) = -\frac{3\pi c^2}{2\omega_{eff}^3} \cdot \left(\frac{\Gamma_{eff}}{\omega_{eff} - \omega} + \frac{\Gamma_{eff}}{\omega_{eff} + \omega}\right) \cdot I(\vec{r}), \quad (3.12)$$

$$\Gamma_{dip,FORT}(\vec{r}) = \frac{3\pi c^2}{2\omega_{eff}^3} \cdot \left(\frac{\omega}{\omega_{eff}}\right)^3 \cdot \left(\frac{\Gamma_{eff}}{\omega_{eff} - \omega} + \frac{\Gamma_{eff}}{\omega_{eff} + \omega}\right)^2 \cdot I(\vec{r}). \quad (3.13)$$

for the potential and the scattering rate for the far off-resonant case respectively. These formulas are valid for a linear polarized laser field only. A small correction has to be added for circular polarized laser light. However, these results can also be used as a good approximation for non-linearly polarized beams. Further details on the dependence of the polarization and optical dipole forces are given in [Gri00].

Such a far off-resonant trap is implemented in our experiment by the dimple trap, which is the linearly polarized output of a 5 W Yb-fibre laser. Since it is red detuned,

the atoms are trapped in the intensity maximum of the focussed laser beam. Due to the detuning of more than 200 nm, heating through photon scattering can be neglected in our case.

3.2 Evanescent Waves

One particular feature of the GOST and also of the micro trap is the evanescent wave which provides vertical confinement. With such a geometry, we have a unique trap which enables us to realize a two-dimensional degenerate quantum gas a few micrometers above a dielectric surface. Because of the evanescent wave, and its particular properties, plays such an important role in the realization of our particular traps, I will describe the evanescent wave and its properties in more detail.

An evanescent wave has the special feature that its electromagnetic field drops exponentially with increasing distance from the dielectric boundary. Since the decay length is in the order of the wave length, the gradient of the laser field and thus the resulting force is very large and the potential can be in most cases considered as a wall. A further interesting point is that a reflection of a multi-level atom from the evanescent wave can lead, under certain circumstances, to an inelastic reflection and cooling of the atom.

To create the evanescent wave, we use a fused silica prism where the laser beam undergoes an total internal reflection at the surface of the prism. This reflection follows Snell's law $n \cdot \sin \Theta_i = \sin \Theta_t$, with Θ_i and Θ_t as angle of incidence and the angle of refraction, and n as the index of refraction of the dielectric medium. For fused silica $n = 1.45$. At a critical angle, Θ_{crit} , the left side of the formula becomes 1 and the incident light is completely reflected from the inside of the surface. Since the light field can not instantaneously drop to zero across the surface, we observe for angles of incidence larger than the critical angle, a light field along the dielectric-vacuum interface with exponentially decreasing amplitude. The mathematical expression for the electric field component of the evanescent wave is [Bou94]:

$$\vec{E}_t(\vec{r}, t) = \varepsilon_t \cdot \vec{\epsilon}_t \cdot e^{-z/\Lambda} \cdot e^{i(k_t x - \omega_L t)}. \quad (3.14)$$

ε_t denotes the amplitude of the electric field, $\vec{\epsilon}_t$ the polarization vector, and Λ the $1/e^2$ -decay length of the evanescent wave. The phase of a plane wave propagating along x is given by the second exponential term, where ω_L denotes the laser frequency and k_t the evanescent wave number. The decay length is dependent on the angle of incidence and the wavelength of the laser light λ and can be calculated from the formula

$$\Lambda = \frac{\lambda}{2\pi \sqrt{n^2 \sin^2 \Theta_i - 1}}. \quad (3.15)$$

In order to characterize the evanescent wave, one has to find the expression for the field

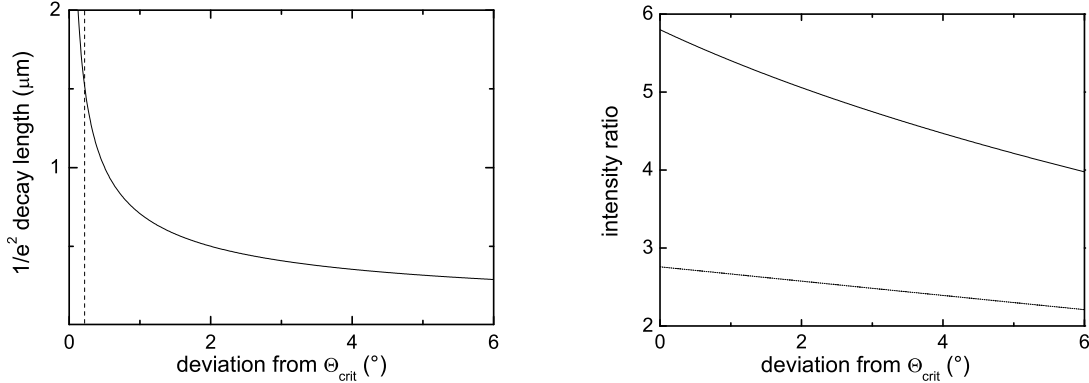


Figure 3.1: Decay length Λ and enhancement factor I_t/I_0 of the evanescent wave versus deviation from critical angle. The vertical dashed line shows the angle we use in the red GOST corresponding to a decay length of $1.4 \mu\text{m}$. The righthand diagram depicts the intensity ratio I_t/T_0 for the *TM*- (solid line) and the *TE*-polarization (dotted line) as a function of $\Delta\Theta$.

amplitude and the polarization of the evanescent wave. There are two relevant cases, one in which the polarization $\vec{\epsilon}_t$ can be perpendicular (*TE*) to the plane of incidence, the other, parallel (*TM*). In the case of *TE*-polarization the polarization of the evanescent wave matches with that of the incident light ($\vec{\epsilon}_t = \vec{\epsilon}_i$). The intensity I_t is dependent on the intensity of the incident light I_0 and can be written as

$$I_t = \frac{4n \cos^2 \Theta_i}{n^2 - 1} \cdot I_0. \quad (3.16)$$

The calculations for the *TM*-polarization result in the evanescent wave having an elliptical polarization with a phase-shifted component perpendicular to the surface of the prism. Thus the potential becomes dependent of the magnetic quantum number. Further, the evanescent wave intensity is larger than in the case of the *TE*-polarization and is thus more favorable for our trapping scheme in order to maximize the dipole potential. The calculations result in the following expressions [Bou94]:

$$\vec{\epsilon}_t = \frac{1}{\sqrt{2n^2 \sin^2 \Theta_i - 1}} (n \sin \Theta_i \vec{e}_z - i \sqrt{n^2 \sin^2 \Theta_i - 1} \vec{e}_y), \quad (3.17)$$

$$I_t = \frac{4n \cos^2 \Theta_i}{n^2 - 1} \cdot \frac{2n^2 \sin^2 \Theta_i - 1}{(n^2 + 1) \sin^2 \Theta_i - 1} \cdot I_0. \quad (3.18)$$

Figure 3.1 shows the $1/e^2$ -decay length of the intensity as a function of the deviation from the critical angle $\Theta_{crit} = 43.6^\circ$. The right diagram depicts the intensity ratio I_t/I_0

for the TM- (solid line) and the TE-polarization as a function of $\Delta\Theta$. The vertical dashed line at $\Delta\Theta = 0.2^\circ$ indicates the angle used for the evanescent wave in the micro trap resulting in the decay length $1.4 \mu\text{m}$.

Van-der-Waals Interaction

For relatively large distances from the dielectric surface, the force on the atom is dominated by the evanescent light field, but the closer the atoms get to the surface the more important the forces caused by the surface become. For example in the dimple trap, the atoms are trapped less than a micron above the prism surface. In this case, considering the vertical potential, the interaction between the atoms and the surface cannot be neglected while for temperature measurements it is also important to be able to calculate the maximum of the vertical potential. The vertical potential in our dipole traps is not only given by the evanescent wave, but also by the attractive Van-der-Waals interaction between the atom and the dielectric surface, and by the relatively weak gravitational field. These additional effects will be explained in the following paragraphs.

The reason for an attractive Van-der-Waals force is based upon the electromagnetic interaction of an atomic dipole with its mirror image on the dielectric surface. It is not my intention to describe this problem in its complexity with retardation effects or QED corrections (for this I refer the reader to [Har91] and [Wyl84]), but I will use the following approximation: the atom will be treated as a two-level system with an effective transition wavelength $\lambda = 866 \text{ nm}$ and the surface of the prism is assumed to be perfectly conducting.

In the consideration of the Van-der-Waals potential there are two special cases which differ depending on the distance of the atom above the surface. The regime for the the case where the atom is close to the dielectric surface ($z \ll \lambda_{eff}/2\pi$) is called the *Lennard-Jones* regime and can be accurately described by the expression [Cou96]:

$$U_{VdW}(z) = -\frac{n^2 - 1}{n^2 + 1} \frac{3}{16} \hbar \Gamma_{eff} \left(\frac{1}{k_{eff} z} \right)^3 = 5.44 \cdot 10^{-49} \text{ kgm}^5/\text{s}^2 \cdot z^{-3} \quad (3.19)$$

where $\Gamma_{eff}/2\pi = 4.98 \text{ MHz}$, the k_{eff} is the linewidth and the wave number of the effective transition. The fact, that we have a dielectric surface is satisfied in the equation for the potential by multiplying with the $(n^2 - 1)/(n^2 + 1)$ -term.

In the case of atom the being far away from the surface ($z \gg \lambda_{eff}/2\pi$) the regime is called the *Casimir-Polder-regime* [Cas48] and the surface attraction is proportional to z^4 . This regime does not allow simple analytical expressions because relativistic and QED-effects can not be neglected anymore. Using the tabulated values in [Mar97], the complete expression for the Van-der-Waals potential of an two-level atom can be written as

$$U_{VdW}(z) = -\alpha_{VdW} \cdot \frac{1}{z^3(1 + 2\pi z/\lambda_{eff})}. \quad (3.20)$$

with $\alpha_{VdW} = 5.44 \times 10^{-49} \text{ kg m}^5\text{s}^{-2}$ as a coefficient. The z^4 -scaling leads to the fact that

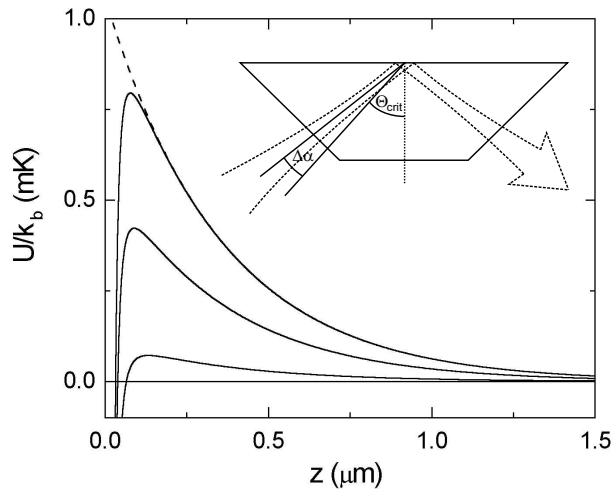


Figure 3.2: Potential curves for the dipole repulsion alone (dashed line) and the combined potential of dipole repulsion and Van-der-Waals attraction for the three laser powers 45 mW, 25 mW and 5 mW. We see that with decreasing power of the evanescent wave the potential wall becomes smaller. The other experimental parameters were $\Delta\Theta = 1^\circ$, $\delta_{EW}/2\pi = 3 \text{ GHz}$ and a beam waist of $700 \mu\text{m}$.

only the atoms very close to the surface are affected by the attractive interaction. So at higher temperatures, and in evanescent waves working with large decay lengths where the atoms are “sitting” relatively high above the surface, the trajectories of the atoms are hardly influenced. But, as figure 3.2 shows, the Van-der-Waals interaction significantly changes the shape of the potential at small distances. The dashed line shows the repulsive potential of the evanescent wave alone. The solid lines describe the combination of the repulsive and attractive potential for three different powers of the evanescent wave. These three laser powers of 45, 25 and 5 mW show the importance of the attractive potential at distances below 150 nm. The position of the maximum of the potential is important for temperature calculations where it is important to know its exact position since the position decides whether the atoms are recaptured or are able to escape.

Influence of Gravity

Already the name Gravito-Optical Surface Trap implies that gravity plays an important part in our trapping scheme. The vertical potential in our dipole traps is a combination of the already described optical potential of the evanescent wave, the Van-der-Waals potential and the gravity. The resulting potential is given by the following expression:

$$U(z) = mgz + U_0 e^{-2z/\Lambda} + U_{VdW}(z). \quad (3.21)$$

m denotes the mass of the cesium atom, g the gravitational acceleration and U_0 the dipole potential at $z = 0$.

Atoms released into this potential will bounce. The time between successive bounces depends on the maximum height h and the maximum perpendicular velocity v_\perp to the EW as described by $\Delta t = 2\sqrt{2h/g} = 2v_\perp/g$. An important quantity to characterize is the probability of reflection with spontaneous photon scattering. Using the probability for such incoherent reflection [Gri00]

$$p_{sp} = \frac{m\Lambda\Gamma}{\hbar\delta} v_\perp. \quad (3.22)$$

one can calculate the average photon scattering rate

$$\Gamma_{sc} = \frac{p_{sp}}{\Delta t} = \frac{mg\Lambda\Gamma}{2\hbar\delta} \quad (3.23)$$

It turns out that Γ_{sc} does not depend on the energy of the atom. This can be explained by the fact that the decrease of scattering probability for colder atoms is exactly compensated by the larger bounce rate.

Obviously the bounce height $k_B T/mg$ is dependent on the temperature and is $3.2 \mu\text{m}$ for an atom with thermal energy $k_B T = 500 \text{ nK}$. Since the range of the dipole potential is about $1 \mu\text{m}$, the exact shape of the potential can not be neglected. Only for higher temperatures can the potential can be approximated as a hard wall. For this case, one can calculate the eigenenergies of the n -th vertical mode as [Wal92]

$$E_n = \hbar\omega_v \left(n - \frac{1}{4} \right)^{2/3}, \quad (3.24)$$

with $\omega_v = (9\pi^2 mg^2/8\hbar)^{1/3}$ being the characteristic frequency which, for Cs-atoms is $\omega_v = 2080 \text{ Hz}$, corresponding to a temperature of $\hbar\omega_v/k_B \approx 95 \text{ nK}$. For very low energies, the approximation of a hard wall is not valid, but we can approximate the potential as harmonic and thus calculate the vibrational quantum energy. For the measured vertical trap frequency of $\omega = 550 \text{ Hz}$ we calculate a vibrational quantum energy of $\hbar\omega = k_B \times 26 \text{ nK}$. In Chapter 6 we will see that we achieve release energies smaller than the distance between the energy levels leading to dominantly populating the vertical motional ground state.

3.3 Magnetic Force

Atoms can not only be trapped with optical forces but with magnetic fields also. In our experiment we use magnetic fields in a combination with laser light in the MOT or, alternatively, we use it to tune the scattering length via the Feshbach resonance. But the magnetic force becomes important in our experiment when the atoms are levitated in order to measure their polarization.

Magnetic forces are a result of the interaction between the magnetic dipole moment $\vec{\mu}$ and the applied magnetic field \vec{B} . Since the magnetic dipole moment can not be induced by the magnetic field, such as in the case in electric dipole moment, the atom must possess a permanent magnetic moment. This precondition is fulfilled for all atoms with a spin \vec{S} not equal to zero. The magnetic moment can be written as $\vec{\mu} = -g_F \frac{\mu_B}{\hbar} \vec{S}$, with g_F as the Lande factor of the considered hyperfine level and μ_B as the Bohr's magneton. Applying a magnetic field leads to the potential $U = -\vec{\mu} \cdot \vec{B}$. Atoms whose spins are antiparallel to the magnetic field can be trapped at the minimum of the magnetic field where their potential energy reaches a minimum. This leads to only *low-field-seeking* atoms being able to be trapped magnetically. However, the atom can only be trapped if the atomic spins follows the magnetic field vector adiabatically. This is the case as long as the Larmor precession frequency is larger than the rotation frequency of the magnetic field axis in the atoms's frame of reference. Then the potential for an atom with the quantum number m_F can be written as

$$U = m_F g_F \mu_B B. \quad (3.25)$$

The quantum number m_F takes the values $m_F = -F = -3$ and the Lande factor is $g_F = -1/4$ [Hak00, Ste02] for an atom in the $F = 3, m_F = 3$ state. This results in the potential energy

$$U_B(F = 3, m_F = 3) = -\frac{3}{4} \mu_B B = -k_B \cdot 50,4 \mu\text{K} \cdot B/G. \quad (3.26)$$

The intention of magnetic trapping in our experiment is not to store the atoms magnetically for a long time, but to compensate for gravity for atoms in the absolute ground state. In order to cancel gravity, the gravitational potential $U_g = m_{Cs} g z = 1568 \mu\text{K} \cdot z/\text{cm}$ has to be compensated by the magnetic potential. The levitation for the atoms in the $|F = 3, m_F = 3\rangle$ -state is achieved by the following vertical magnetic field gradient

$$\frac{\delta B}{\delta z} = \frac{4 m_{Cs} g}{3 \mu_B} = 31.3 \text{ G/cm} \quad (3.27)$$

Applying this gradient leads to compensation of gravity only for atoms in the ground state. All atoms in other magnetic substates do not experience full compensation and follow the oscillatory behavior at the evanescent wave. With the levitation field we are now able to distinguish atoms in the $m_F = 3$ -state from atoms in other magnetic substates, and thus to determine degree of polarization of the sample.

3.4 Inelastic Collisions

As already mentioned in the previous chapter, the inelastic processes in cold ensembles of Cs-atoms, which are generally up to three orders of magnitude more severe as in ensembles of other alkali atoms, made the generation of a Cs-BEC impossible for long time. First, the work done in investigating the zero-energy resonance [Vul99] led the way to avoiding there strong losses. However, there are also other mechanisms which lead to losses in dipole traps, the inelastic processes.

The inelastic processes can be categorized in three main categories according to the number of atoms involved in the collision process. One of the processes is density independent, where the trapped atoms can be hit by a background gas atom. Since such background gas atoms are at room temperature, the energy transferred to the trapped atoms is much larger than the trap depth: the atom gets immediately lost. In our apparatus this process is strongly suppressed by the good vacuum, leading to background gas limited lifetimes of several minutes. This loss process plays a minor role in our trap where we have lifetimes of about 10s. A more important significant loss process in our experiment is the two-body process where two atoms collide and either internal energy, or energy from the light field is transferred into kinetic energy of the atoms leading to a removal of both atoms. The third and final process is the three body collisions which only becomes important at higher densities, in our case especially at the end of the evaporation. In this process two atoms collide to form a dimer while a third atom carries away the binding energy and momentum.

In the following subsections I will describe the two- and three-body processes and how they can be reduced or even removed.

3.4.1 Two-body Collisions

The most frequent inelastic process in our trap is inelastic collisions that occur in the presence of a blue-detuned light field. This process is illustrated in figure 3.3. The blue detuned evanescent wave serves, in this type of collision, as an energy reservoir. The atom can be excited during a collision with another atom into the repulsive $S_{1/2} + P_{3/2}$ molecular potential by the blue detuned evanescent wave photon at the Condon point, where the resonance condition is met. Now, the energy of $\hbar\delta_{ew}$, which corresponds at 2 GHz detuning to a thermal energy of about 100 mK, is converted into kinetic energy of both atoms. This leads to a loss of both atoms in the shallow dipole trap.

Apart from the repulsive excited state there is also an attractive one which, when assisted by red-detuned laser light, can be involved during a collision. This kind of a collision can only take place in a near red-detuned trap, such as the MOT. The light used in the dimple laser is so far detuned from resonance that it does not lead to such light induced collisions. The prominent loss mechanism in the GOST and the micro trap involves the blue-detuned light of the evanescent waves. It is evident that this loss

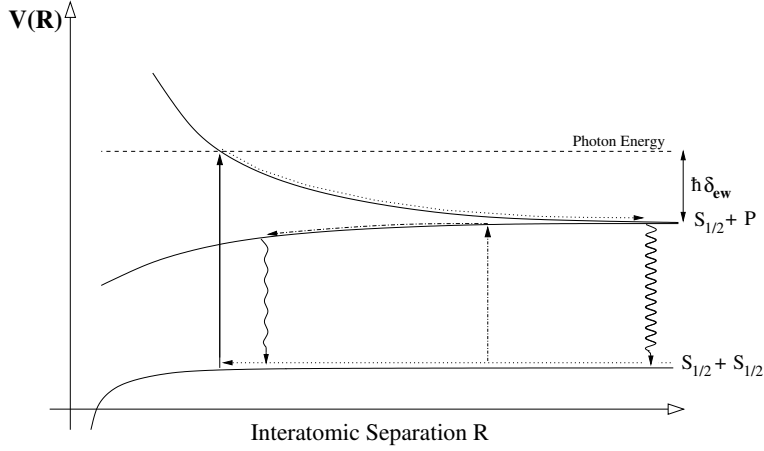


Figure 3.3: *The two relevant electronic transitions involved in light-assisted inelastic collisions. The repulsive molecular potential is excited by blue-detuned light, whereas the attractive potential can be excited by red-detuned light fields.*

process is dependent on the detuning of the blue light field. The detuning dependence of the loss coefficient β has been investigated in [Ham]. A semiclassical model which has been made assumes that β is proportional to the probability of an atom being at the Condon point, and to the probability for excitation by the light field. Using a semiclassical Landau-Zener model results in the following detuning dependence on the rate coefficient

$$\beta \propto \frac{I}{\delta_{EW}^2} \quad (3.28)$$

where I is the intensity of the evanescent laser beam. The proportionality of the detuning has been confirmed experimentally. In the case of the near-resonant evanescent wave the rate coefficient is in the order of $10^{-12} \text{ cm}^3/\text{s}$ and can be significantly reduced by increasing the detuning of the evanescent wave. In the dimple trap the evanescent wave laser beam is more than 10 nm red-detuned, and therefore this process is strongly suppressed. Above 1 nm we have observed no significant loss due to this collision process.

There is another important two-body process making the life of the experimentalists difficult. These difficulties are associated with the properties of the magnetic trap. In a magnetic trap only atoms in the $|F = I + 1/2, m_F = F\rangle$ and $|F = I - 1/2, m_F = -F\rangle$ -states can be trapped. I describes the nuclear spin and is, in the case of cesium, $7/2$. If one or both atoms change their magnetic substate during a collision they are lost. Usually the loss rates for this process are very low ($\beta \approx 10^{-15} \text{ cm}^3/\text{s}$), but in the case of cesium the spin relaxations rates were measured to be three orders of magnitudes higher than expected [Söd98, Arl98]. Due to the large scattering length the atoms

penetrate to smaller internuclear distances where high-order processes like the second-order spin-orbit interaction take place [Leo98]. The large mass of the cesium atom leads to a large contribution of this spin-spin coupling and makes the formation of a BEC in this state impossible [GO98a]. Trapping the atoms in the lower hyperfine state $|F = 3, m_F = -3\rangle$ avoids the hyperfine-changing interactions but the Zeeman-energy may be released during a collision. Even at small magnetic fields the inelastic losses are too high to reach quantum degeneracy [GO98b, Hop00].

This loss process does not exist for fully polarized samples where the atoms are in the absolute ground state $|F = 3, m_F = 3\rangle$ and thus do not have any internal energy. Such a sample of atoms can be trapped only in an optical dipole trap. It should also be noted that in an optical dipole trap this inelastic process cannot be always avoided. In an unpolarized sample, a small fraction of atoms populate higher spin-states and thus possess internal energy depending on the Zeeman-splitting and the state they occupy. The energy splitting between neighboring m_F -states is $\Delta E/k_B = 16.8 \mu\text{K}$ per Gauss and plays a minor role at small magnetic fields and deep potentials, such as in the GOST. However in the dimple trap where some atoms may occupy higher magnetic sub-states and a magnetic field of typically 30 G is applied, the m_F -state changing collisions can be of importance also at higher potentials. When no depolarizing mechanism is present, the polarization degree of the atoms can increase when being trapped since atoms in higher spin-states decay.

3.4.2 Three-body Recombination

If the atoms are in the absolute ground state and the trapping laser fields are far from the resonance, the inelastic two-body collisions can be ignored. However three-body collisions in which two atoms form a molecule, while a third atom is present to satisfy momentum and energy conservation. It is difficult to distinguish the three-body recombination from a two-body loss in our experiment. Since the loss process in the GOST and the micro trap is dominated by two-body processes, it is almost impossible to study the three-body recombination in our microtrap. The three-body recombination with Cs-atoms has been studied in [Web03b] where the exact loss coefficients have been determined.

Since, for the three-body recombination, three atoms have to be present the rate γ_{rec} for such events scales with the density n as $\gamma_{rec} = \alpha_{rec}n^3$, with the characteristic parameter α_{rec} . In the limit of ultra low interaction this parameter scales with the scattering length and the mass of the atom as $\alpha_{rec} \propto a^4/m$. Since it is not possible to measure the three-body events experimentally one must extract the three-body coefficient L_3 from the measured losses. The three-body coefficient is given by

$$L_3 = n_l C \frac{\hbar}{m} a^4. \quad (3.29)$$

n_l denotes the number of atoms lost per recombination event and C is a dimensionless factor, which can take on values between 0 and 70. The recombination process sets free the molecular binding energy $\varepsilon = \hbar^2/ma^2$ which corresponds to the binding energy of the weakly bound last energy level of the dimer. This energy is typically large compared to the trap depth and since the molecule and the third atom receive $\varepsilon/3$ and $2\varepsilon/3$ respectively, they leave the trap. In this case n_l in formula 3.29 is equal to 3. For large scattering length ε becomes small and if the energy doesn't reach to expel the molecule, it can be either lost as a dimer or the molecule is trapped and stays in the atom ensemble. If it releases its high vibrational excitation energy in an inelastic collision with a fourth atom, all three collision partners are expelled from the trap. The kinetic energy of the remaining atom leads to *recombination heating* of the ensemble.

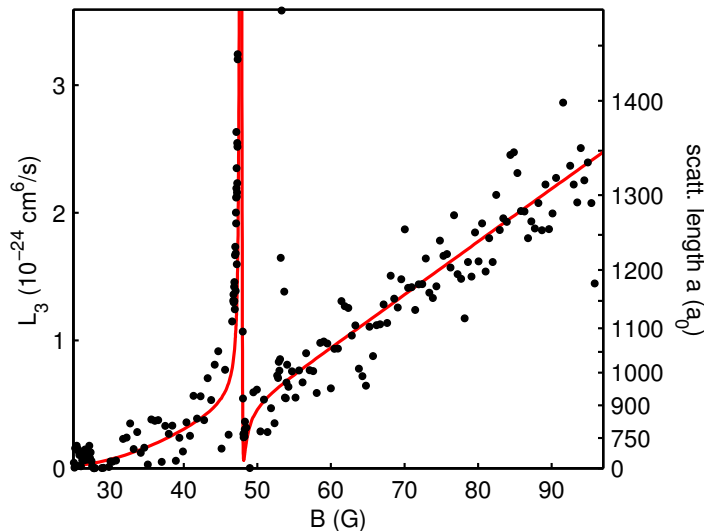


Figure 3.4: Measured values of L_3 as a function of an applied magnetic field [Web03b]. We see that for scattering lengths below $500 a_0$ the loss coefficient is relatively small.

Figure 3.4, taken from [Web], measured L^3 coefficient as a function of the bias magnetic field. Due to the strong a^4 -dependence the coefficient is relatively small for magnetic fields below the 48 G-Feshbach resonance.

We know all loss processes in the trap, hence we can describe the general loss from the trap by the differential equation:

$$\frac{\dot{N}}{N} = -\alpha - \beta\langle n \rangle - L_3\langle n^2 \rangle. \quad (3.30)$$

The first density independent term α describes the loss through background gas collisions, β summarizes all two-body loss processes and the third term represent the

three-body recombination. In the micro trap at lower densities the second term dominates the loss process, whereas the first term does not contribute to the loss on a timescale of our experimental cycle. At higher densities, especially in the degenerate regime the three-body recombination becomes more important.

3.5 Evaporative cooling

Besides laser cooling, evaporative cooling is one of the most efficient cooling methods used in the field of ultra cold atoms. With laser cooling one can reach temperatures in the range of μK without losing many atoms thereby allowing the phase-space density to be increased. In the nineties, it became clear that laser cooling had reached its limit and any further increase of phase-space density was near impossible. If the density becomes too large, light scattered by one atom is reabsorbed by another causing repulsion between them. A more promising, and up to now the only possible, route to BEC is evaporative cooling. This method was proposed in 1986 by H.Hess [Hes86] and was soon followed by an experimental realization [Mas88].

The evaporative cooling method is based on the preferential removal of atoms from the confined sample, whose energy is higher than the average energy of the sample. This first step is followed by thermalization with the remaining gas by elastic collisions. The process starts again causing the sample to cool while losing relatively few atoms. Since this cooling method relies on removing atoms, it is important that not too many atoms are removed. This would lead to a lower temperature but not increased density, while removing only a few atoms would lead neither to decreased temperature nor to higher density. In the next paragraphs I will describe which evaporation parameters are important and which conditions have to be fulfilled to achieve high evaporation efficiency.

3.5.1 Plain and Forced Evaporation

There are two cases of evaporative cooling, namely plain evaporation and forced evaporation. Plain evaporation occurs when the temperature of the sample is in the range of the potential depth of the trap which is constant during the plain evaporation process. In this case, there are many atoms which exceed the trap depth and thus can leave the trap. They carry energy away from the sample and thus cooling the sample until a temperature reaches about one tenth of the trap depth. At this point the fraction of hot atoms in the sample is small, the evaporation stops and the decay is dominated by natural lifetime of the sample. This type of evaporation takes place when the atoms are transferred from a deep to shallow trap, such as it is the case of loading the GOST or microtrap.

Forced evaporation takes place when the trap depth is lowered. This allows the atoms

with energies higher than the trap depth to escape. To sustain the cooling process the trap depth must be lowered continuously enabling a steady decrease in the temperature. In order to reach this regime, one has to keep the ratio between the truncation parameter η , which is defined by the potential boundary, and the thermal energy $k_B T$ of the sample constant. The truncation parameter is given in units of thermal energy $k_B T$ and is defined by the energy that leads to a removal of an atom from the trap.

The lowering of the potential can be implemented in many different ways. In most BEC experiments working with magnetic traps the so-called RF-evaporation technique is used. In this radio frequency photons induce transitions between trappable m_F -states into states, which can not be trapped magnetically. In optical dipole traps a forced evaporative cooling is usually implemented by lowering the dipole potential. Compared to magnetic traps, where the potential for the cold atoms remains unchanged, lowering the potential in a dipole trap can also lead to simultaneous reduction of the density since the trap becomes flatter. This fact makes evaporative cooling in a dipole trap more difficult than in a magnetic trap because with decreasing density the elastic collision rate becomes smaller and thus the atoms cannot completely thermalize.

Thermalization and Evaporation Timescale

Thermalization plays critical role in the evaporative cooling. If the elastic collision rate is too small, the ensemble cannot be thermalized and thus the evaporation process stops. In the case of cesium, which has a large cross section at low energies, there is almost no contribution to thermalization because only a little kinetic energy is transferred by them. In order to calculate the thermalization time, one first has to know the elastic collision rate

$$\gamma_{el} = \bar{n} \sigma \bar{v}_{rel} \quad (3.31)$$

with \bar{n} as the average atomic density, σ the elastic cross section and $\bar{v}_{rel} = \sqrt{16k_B T / \pi m}$ the average relative velocity between two atoms for a Maxwell-Boltzmann distribution. Using the expression for the elastic cross section, one arrives at the expression for the elastic collision rate which is dependent from the mean density and the temperature:

$$\gamma_{el} = \bar{n} \cdot \sqrt{\frac{16k_B T}{\pi m}} \cdot \frac{2(2\pi a \hbar)^2}{\pi \hbar^2 + 4ma^2 k_B T} \quad (3.32)$$

Using this relation one can determine the time needed for a thermalization [Arn97]

$$\tau_{th} = 10.7 \frac{1}{\gamma_{el}}. \quad (3.33)$$

According to this relation, there are about 10 elastic collisions needed to thermalize the atomic ensemble.

The thermalization time determines how fast the potential should be lowered to provide thermalization during the evaporation process. While lowering the potential too fast, does not allow thermalization to take place while for a slowly varying potential the losses become more important and the evaporation becomes less efficient. The faster the thermalization, the faster the potential can be lowered without affecting the efficiency. This is reflected in the relation for the evaporation rate dependent on the number of trapped atoms N [Met99]

$$\dot{N} = -N \cdot \gamma_{el} \frac{\eta}{\sqrt{2}} e^{-\eta} \quad (3.34)$$

This relation considers a three dimensional evaporation process with a large truncation parameter η which is kept constant during the evaporation. Considering the evaporation time

$$\tau_{ev} = \frac{\sqrt{2}e^\eta}{\eta} \cdot \frac{1}{\gamma_{el}} \quad (3.35)$$

we see that for a large truncation parameter the collision rate must be large to provide an efficient evaporation. The η -dependence originates from the Boltzmann-distribution which determines how probable the production of an atom with high energy is.

3.5.2 Evaporation Efficiency

In order to be able to optimize the shape and the speed of the evaporation ramp one has to know the efficiency of the evaporation process. From this the gain of the phase-space density can be calculated for a given number of atoms. The larger the number, the more efficient the evaporation process. The evaporation efficiency is defined by

$$\epsilon \equiv \frac{\ln(\frac{D'}{D})}{\ln(\frac{N}{N'})} = 3 \frac{\ln(\frac{T}{T'})}{\ln(\frac{N}{N'})} - 1 \quad (3.36)$$

where D and D' denotes the phase-space density at the beginning and the end of the evaporation respectively, while N and N' are the corresponding atom numbers and T and T' the temperatures. Using the right hand side of the expression, the efficiency can be calculated directly using the measured quantities T and N . The expected efficiency in a harmonic potential is given by $\eta - 3$ under the assumption that the atoms leave the trap isotropically. For a three dimensional RF-evaporation used in the most BEC-experiments efficiencies of about three have been reached. This corresponds to a 1000-fold increase in the phase-space density for each order of magnitude of lost atoms. In section 6.1 we will see that for evaporative cooling in our micro trap the evaporation efficiency is in the range of two. This relatively small efficiency can be explained by the reduced dimensionality of the evaporative cooling process in the dimple trap.

To maximize the evaporation efficiency one must find the right rate of decreasing of the potential depth. This rate is determined by several factors. As already mentioned, the elastic collisions play a crucial role, but in a real experiment there are also inelastic collisions which lead in most cases, to losses. These types of collisions are called "bad" collisions, while the elastic ones are called "good". When the ratio of "bad" to "good" collisions is small, the loss rate is small compared to the timescale of the thermalization and a large truncation parameter can be chosen in order to achieve a large efficiency. In the case of large loss the truncation parameter has to be small. This usually leads to small evaporation efficiencies, because the atoms can not fully thermalize. If the elastic collision rate increases during the evaporation, a process called *runaway evaporation*, takes place which usually has a large efficiency and is reached in three dimensional evaporative cooling.

3.5.3 Dimensionality of the Evaporation

In the previous subsection we have that the evaporation is based on the selection of atoms above a certain total energy E . But it is possible that not all atoms above this energy leave the trap and only those which move in the direction in which the potential has been lowered, atoms moving in other directions remains disregarded. Evaporative cooling is called one dimensional when the selection is based on $E_z > \eta k_B T$, two-dimensional for $E_x + E_y > \eta k_B T$ and three-dimensional for $E > \eta k_B T$. In the case of evaporative cooling in our micro trap or the GOST, we have two-dimensional evaporation when the horizontal potential is lowered by reducing the power of the dimple laser or the hollow beam respectively. In this case the evaporation takes place only in the horizontal plane and the energy of the atoms in the vertical direction is in the first instance not influenced by the evaporation. However, elastic collisions play an important role for the cooling of the vertical degree of freedom. The evaporation is always three-dimensional if the ergodic coupling between the different degrees of freedom is faster than the time between elastic collisions. In most traps the ergodic mixing is slow compared to the typical collision time of few milliseconds.

The reduced dimensionality of the cooling leads to a dramatic reduction in the efficiency because the major fraction of the atoms with enough energy to escape collide with other atoms and increase their kinetic energy. These slow the process of atoms leaving moving in the direction which is not cooled. In principle, this can only increase the evaporation time and should not affect the evaporation efficiency, but the evaporation time is limited by inelastic processes and thus 1D or 2D evaporation always exhibits a reduced efficiency.

The reduced efficiency can be explained by considering the atoms in velocity space. While in 3D evaporation the evaporating atoms are mainly from a shell with velocities between $\sqrt{2\eta k_B T/m}$ and $\sqrt{2(\eta + 1)k_B T/m}$, the volume of the shell with a z-component

of the velocity larger than $\sqrt{2\eta k_B T/m}$ is reduced by a factor of 4η compared to the whole shell. In the case of 2D evaporation one obtains a reduction in the number of collisions per evaporation by the factor of $3\sqrt{\eta}/2$ compared to the three-dimensional case.

The reduction of the efficiency could be observed experimentally by comparing the evaporation rate for different dimensions of the evaporation. In [?] axial and three-dimensional evaporation in a magnetic trap have been compared. It was observed that the axial evaporation rate was a factor of about 30 smaller than in the 3D case. In another experiment [Wu96] compared 2D with 3D evaporative cooling where the phase-space density increase in the 3D case was a factor of 20 higher than in the 2D case, and the fraction of atoms which remained was three times higher.

In the micro trap we observe a relatively small efficiency which can be explained by the reduced dimensionality of the evaporation. A three dimensional evaporation could be realized by simultaneous ramping down all trapping potentials. However it was observed that lowering the power or increasing the detuning of the evanescent wave laser led to increased losses. This effect, caused by the fact that imperfections in the evanescent wave becomes more important at lower intensities or larger detunings of the evanescent wave, makes efficient three-dimensional evaporative cooling in a micro trap impossible. In former measurements we have realized one-dimensional evaporative cooling in the GOST, where the detuning of the evanescent wave was ramped up [Ryc00]. The efficiency was visibly smaller than what we observe for the two-dimensional case in the micro trap.

Chapter 4

Experimental Setup

It is remarkable that in our experiment we keep an atomic cloud at almost absolute zero temperature about one micron above a glass surface which is factor 10^{10} warmer. The sample seems to be undisturbed by the hot environment for many seconds. In order to achieve these conditions one has to meet many stringent requirements in the experimental setup. The experimental setup consists of three main elements: the vacuum system ensures perfect isolation between the gas sample and the apparatus, the laser system makes the cooling and trapping of the atoms possible and finally, the experimental control guarantees precise management of the many experimental cycles. In this chapter I will introduce all elements of the experimental setup.

4.1 Vacuum System

The first stage of building a laser cooling experiment is the vacuum system. The cold atoms have to be isolated from the laboratory environment and against the “hot” air molecules. Only under ultra high vacuum (UHV) conditions it is possible to store the atoms for a long time, on the other hand, one need a high flux of Cs-atoms to load the trap quickly. This problem is solved by an oven and the Zeeman slowing technique (Section 4.2). The oven is separated from the experimental section by a differential pump section. In this way it is possible to maintain a pressure gradient of up to three orders of magnitude between the source of atoms and the experimental section. A photograph and schematic overview of the complete apparatus is shown in figure 4.1.

To obtain vapor Cs-atoms we heat dispensers, 4 cm long metallic sticks with chemically bounded cesium-133, up to few hundred degrees. The temperature and thus the released number of Cs-atoms is controlled by an electrical current of about 4 amperes through the dispensers. At an oven temperature of 85°C exists a vapor pressure of 10^{-4} mbar. To create the effusive atomic beam, the atoms are sent through a 2 mm diameter hole. After passing through a 6-way-cross, which hosts an inverted magnetron,

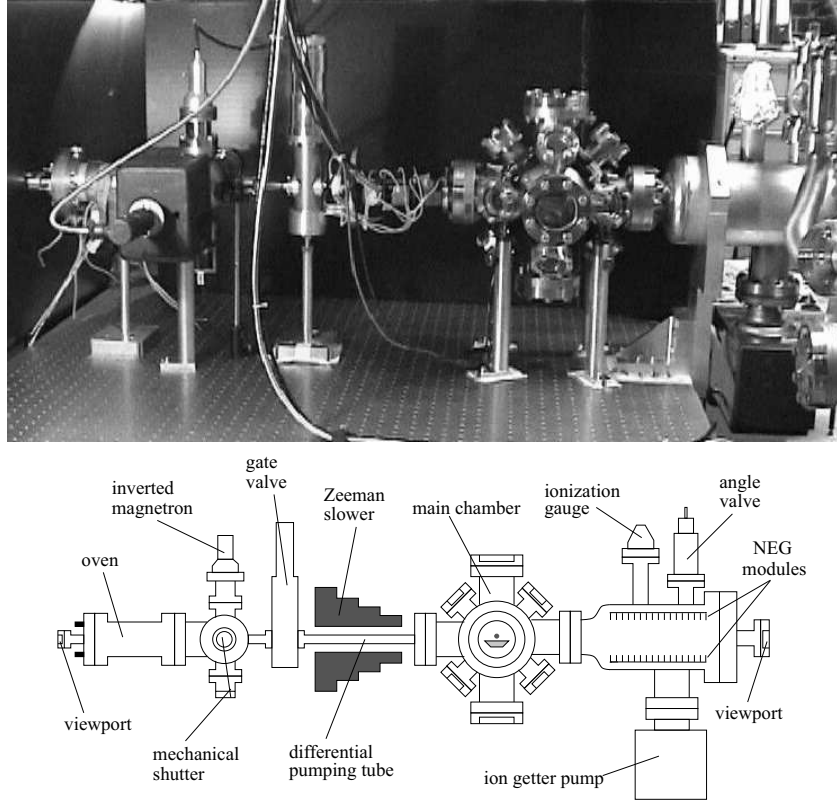


Figure 4.1: *Picture and schematic drawing of the vacuum apparatus. The experiment takes place in the large main chamber, where the fused silica prism is situated.*

an ion-getter pump and a mechanical shutter driven by a step-motor, the atomic beam propagates through a short flexible tube, introduced to allow the possibility of aligning the atomic beam with the experimental section. A valve is used to connect the oven section with the differential pump section, which consists of 45 cm long tube whose diameter increases in five steps from 4 mm up to 9 mm. This section maintains the large pressure gradients between the oven section and the main chamber, where a pressure of less than 10^{-11} allows atoms to be stored the atoms for several minutes. This part also hosts the Zeeman slowing section described in section 4.2. The atomic beam provides a source of about 10^8 relatively cold atoms per second directly in the main chamber.

The main part of the apparatus is the spherical stainless-steel chamber, which is connected to the differential pump section through a big opening. On the opposite side of the entry point of the atoms is a 5 cm diameter opening for the pump section. Its purpose is to maintain the UHV in the main chamber and to remove atoms which

could not be trapped in the MOT. Two pumps provide sufficient pump power. A pair of Non-Evaporative-Getter modules (NEG-modules) provide the majority of the pumping power and are supported by an ion-getter pump attached to the bottom of the apparatus. Additionally, the pump chamber hosts a valve to connect a turbo pump and a UHV-gauge. Finally, a viewport situated at the end of the pump chamber serves as entry point for the Zeeman slowing laser which is overlapped with the atomic beam. To obtain a good optical access into the main chamber, there are 16 anti-reflection coated viewports to allow access for several different lasers into the chamber and to detect the fluorescence from the atoms using a CCD-camera.

The central element of the GOST, the fused silica prism, lies 0.5 cm below the center of the main chamber. The prism shape allows us an easy generation of the evanescent wave at the prism surface. The prism has a 4×5 cm surface and trapezoidal base line and is fixed in place with a titanium holder which sits on the bottom viewport of the chamber. Both angle sides and the bottom surface are anti-reflection coated for 852 nm and 1064 nm to reduce scattered light. To prevent any unwanted interference effects of the evanescent wave and additional bumpiness, the upper surface is left without coating.

4.2 Magnetic Fields

Magnetic field plays an important role in the experiment, therefore precise control of all fields is very important. The Zeeman slower requires a magnetic field, which compensates for the Doppler shift as the atoms are decelerated during their flight through the differential pump section. The four coils are placed coaxially around the tube. The resulting magnetic field and the Zeeman slower enables us to slow the atoms from the initial few hundred meters per second to the capture velocity of the magneto-optical trap sitting in the main chamber.

The magnetic field required for the MOT is generated by two coils each of 250 windings, wound directly on the outer surface of the chamber. The coils are placed 9 cm apart from one other and are connected in an anti-helmholtz configuration. The coil axis lie perpendicular to the axes defined by the atomic beam and gravity. Optimum current for loading the MOT was found to be 4 A corresponding to a field gradient of about 20 Gauss/cm. This field is kept constant during the loading and the transfer of the MOT.

In order to be able to create a homogenous magnetic field in each direction and thus to change the position of the field-zero of the gradient, there are three pairs of additional coils attached to the viewports in the three perpendicular directions. This magnetic coils enable us to compensate for the earth's magnetic field and to change the position of the MOT specially. This is important when loading the GOST. We use the vertical coils for generating a guiding field needed for polarizing the atoms. To maintain the polarization of the atoms, this magnetic field of about 1 Gauss is applied while the

atoms are trapped in the micro trap.

To tune the interaction between the Cs-atoms via homogenous bias field, we need a strong homogenous magnetic field in the center of the experimental chamber. Such a field parallel to gravity is provided by two coils 30 cm apart, each with 200 windings. A programable power supply (Delta SM 45-70D) provides up to 45 A, corresponding to a magnetic field of 90 Gauss. The heat produced by the coils is in total about 200 W at typical operating currents of 21 A and is dissipated by water cooling. The current can be switched from the typically operating current 21 A to 0 A within about 10 ms, but because of eddy currents it takes slightly longer to switch the magnetic field in the chamber. The magnetic field is controlled by the analog input of the power supply with an accuracy of about 17 mG.

Finally, another pair of coils is used in this experiment. To magnetically levitate the atoms, there are two coils wound in the same manner as the coils for the MOT on to the chamber. In this case, the coil axes is parallel to gravity. The coils have 30 windings each, the copper wire used has a diameter of 2,4 mm enabling high currents to be carried. The coils are connected in an anti-helmholtz configuration and provide a vertical B field gradient of 31.3 G/cm necessary to compensate for gravity for the cesium atom in its ground state. The 90,8 A needed for this field is provided by a programable power supply (Delta SM 30-100D). Since it would be technically very difficult to cool both these coils, they can not be driven at 90,8 A for longer than few seconds. During the experimental cycle the coils are switched on for about 100 ms and have then about 15 s time to cool down. Their temperature does not normally exceed 35° C.

4.3 Laser Setup

The various laser systems play a central role in the experiment. Altogether 10 different lasers with wavelengths between 532 nm and 1060 nm are used for the three traps. They are used to decelerate, cool, trap and image the atoms. Those lasers whose wavelengths are few ten of MHz from the atomic resonance must be temperature od current stabilized, or a combination of both, while those whose wavelengths are 200 nm from resonance do not need any form of stabilization. This fact shows the wide spectrum of laser used in our experiment. The following section introduces all lasers associated with the different traps. Many parts of the experimental setup have been explained in more detail in previous works [Man99, Ryc00].

4.3.1 MOT Lasers

The magneto-optical trap, first realized in 1997 [Raa87], is nowadays a standard trap in every laser cooling experiment. It is used to collect and pre-cool atoms in a relatively easy way and without a large effort. A MOT loaded with a decelerated atomic beam has

two big advantages compared to other schemes [Mon90]. First, the loading is achieved within few seconds and the second and more important point is the UHV conditions are preserved since the atoms do not have to be loaded from the background gas. The MOT bridges, due to its large capture velocity, the huge temperature difference between the atomic beam and an atomic cloud. But to ensure a constant source of cold atoms for many hours stable it needs stabilized laser sources. How this stabilization and the laser setup work will be briefly explained in following paragraphs.

Laserdiodes

The laser light used for the MOT, the Zeeman laser, all repumper beams, the evanescent wave, hollow beam and the polarizer laser beam are provided by DBR-laser diodes (SDL-5712-H1). These laser diodes are easy to use because they do not employ any external gratings to stabilize them. Instead a layer of spatially periodical index of refraction material right behind the laser-active semiconductor selectively reflects light of a narrow frequency band back to the laser medium and thus passively stabilizes the frequency to a within few ten MHz. The wavelength can be tuned about 2 nm by changing the current or the temperature of the laser medium. While tuning the temperature changes the frequency over a wide range at a rate up to ~ 70 GHz/s, modifying the laser current allows fast frequency modulation between kHz-MHz within a small frequency interval. The temperature is stabilized using an integrated peltier element. The diode currents of the near-resonant lasers for the MOT and Zeeman laser are used to actively lock the laser frequencies to atomic references. The diode currents of the lasers for hollow beam and the evanescent wave are not stabilized since the frequency changes due to fluctuations are much smaller than the detuning in the range of many GHz. The lasers provide up to 90 mW at 852 nm at a current of 150 mA with a spectral width of the laser line of typically 10 MHz.

Optical Setup and Frequency Lock

Since the MOT is the original atomic for the GOST and thus the microtrap, the number of atoms in the MOT has to be kept as stable as possible to avoid fluctuations in number of atoms entering subsequent traps. Beside the magnetic field which can be sustained easily for longer time, the frequencies of the lasers required for the MOT are very critical with respect to number and temperature of the trapped atoms. As the typical experimental cycle takes up to several hours, longtime drifts are unwanted as well as frequency changes on the second scale.

The MOT laser and the Zeeman slower laser, providing the laser light for the closed transition $F = 4 \rightarrow F' = 5$ are frequency stabilized by a beat lock with an additional *master* laser. The obtained beat signal between these lasers is detected on a fast photodiode, mixed down and compared to the frequency from a stable voltage-controlled

oscillator. The master laser is a 852 nm-laser diode (SDL-5429) which is frequency locked 170 MHz below the $F = 4 \rightarrow F' = 5$ transition. It is stabilized by using an external Littrow-type extended-cavity setup for slow frequency changes while changing the current allows fast frequency adjustments. The stabilization is based on a modulation transfer spectroscopy, where the beam passes through a cesium vapor cell and delivers in this way a robust and Doppler-free signal. The master laser has a frequency width of 100 kHz with no significant long-term drift.

The beam of all lasers, except of the master laser, has to be then collimated and shaped by a pair of prisms before it passes through a optical diode. Two beams are extracted from the main beam. One of these passes through a saturation spectroscopy setup and is then detected on a photodiode whose signal serves as a frequency reference. The remaining beam is overlapped with the beam from the master laser and a fast photo diode detects the beating signal of about two hundred MHz which is translated into a RF-signal. This signal is then processed by several electronic circuits [Ham02a] to obtain an error signal that features a steep slope and an adjustable zero crossing at the desired laser frequency. Now, we have a stable laser source whose frequency ranges from -122 MHz up to +44 MHz with respect to the $F = 4 \rightarrow F' = 5$ transition. The MOT laser is tuned 8 MHz and the Zeeman laser 25 MHz to the red. Finally, both lasers are coupled into a polarization maintaining optical fibre to transport the light to the experiment which is located on a separate optical table to prevent scattered light from any near-resonant laser entering the dipole trapping stage.

The laser light for the repumper is derived in a similar manner to the MOT-laser. Since the frequency of the repumper laser beam is not critical, we control the laser by saturation spectroscopy and stabilize it by fm-modulation spectroscopy, which guarantees a stable frequency for many hours. Since we use the repumper laser for the polarizer laser we use an AOM to switch the laser beam before the laser beam is coupled into a polarization maintaining optical fibre. In order to remove residual stray light we use a mechanical shutter.

MOT Geometry

Once the frequency stabilized laser beam has been brought to the experimental table it has to be divided and brought to the apparatus. An advantage of using a fibre is, beside the clean gaussian mode, the fact that the apparatus is completely, geometrically decoupled from the optical setup and the MOT geometry must not be adjusted after making a change at the optical setup.

Separate fibres are used for the beams driving the MOT-cooling and MOT-repumping transitions, while both Zeeman slower beams are coupled into one fibre. Both MOT-beams are overlapped at a polarizing beam splitter cube after they have been collimated to a waist of 0,7 cm. The beam is then split into five separate beams, four of them are directed perpendicularly to the axis of the MOT coils into the experiment chamber

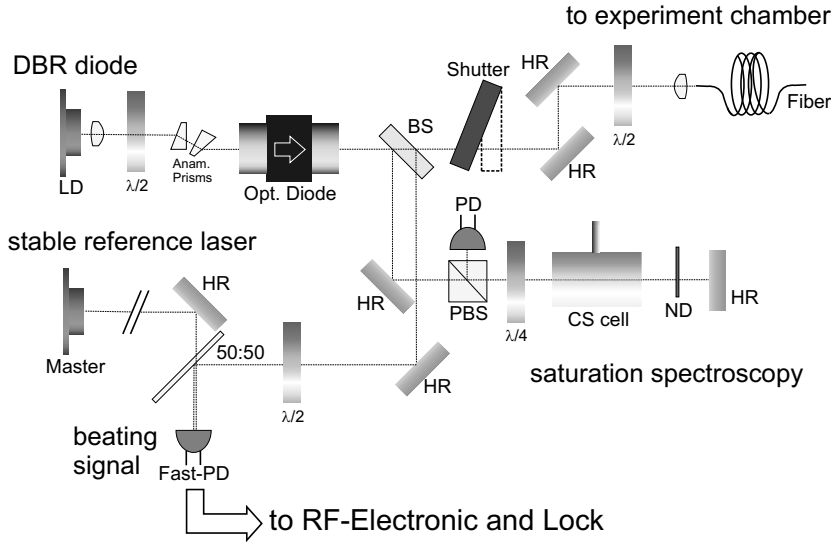


Figure 4.2: *Optical setup of the MOT- and the Zeeman slowing laser. The laser light is then guided to the experimental table by an polarization maintaining optical fibre.*

while the remaining beam enters the chamber horizontally and is retro-reflected. In this configuration the intersection of the six beams lies about 0,5cm above the center of the prism surface and coincides roughly with the zero-point of the MOT-quadrupole field. The intensity of each beam is about 10 mW/cm^2 which is 9,4 times the saturation intensity of cesium.

The combined cooling-repumping beam of the Zeeman slower enters the apparatus through a small viewport at the front of the pump chamber and is formed in such a way to allow optimal overlap with the counter propagating atomic beam. The 30 mW beam is circularly polarized and is controlled by a shutter at the entrance of the viewport.

4.4 The Gravito-optical Surface Trap

More than 10^8 atoms can be trapped and pre-cooled down to $10 \mu\text{K}$ in the MOT. After the transfer into the Gravito-Optical Surface Trap (GOST) the MOT-laser and the MOT magnetic field are switched off and the atoms are trapped by two respectively three other lasers. One laser produces the evanescent wave providing vertical confinement and the Sisyphus cooling process described in the next chapter, the hollow beam confines the atoms laterally and finally, the repumping laser which is important for the cooling mechanism. Which role each laser plays and how the hollow beam and the evanescent waves are produced will be described in the following paragraphs.

Evanescent Wave

The bottom of the GOST is illuminated by a 150 mW-laser diode similar to the one used for the MOT and Zeeman slower. The temperature of this laser is stabilized and is during its operation set to a constant value. Active frequency lock is not necessary in this case because the detuning of 2 GHz to the blue with respect to the $F = 3 \rightarrow F'$ -transition is much larger than the passive stability of the laser diode which is approximately few ten MHz. The laser light is first shaped using anamorphic prisms before passing through an optical diode to prevent back reflection to the laser. A 200 MHz acousto-optical modulator (AOM) enables us to switch the laser beam very quickly which is needed to measure the ensemble temperature. Directly behind the AOM, the beam passes through a heated filter cell, which is necessary to remove any laser sidebands which would otherwise cause heating in the GOST. Since a circular laser beam would appear

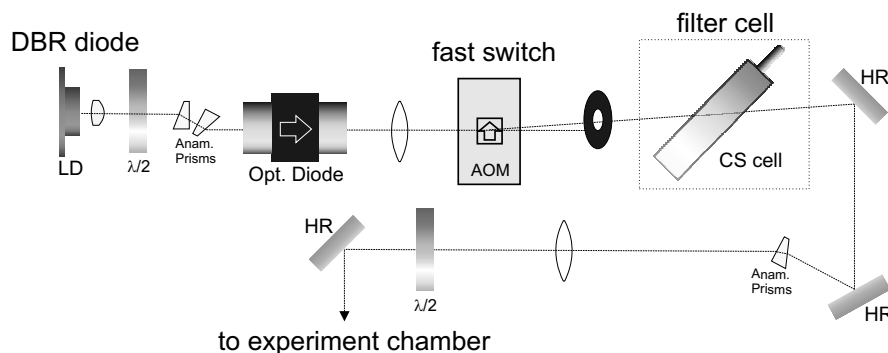


Figure 4.3: *Optical path of the evanescent wave laser beam. The laser light passes a heated Cs-filter cell in order to filter out resonant photons.*

at the surface as a elliptical spot, it must be shaped by a prism to yield a circular evanescent wave spot on the prism surface. A lens focusses the beam to a waist of $700 \mu\text{m}$ and finally a half-waveplate sets the polarization to TM in order to increase the evanescent wave intensity. The beam is then shone into the chamber and undergoes a total internal reflection from the prism surface. The peak dipole potential in the center of the spot is $U/k_B = 1.65 \text{ mK}$.

Hollow Beam

The hollow beam provides horizontal confinement. To generate such a ring-shaped focus we use axicon optics which create light walls of a focus quality comparable to a Laguerre-Gaussian beam of the order 100. In former experiments [Man99, Ryc00, Ham02a] the hollow beam has been operated at a power up to 800 mW and detunings between 1

and 3 nm to avoid detrimental heating photon scattering. In the current setup two DBR-laser diodes at much lower detunings and power provide the laser light required. The laser beams are superimposed on a polarizing beam-splitter after passing through a optical diode and the collimation optics before being coupled into an optical fibre. The single-mode fibre generates a clean transverse electro magnetic mode ($TEM_{0,0}$), which is important for generating the hollow beam. Figure 4.4 gives a schematic overview of the optics used to create the hollow beam.

The light is first collimated and again focussed to an intermediate image plane by two achromatic lenses (AC). The axicon behind these lenses creates the ring-shaped focus. To remove stray light from the inner part of the hollow beam, a circular metallic coating of almost the same size (dark spot) as the ring focus on a glass substrate is placed inside the ring in the first image plane. This plane is then imaged onto the prism surface in a near 1:1 image by two achromatic lenses.

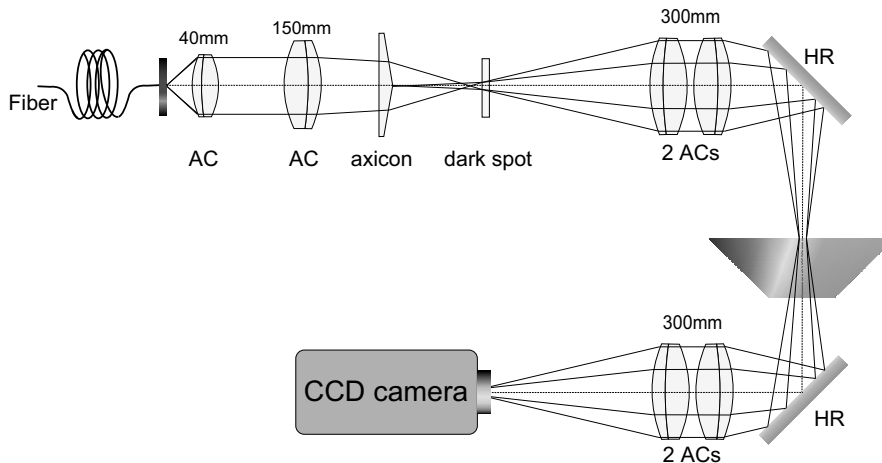


Figure 4.4: *Optics for the hollow beam. A single mode fibre produces a clean Gaussian mode is needed to generate a ring shaped focus by the axicon optics.*

After the light passes through the chamber it is identically imaged for alignment purposes on a CCD-chip of a monitor camera. This camera enables the positioning of the hollow beam, the evanescent waves and the dimple laser. It also indicates where on the prism surface there are impurities which would lead to a shortening of the lifetime in the GOST.

The laser power at the prism surface of both laser beams is 20 mW and 25 mW and the detuning is 37 GHz and 85 GHz respectively. The unequal values for the laser power are caused by the different fibre-coupling efficiencies due to differing astigmatism of the laser diodes. The values for the detuning arise after optimizing the atom number in the GOST. The diameter of the hollow beam with $1/e^2$ -wall thickness of about $20 \mu\text{m}$ is $820 \mu\text{m}$. This amounts to a total potential depth of both lasers of $U/k_B = 93.2 \mu\text{K}$.

Repumping Beam

Both lasers described so far are used for trapping of atoms, but for efficient Sisyphus-cooling an additional laser is required. This repumping beam transfers atoms which have decayed during the cooling cycle into the $F = 4$ state back into the $F = 3$ ground state to close the cooling cycle. This laser beam is resonant with the $F = 4 \rightarrow F' = 4$ transition and is applied during the GOST phase. A few microwatts are derived from the Zeeman laser beam and shifted 225 MHz to the red by using an AOM. The beam is guided by an optical fibre to the experimental table and is focussed into the GOST region from above.

4.5 Dimple Trap

The GOST prepares a sample of cold atoms close to the prism surface. Due to the light assisted inelastic collisions a further increase of the density is only possible in the presence of strong loss mechanisms. Therefore it is necessary to use far detuned laser fields in order to reduce light induced loss processes. After the atoms have been prepared by the GOST, they can be transferred into dimple trap. The dimple trap is a micro trap, where the atoms are kept in regions of maximum laser intensity. The dimple trap consists of a far blue-detuned evanescent wave and a focussed red-detuned laser beam, described in the following paragraphs.

Far-detuned Evanescent Wave

The beam for the evanescent wave is typically blue detuned 2-15 nm from the resonance and is derived from a typically 2-15 nm blue-detuned titanium:sapphire laser which is pumped by a 10 W-laser at 532 nm (Coherent Verdi V-10). To be able to switch the laser beam within a few microseconds it passes through an AOM. Because thermal effects in the AOM change the plane of polarization of the linear polarized laser beam, the laser beam has to pass through a polarization beam splitter to ensure a stable plane of polarization. This is important since any deviation in the polarization has a dramatic effect on the evanescent wave potential. To avoid these thermal effects, where the RF-signal changes the temperature of the AOM and thus its diffraction properties, the AOM is switched off only for temperature measurements and when taking pictures of the recaptured atoms. In this way the temperature of the AOM crystal, subsequently, the plane of polarization can be kept constant during the experimental cycle. Two lenses focus the beam to a size of $500 \mu\text{m}$ at the prism surface while a half-wave plate sets the TM-polarization. The angle of incidence is set 0.2° degree above the critical angle leading to a decay length of $\Lambda = 1.4 \mu\text{m}$. This values corresponds at a detuning of 13.2 nm and a power of 700 mW, to a maximum potential height of $U/k_B = 50 \mu\text{K}$ in the center of the evanescent wave.

1064 nm-laser

The beam for the horizontal confinement is derived from a 10 W Yb-fiber laser. This laser has the advantage that it possess a clean gaussian mode due to the single mode optical fibre. The optical setup is depicted in figure 4.5. After the laser beam leaves the collimation optics and its plane of polarization is rotated vertically by a half-waveplate, it is focussed into the AOM. The AOM allows us fast switching of the beam and exact controlling of its intensity and its angle of refraction. Changing the RF-frequency coupled into the AOM leads to a changing of the refraction angle and thus the position of the dimple at the prism surface. The modulation of the position of the dimple enables us to measure the horizontal trap frequency. The beam then passes through two lenses and is reflected into the vacuum chamber by a mirror underneath the apparatus. The first lens of the telescope is mounted at linear positioning stage (Physical Instruments MP42E) and can be moved over a distance of 50 mm with a precision of a few micrometers. The stage is controlled by a computer and is able to change the focus size on the prism surface between about 40 – 150 μm within a few seconds. To avoid changing the horizontal position of the focus at the prism surface during movement of the stage, the optics have to be exactly aligned.

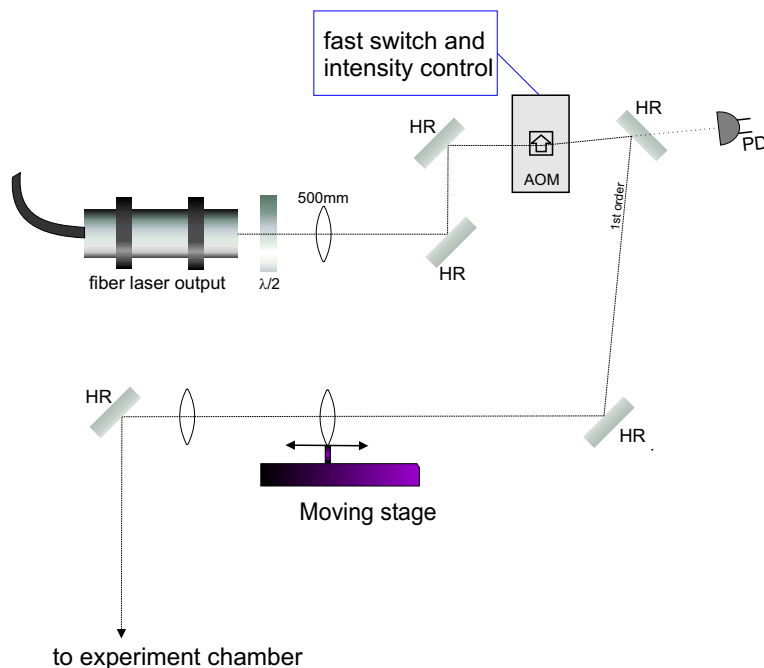


Figure 4.5: Optical setup for the dimple laser. The intensity of the dimple beam is controlled by a logarithmic photodiode and an AOM. The waist of the dimple can be changed by moving the focussing lens.

One of the most important parts in the optical setup is the AOM. It is used for fast switching of the laser beam which is important for studying of the horizontal expansion of the atoms. Furthermore, it is used to implement evaporative cooling by reducing the laser intensity in a controlled fashion. For this purpose a photodiode detects the signal of the laser beam and feeds it back to a control unit which is connected to the computer in order to give the shape of the intensity ramp. The required signal is then sent as a RF-signal to the AOM. We use a logarithmic amplifier (AD8305) to be able to detect the intensity of the laser light over a range of almost four decades. The fiber laser provides up to 5 W, together with a waist of $120\ \mu\text{m}$, results in a horizontal potential of $U/k_B = 45\ \mu\text{K}$ which is in the same range as the vertical one.

Polarizing Laser

For evaporative cooling in the dimple trap we pump the atoms into the lowest spin state $F = 3, m_F = 3$. In this state we can utilize the favorable scattering properties of cesium. The atoms are polarized by a 5 ms long pulse of a few ten nW circularly polarized (σ^+) light which is sent parallel to the guiding magnetic field into the chamber. To generate a clean circular polarization, we use a polarizing beam splitter and $\lambda/4$ -waveplate directly before the laser beam enters the chamber. The beam is branched off from the MOT-repumper laser beam ($F = 3 \rightarrow F' = 3$ -transition) and shifted by a 150 MHz-AOM, first to the $F = 3 \rightarrow F' = 2$ -transition, and then back to the $F = 3 \rightarrow F' = 3$ -transition by an other AOM. This allows fast switching of both the MOT-repumper and the polarizing beam. Finally, the laser beam is transferred by an polarization maintaining optical fibre to the experimental table.

Chapter 5

Trap Properties and Measurement Procedures

In this chapter I will explain how we shape the lasers in order to cool and trap the cesium atoms. In Section 5.1 I will describe the gravito-optical surface trap and the Sisyphus cooling mechanism. Section 5.2 focusses on the dimple trap and its properties. Then Section 5.3 explains all procedures we use to measure important quantities such as atom number, temperature and trap frequency of the atomic sample. Finally, the principle of levitation and Feshbach spectroscopy will be explained.

5.1 Gravito-optical Surface Trap

The gravito-optical surface trap (GOST) serves as a reservoir of cold and dense atoms. The big advantage of the GOST is that, it cools and stores the atoms few micrometers above the prism surface, so the atoms can be easily transferred into the surface micro trap, where the main part of the experiment happens. The walls of the GOST, which can be described as an optical mug, are generated by a hollow beam, while the vertical confinement is provided by a repulsive evanescent wave. The GOST is loaded directly from the MOT by releasing the atoms, after being compressed, from a height of about 0.5 mm above the prism. About 20 million cesium atoms are cooled by Sisyphus-cooling, based on inelastic reflections at the evanescent wave, to temperatures below ten microkelvin. In this section I will explain the potentials, properties and the cooling mechanism of the GOST.

The bottom of the optical mug is generated by a blue-detuned evanescent wave. This hard wall potential and the long-range gravity potential create a wedge-potential in the vertical direction. The evanescent laser beam has a detuning of 2 GHz with respect to the $F = 3 \rightarrow F'$ -transition and a power of about 55 mW. The beam is focussed to a size ($1/e^2$ -radius) of $700 \mu\text{m}$ at the prism surface. The angle of incidence is set to 1°

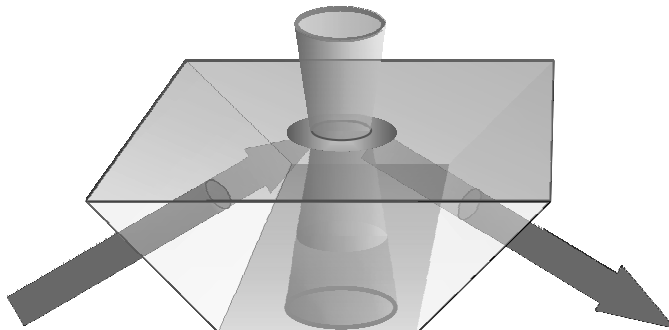


Figure 5.1: *The most important part of the experiment is the prism, which enables us to generate an evanescent wave, which serves as a bottom of the GOST. The hollow beam avoids horizontal escape of the atoms.*

from the critical angle ($\Theta_{crit} = 43.6^\circ$), this corresponds to a decay length of 700 nm. All these parameters create a total potential depth at the center of the evanescent wave of $U/k_B = 780 \mu\text{K}$.

To trap the atoms horizontally, the evanescent wave spot is superimposed with a hollow beam. The diameter of the hollow beam is $820 \mu\text{m}$. Due to the relatively sharp $20 \mu\text{m}$ thick walls, the hollow beam can be considered as a cylindrical box potential. The total potential provided by two diode lasers of $93 \mu\text{K}$ is equal to the potential depth generated by the far detuned laser beam as described in [Ham02a]. To prevent heating due to photon scattering from the hollow beam, the beam was derived at earlier stage of the experiment from a 1 nm to the blue detuned titanium:sapphire laser which was also used for the evanescent wave of the micro trap. Since in the present experiment the titanium:sapphire laser is used for the evanescent wave of the dimple trap only, it is set to a fixed detuning of 15 nm. Since it is unfortunately technically not possible to change the detuning during the experimental cycle, we would need 15-times more power to generate at this detuning the same depth of the horizontal potential. For this reason in the present experiment there are two laser diodes, operating much closer to the $F = 3 \rightarrow F'$ -transition, for the horizontal confining. It turned out that we trap in the GOST the same number of atoms at a temperature of about $10 \mu\text{K}$ as we trapped with the far detuned hollow beam. The reason for the almost unchanged conditions in the GOST may be the smaller detuning of the evanescent wave leading to higher cooling rate. Figure 5.1 shows the geometry of the GOST. The size of both beams is not scaled, in fact the prism width is 50 times larger than the diameter of the GOST. Nevertheless, the trap volume in the range of cubic millimeters is large enough to trap a relatively big sample of cold atoms.

Cooling in the GOST

As the atoms see in the evanescent wave a repulsive wall, they are reflected like on a trampoline. Most reflections are completely elastic, where the atoms do not lose their kinetic energy, but sometimes an atom is reflected inelastically. Inelastic reflections on the evanescent wave are the basic principle of the Sisyphus cooling mechanism. Figure 5.2 shows the simplified level scheme of the cesium atom and the details of the cooling cycle. Since the detuning of the evanescent wave is smaller than the hyperfine splitting of the ground state of 9.2 GHz, but much larger than the splitting of the excited state manifold, the cooling cycle can be described by means of a three level system.

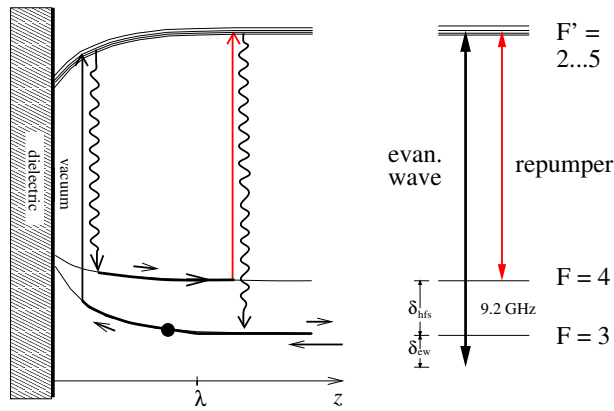


Figure 5.2: Illustration of the sisyphus cooling mechanism in the GOST. The dot represents the atom approaching the surface and the arrows show its path during the cooling process. When the atom is pumped by an evanescent wave photon into the upper hyperfine state it has to be pumped back by an weak repumper laser to close the cooling cycle.

Before the atoms are released into the GOST, they are pumped into the lower hyperfine state $F = 3$, so it can be assumed that the most atoms approach the repulsive wall in this state. Due to the blue detuning of the evanescent wave, the atoms have to climb a potential hill as depicted in the scheme. In most cases the atoms stay after elastic reflection in this same state. Since there is no change in kinetic energy, the temperature of the sample doesn't change. An inelastic reflection takes place when the atom is pumped into the upper hyperfine state $F = 4$ by a evanescent wave photon while in the intense light field. Since the lifetime of the $6P_{3/2}$ state of 30 ns very short compared to the bouncing frequency of about 1 kHz, the atom leaves the evanescent wave field in the $|F = 4\rangle$ state. The atom returns in a less repulsive potential and thus its kinetic energy is transferred into internal energy by the pump process. To calculate the mean energy loss ΔE_{\perp} , the reduction of the potential energy according to the ratio of the detunings $\delta_{EW}/(\delta_{EW} + \delta_{HFS})$ has to be taken into account. The mean energy

loss during such a cooling cycle is found to be $\Delta E_{\perp}/E_{\perp} = -\frac{2}{3}\delta_{HFS}/(\delta_{HFS} + \delta_{EW})$, where $E_{\perp} = mv^2/2$ is the kinetic energy of the incoming atom. To close the cooling cycle and to prevent releasing of the internal energy into kinetic energy, the atom has to be pumped back into the $|F = 3\rangle$ -state. A very weak laser beam, resonant on the $F = 4 \rightarrow F' = 4$ -transition, pumps the atom back in to the ground-state. The intensity of the GOST-repumper plays a major role for the cooling efficiency. A strong GOST-repumper pumps the atoms back in to the $F = 3$ -state immediately after arriving in the upper hyperfine state, so they exit the reflection in the ground state. On the other hand a weak GOST-repumper doesn't close the cooling cycle and the internal energy can be inverted into kinetic energy. To calculate the cooling rate, one has to consider the probability for a cooling reflection p_{cool} , the mean relative energy and the reflection rate ν_{refl} . The result can be written as:

$$\beta = p_{cool} \cdot \frac{\Delta E_{\perp}}{E_{\perp}} \cdot \nu_{refl} = \frac{q}{3} \cdot \frac{\delta_{Hfs}}{\delta_{EW}} \cdot \frac{mg\Lambda}{\hbar(\delta_{EW} + \delta_{Hfs})} \cdot \Gamma. \quad (5.1)$$

Here q denotes the probability of a scattering process ending in the upper hyperfine state ($q=0.25$), m is the cesium mass, Λ is the decay length of the evanescent wave and Γ is the natural line width of the transition. Now we can calculate the cooling rate: at a detuning of 2 GHz and a decay length of $0.7 \mu\text{m}$ the average cooling rate is $\beta \approx 2.6 \text{ 1/s}$.

To determine the temperature limit of the cooling mechanism, we have to consider the cooling and the heating rate. To get the expression for the temperature limit, we have to count the number of scattered photons per cooling reflection and multiply this with the rate at which such a process occurs. We then obtain a temperature limit of:

$$T_{min} = \left(\frac{1}{q} + \frac{1}{q_r}\right) \cdot \left(1 + \frac{\delta_{EW}}{\delta_{Hfs}}\right) \cdot T_{rec}. \quad (5.2)$$

Here q_r denotes the branching ratio of the $F' = 4 \rightarrow F = 3$ -transition, and $T_{rec} = \hbar^2 k^2 / mk_B$ is the recoil temperature for the cesium atom with the mass m . The theoretical limit for the temperature is about $2 \mu\text{K}$ for $q_r = 0.34$ and a detuning of the evanescent wave of $2\pi \cdot 2 \text{ GHz}$, about ten times higher than the recoil temperature that is typical for Sisyphus-cooling methods. The Sisyphus-cooling process is described in [Man99, Ham02a] in more detail.

During the transfer of the atoms in the GOST the potential energy is deposited into the sample. In this stage of the GOST Sisyphus-cooling is very important, because it has to remove this energy as fast as possible. In the initial storage phase the number of atoms declines relatively fast. One reason is that the atoms transfer their vertical energy into the horizontal motion and thus they can penetrate through the hollow beam. Since only the hottest particles can overcome the potential barrier, this process can be considered as plain evaporation which in addition to the loss leads to decreasing temperature. Another reason for the relatively fast decay is inelastic collisions mediated by the blue-detuned light field of the evanescent wave and the hollow beam.

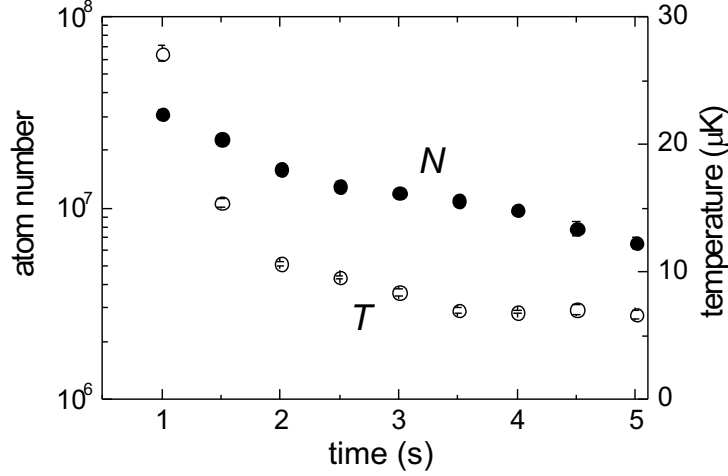


Figure 5.3: Time evolution of N and T in the near-resonant GOST. The atoms are cooled mainly by the Sisyphus process and plain evaporation through the hollow beam. The lifetime of the sample strongly depends on the detuning of the evanescent wave.

The ensemble temperature drops very rapidly from an initial value of about $100 \mu\text{K}$ to $10 \mu\text{K}$ after five seconds of Sisyphus-cooling, despite the relatively small 2 GHz detuning of the evanescent wave. The detuning has to be kept at this relatively small value to maintain the large cooling rate for the duration of the GOST stage, because otherwise the heating due to the hollow beam would lead to a higher temperature and consequently a lower density of the reservoir. Figure 5.3 shows the evolution of the atom number and temperature in the GOST. This data has been taken with a hollow beam detuning of 3 nm and evanescent wave detuning which starts at 2 GHz and is switched to 6 GHz two seconds after loading from the MOT. The diagram shows that the temperature due to the reduced heating process is about $3 \mu\text{K}$ below the value we can reach with the present experimental setup. But nevertheless, the GOST provides about 10^7 atoms with an density of about $3 \times 10^{11} \text{ cm}^{-3}$, a good starting condition for loading the dimple trap.

Ensemble Properties

In order to be able to improve the loading efficiency into the dimple trap, one has to know some properties of the reservoir. Its density determines the elastic collision rate, which plays a crucial role in the loading process.

To calculate the density distribution, one has to assume that the atoms are in thermal equilibrium, that the vertical potential can be considered as a hard wall and the horizontal one is a box potential. In this case, the density depends only on the height

above the prism and the temperature of the sample and can be derived from the formula

$$n(\vec{r}) = n_0 \exp\left(\frac{mgz}{k_B T}\right), \quad (5.3)$$

where $n_0 = Nm g / \pi k_B T r_{HB}^2$ is the peak density, r_{HB} is the radius of the hollow beam, N is the number of atoms, and T represents the ensemble temperature.

The average density of the sample for the GOST potential can be written as

$$\langle n \rangle = \frac{n_0}{2} \quad (5.4)$$

The phase-space density for unpolarized atoms in the GOST can be calculated from the peak-density n_0 and the thermal de-Broglie wavelength $\lambda_{dB} = h / \sqrt{2\pi m k_B T}$ as

$$D = \frac{1}{7} n_0 \lambda_{dB}^3 = \frac{1}{7} \frac{g \hbar^3 (2\pi)^{3/2}}{\pi r_{HB}^2 \sqrt{m}} \cdot \frac{N}{(k_B T)^{5/2}}. \quad (5.5)$$

The factor of 1/7 takes into account that the atoms are located in all seven magnetic substates of the Cs-ground state. When polarizing the atoms this factor disappears.

5.2 Dimple trap

The GOST serves as a atom reservoir for the next trap. The main part of the experiment takes place in the surface micro trap, the *dimple trap*. The dimple trap is where the evaporative cooling takes place and where the quantum degeneracy and finally the two-dimensional regime are achieved.

The dimple trap is a combination of a far-detuned evanescent wave and a tight focus of a 1064 nm-laser beam. The figure 5.4 shows the scheme of the dimple trap. The horizontal potential is now provided by the attractive gaussian potential of the 1064 nm beam. A combination of the hollow beam potential and the the dimple laser potential is shown in figure 5.5. Since the density in the dimple trap is much higher than the one in the GOST, the 2 GHz-evanescent wave has been replaced by an other one with detunings between 5-15 nm in order to suppress light induced collisions, discussed in section 3.4.1. The vertical potential depth given by the 13.2 nm detuned evanescent wave is $50 \mu\text{K}$, while horizontally the atoms see a $45 \mu\text{K}$ deep potential well for a 5 W-beam with a waist of $120 \mu\text{m}$.

5.2.1 The Dimple Trick and Loading the Dimple Trap

Measurements in [Ryc00] show that for several reasons it is not possible to reach quantum degeneracy in the GOST. The combination of box and wedge potentials used in the GOST leads to weak compression of the atoms during the evaporative cooling. However

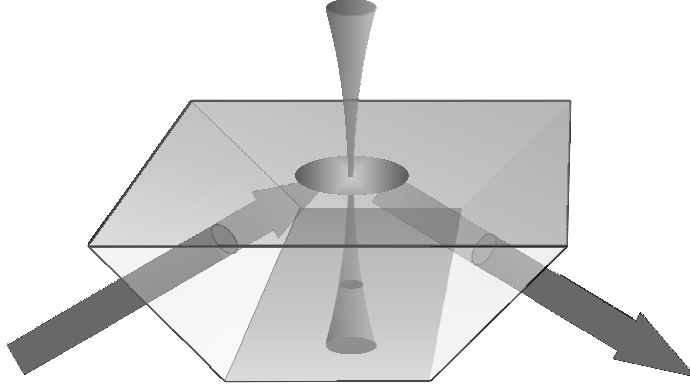


Figure 5.4: *Schematic overview of the dimple trap, where the dimple laser controls the horizontal confinement and a far blue-detuned evanescent wave confines the atoms vertically.*

a combination of the wedge potential and a gaussian potential leads to much favorable scaling between the phase-space density and the temperature.

An adiabatic modification of the shape of a potential can lead to a local increase in the density and phase-space density of the trapped atomic gas. Changing the strength of the potential adiabatically, without changing the shape, doesn't lead to an increase of the density, because the compression is compensated for an increase in the temperature. A non-adiabatic change will even decrease the phase-space density. In [Pin97] such a local increase of the phase-space density was demonstrated, and the same effect with cesium atoms was observed in previous experiments [Ham02b] in the GOST. This effect was used in [SK98] to reversibly form a sodium BEC by changing the peak phase-space density by a factor of more than 50.

It is important to note that the change is small compared to the whole potential. This means in our case, that the reservoir of the atoms is large compared to the size and the depth of the dimple trap. If the dimple trap potential is adiabatically transformed into the combined potential by slowly ramping up the intensity, the atoms trapped in the small dimple will have the same temperature as the reservoir temperature. The thermal contact between the reservoir and the small sample trapped in the dimple is caused by elastic collisions. In the dimple the density satisfies the relation $n(r) \propto \exp(U/k_B T)$, and thus the phase-space density is locally grown. Since the density has been increased, but the temperature stayed nearly constant, the phase-space density has been also enlarged. The constant temperature can be explained by the fact that the excess energy introduced during the process was absorbed by the large reservoir. Besides the condition that the

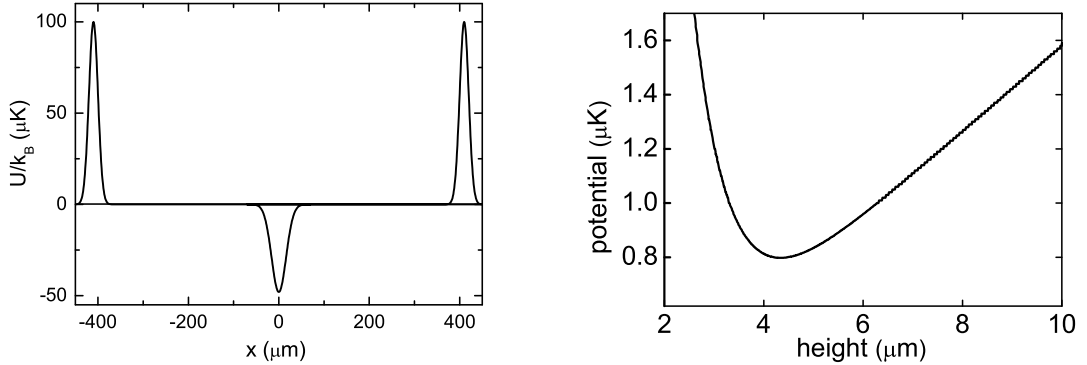


Figure 5.5: *During the loading of the dimple trap, the horizontal potential is a combination of the hollow beam and dimple laser potentials. The vertical potential consists of the repulsive evanescent wave potential and the gravitational potential, leading to a wedge potential as shown in the right picture.*

reservoir has to be much larger than the dimple, it is also important, that the dimple is not deep enough to load all reservoir atoms. This condition is also fulfilled in our case. A theoretical treatment of the dimple loading mechanism is given in [Pin97].

Figure 5.5 shows how the dimple trick is implemented in our experiment. First, the reservoir is prepared by the GOST, then the dimple laser is slowly ramped up and the atoms are loaded through thermalization into the dimple trap within about one second. Finally the reservoir is removed by switching off the hollow beam. Now, the dimple provides the only horizontal confinement, and further cooling of the dense sample can be started.

Since the trap potential is conservative, an atom entering the dimple trap from outside will leave the trap at some other point with unchanged kinetic energy. Of course, the atom gains kinetic energy by entering the potential, but it loses the same value by leaving the light field. There is no mechanism, which would force the atoms to stay in the trap, but there are two mechanisms leading to a reduction of the kinetic energy and thus trapping the atom in this conservative trap.

Considering the loading process, the location and energy of an atom are both important. For example, during the loading process when ramping up the dimple potential, energy can be transferred from outside into the system or vice versa. It depends on the position and kinetic energy of the atom, whether it loses enough energy to remain in the trap or receives energy from the changing potential. An atom which is inside the light field and has energy smaller than the potential depth of the trap, it can not climb up the potential hill and so will remain trapped. This case shows that the spatial overlap

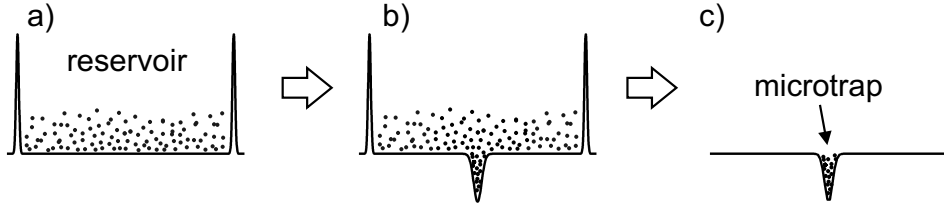


Figure 5.6: First, the atoms are precooled in the GOST (a), then the dimple potential is ramped up and the atoms are loaded by elastic collisions into the trap (b) and finally the reservoir is removed by switching off the GOST-laser beams and the atoms are trapped vertically by the dimple (c).

between the reservoir and the dimple trap and the temperature of the reservoir atoms are both important parameters in considering the loading process. Optimizing the loading process by adjusting these both parameters is called *phase-space matching*. The calculation in [Ham02b] shows that the transfer efficiency for a small ($40\ \mu\text{m}$) dimple is in the range of few percent which can be explained due to the bad spatial overlap between the reservoir and dimple trap. Increasing the volume of the dimple trap increases the number of trapped atoms on one hand, but on the other hand it reduces the gain in density and peak phase-space density.

There is another process, which increases the transfer efficiency. Since the GOST provides a large and dense sample of atoms, elastic collisions occur frequently between the atoms within the dimple trap. Such elastic collisions can change the kinetic energy of both collision partners. If one of the colliding atoms doesn't possess enough energy to leave the potential well it remains trapped, while the other atom carries its missing energy away. On this account it takes for about one second to load a large dimple trap; then an equilibrium of the loading processes and opposite processes, where trapped atoms are kicked out from the trap, is reached and the atom number in the trap stabilizes. References [Ham02b] and [Wen00] discuss this loading process in more detail.

Figure 5.7 shows the typical loading curve, where $N(\bullet)$ the number of atoms trapped in the dimple and $N(\circ)$ the number of reservoir atoms is depicted. Immediately after the sudden switch on of the dimple laser, which is focussed to $32\ \mu\text{m}$, 4×10^4 atoms are trapped in the $4\ \mu\text{K}$ potential. Elastic collisions fill the in this case relatively small dimple trap on the time scale of few 100 ms, and the maximum is reached after 500 ms, when the equilibrium between the loading rate and the loss rate is reached. Loading in a larger dimple trap happens on similar time scale and shows the same behavior. Transfer efficiencies up to 40% have been observed for a dimple trap with large volume. The loading mechanism for both cases is described in [Ham02b] in more detail.

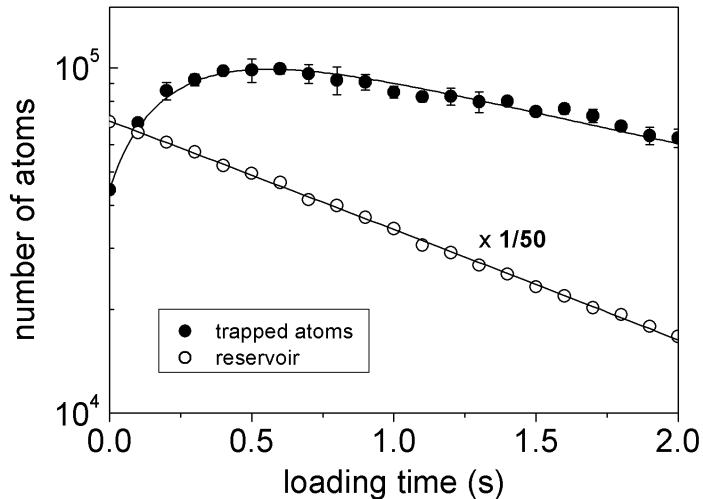


Figure 5.7: Typical loading curve for a dimple trap. After about half second the dimple trap is loaded by thermalization. The solid lines are fits obtained from the model described in [Ham02a].

5.2.2 Ensemble Properties

After the dimple trap has been loaded, evaporative cooling is initialized. In order to be able to optimize the evaporation efficiency, one has to know the density and the phase-space to be maximized. Since these values can't be measured directly, they have to be calculated from quantities obtained by direct measurements. As described in following paragraphs, we are able to measure the number of atoms N , the temperature T and the trap frequency ω .

The trap frequency, measured by the method described in section 5.3.5, specifies the behavior of the atoms in the trap. There is not only one frequency, but due to the anharmonicity of the potential we get a wide spectrum of trap frequencies. The approximation of the potential by a harmonic potential is not valid for all energies but only for the case when the ensemble temperature is much smaller than the potential depth. Atoms at higher energies in principle oscillate at smaller frequencies than atoms at low energies. For all the following formulas a harmonic potential in the horizontal plane and a wedge-potential in the vertical direction is assumed. Since the dimple potential is symmetric in the x-y-plane, one can introduce the radial coordinate $r \equiv \sqrt{x^2 + y^2}$ and write for the density of the atomic sample

$$n(\vec{r}) = n_0 \cdot \exp\left(-\frac{r^2}{r_0^2}\right) \cdot \exp\left(-\frac{z}{z_0}\right), \quad (5.6)$$

where $r_0 \equiv \sqrt{2k_B T / (m\omega_r^2)}$ is the radius, $z_0 \equiv k_B T / mg$ describes the height at which the density has decreased to $1/e$ of its initial value and ω_r denotes the radial trap frequency in the dimple trap. Starting from the peak number density n_0 with the effective volume $V_0 \equiv \pi r_0^2 z_0$, one can derive the mean density $\langle n \rangle = 1/N \cdot \int n^2(\vec{r}) dV$ and the mean quadratic density $\langle n^2 \rangle = 1/N \cdot \int n^3(\vec{r}) dV$ as:

$$n_0 = \frac{N}{V_0} = \frac{m^2}{2\pi k_B^2} \cdot \frac{N\omega_r^2}{T^2} \quad (5.7)$$

$$\langle n \rangle = \frac{n_0}{4} \quad (5.8)$$

$$\langle n^2 \rangle = \frac{n_0^2}{9} \quad (5.9)$$

Now, having the peak number density, we can calculate the phase-space density for an unpolarized sample from the expression $D = 1/7 \cdot n_0 \lambda_{dB}^3$. Polarizing the atoms leads to an increase of the phase-space density of a factor 7 due to the fact that all atoms populate only one magnetic sub-state, so it can be written as

$$D = \sqrt{2\pi m} \cdot \frac{g\hbar^3 N\omega_r^2}{(k_B T)^{7/2}}. \quad (5.10)$$

The formulas 5.7 and 5.10 show that evaporative cooling is more favorable in the dimple trap than in the GOST, where the peak- and average densities scale with atomic number and temperature as $n_0 \propto N/T$ and the phase-space density $D \propto N/T^{5/2}$. The more favorable scaling of the temperature in the formula for the peak density in the dimple trap leads to stronger compression of the sample for decreasing temperature. During the evaporative cooling the decreasing temperature is a result of two independent effects. In contrast to evaporative cooling, where the temperature is reduced and the phase-space density increased at the cost of trapped atoms, cooling by adiabatic change of the potential depth without change of the potential shape, reduces the temperature and the density in a such way that the phase-space density stays constant.

5.2.3 Storage

Particular with regard to the evaporative cooling, the lifetime of the atoms in the dimple trap turned out to be very important. Many effects, like two- or three-body collisions, plain evaporation or defects in the evanescent light field can reduce the life time radically. In [Ham02b] the storage in the dimple trap has been studied in detail. In this paragraph only a short survey of the effects affecting the lifetime in the dimple trap will be given.

Figure 5.9 shows a typical lifetime measurement of atom in the dimple trap. This data has been measured in a dimple trap with an evanescent wave detuning of 1.5 nm.

To ensure that the lifetime is not governed by plain evaporation, we wait until the equilibrium at $T = 5.1 \mu\text{K}$ is reached. Since the temperature can be assumed constant, the peak density after 1.2s of $3.2 \times 10^{13} \text{ cm}^{-3}$ is in this case dependent on the atom number only, which makes the evaluation of the decay easier. Possible candidates for the loss are light-assisted collisions, three-body collisions and loss through leaks in the evanescent wave potential. All these processes can be described by the formula 3.30. Using this theory and the data fit from figure 5.9 it was not possible to entirely separate the loss contributions from two-body and three-body processes. The calculations result in the coefficient $\beta = 3.5 \times 10^{-14} \text{ cm}^{-3}/\text{s}$ and an upper bound for L_3 of $10^{-27} \text{ cm}^6/\text{s}$. As the decay is obviously non-exponential, the losses seem to be caused by a collisional

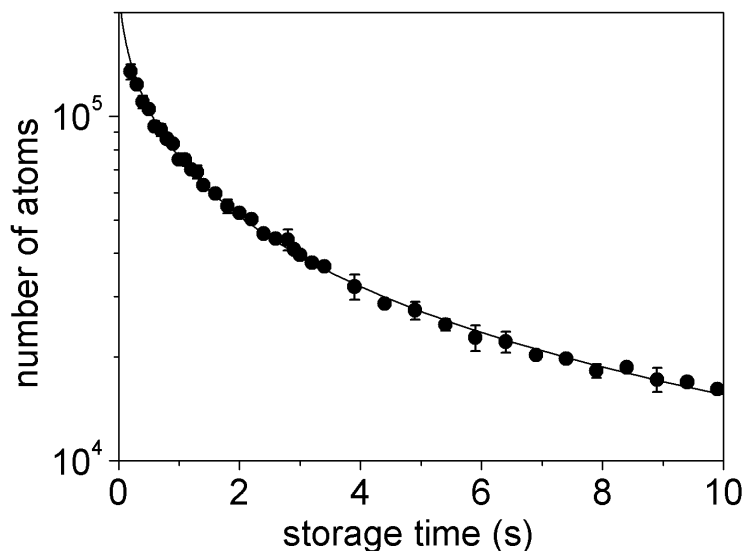


Figure 5.8: *Typical decay of the atoms in the dimple trap. The lifetime is limited by processes described in the text.*

mechanism. Since this data have taken with a unpolarized sample, a collision process that changes the magnetic substate and releases the Zeeman energy, will also play a role in the loss process. Measurement shows that the lifetime can be increased when polarizing the atoms. We observe that the life time significantly depends on the applied magnetic offset-field: the larger the magnetic field, the shorter the life time. This can be explained by the fact that with increasing magnetic field the internal energy of the atom also increases. But unfortunately, our polarization method doesn't polarize the sample completely, there are still some atoms in higher magnetic substates leading to reduced life time. Only after polarizing the atoms completely can we distinguish between the different loss processes.

5.3 Measurement Procedures

5.3.1 Experimental Control

In our experiment there are nine lasers, about ten different magnetic coils, one camera and many other parts, which have to be coordinated and synchronized with an accuracy of microseconds. There are processes which are done in less than few milliseconds and others which take several seconds. This shows that the control of the experiment has to be very flexible to obtain exact and stable data.

Every dynamical part in the experiment is either controlled by a TTL-pulse or an analog signal which controls intensity ramps or magnetic fields. The central element of the experimental control is a timing board (Adwin-4LD), which generates the control signals after the desired control sequence has been entered through the LabView interface on a PC. Our Adwin version includes 23 TTL-compatible digital channels and 8 analog outputs with $\pm 10 V$ range which control in particular the the intensity ramp of the dimple laser, the Feshbach magnetic field and the detuning of the MOT-laser. The accuracy is better than $1 \mu s$ and the minimum step between consecutive switching process is $10 \mu s$. The LabView graphical user interface enables the experimentalists to enter the times, when each channel has to be switched off or set to a certain value. The program allows these variables to be varied systematically from one experimental cycle to the next.

To change the size of the dimple trap, the focusing lens is mounted at a linear positioning stage, which is driven by a micro motor. To trigger the stage a TTL-pulse is send to the motor controller, which can be programmed by the software "NetMove for Mercury". The programming of the travel velocity, the distance to go and the acceleration is straightforward. In standard operation the controller is programmed in such a way that a single TTL-pulse triggers a closed loop of different commands. The stage moves during the evaporation with a velocity of 0.2 mm/s over a distance of 11 mm , changing the dimple size from $130 \mu\text{m}$ to $64 \mu\text{m}$, it then waits at the final position for 5 s before moving back to the origin wait for the next trigger-pulse. The original position can be reproduced with a precision in the range of a micrometer, which ensures a stable and reproduceable measurement cycle.

5.3.2 Measurement Cycle

The measurement cycle consists of three stages and is typically 15 s long. First the atoms are collected and pre-cooled in the MOT, then transferred in the GOST, which prepares the atoms for loading into the dimple trap, where then evaporative cooling takes place. These three stages span a temperature gap of initially several hundred Kelvin and the final 15 nK reached at the end of the evaporative cooling.

In the MOT about 5×10^8 atoms are loaded from the atomic beam within 5 s . Before

the transfer into the GOST the atoms are further cooled down by polarization gradient cooling. This cooling stage reduces the temperature down to few microkelvin and is realized by increasing the MOT-laser detuning from initially -8 MHz to -60 MHz within 50 ms directly before the laser is switched off. At the same time an offset magnetic field shifts the magnetic field zero of the compressed MOT about 0.5 mm above the prism surface. Additional horizontal offset fields position the cloud in the center of the hollow beam. Then the MOT laser beams and the quadrupole field are switched off and the atoms drop onto the evanescent wave. In the first second of the Sisyphus-cooling and plain evaporation through the evanescent wave and hollow beam, the atoms are cooled down from as much as $100 \mu\text{K}$ to few tens of microkelvin. Because of the conversion of the potential energy into kinetic energy ($160 \mu\text{K}/\text{mm}$), the temperature of the sample in the initial GOST is much higher than the temperatures reached by the polarization gradient cooling in the MOT. The Sisyphus-cooling in the GOST prepares up to 10^7 atoms at $\sim 10 \mu\text{K}$ in 5 s. The dimple laser is ramped up within a half second 3.5 s after the atoms are transferred into the GOST. After waiting for 1 s until the dimple is filled through elastic collisions, the hollow beam and the near resonant evanescent wave are switched off. The far detuned evanescent wave, used for the vertical confinement in the dimple trap, is already switched on since starting the cycle to support the evanescent wave of the GOST and to further reduce thermal effects in the AOM. Simultaneously with removing the reservoir at $t = 5 \text{ s}$, the compression ramp is initialized, the lens focussing the dimple beam is moved by a linear stage for about 5 s thereby changing the size of the dimple trap from $130 \mu\text{m}$ to $64 \mu\text{m}$. The forced evaporative cooling is started at $t = 5.1 \text{ s}$ by ramping down the intensity of the dimple laser from its initial value of 5 W to a few mW within 5.5 s.

To measure the number of atoms remaining in the dimple trap after the evaporation, the MOT-beams and the quadrupole magnetic field are switched on to drive the atoms into the MOT. After a CCD-camera takes a picture of the fluorescence of the recaptured atoms, the atomic beam shutter is opened again and a new experiment cycle begins.

5.3.3 Atom Number Measurement

In the most BEC-experiments [Ket99] the number of atoms and their density is measured by absorption imaging using a resonant laser beam which generate a shadow to a CCD-camera. Due to the geometry of the trap and the current setup it is not possible to use this technique as a diagnostic tool. The standard practice for measuring the desired quantity is to recapture the atoms into the MOT and determine their number as a function of various parameters.

The fluorescence of the atomic cloud in a -8 MHz detuned MOT is measured by a CCD-camera (Princeton Instruments RTE/CCD-768-K/1) with a 30 ms exposure time. In order to measure low numbers of atoms, we increase the exposure time up to 150 ms, in this way we are able to detect few hundred atoms. But background light and dark

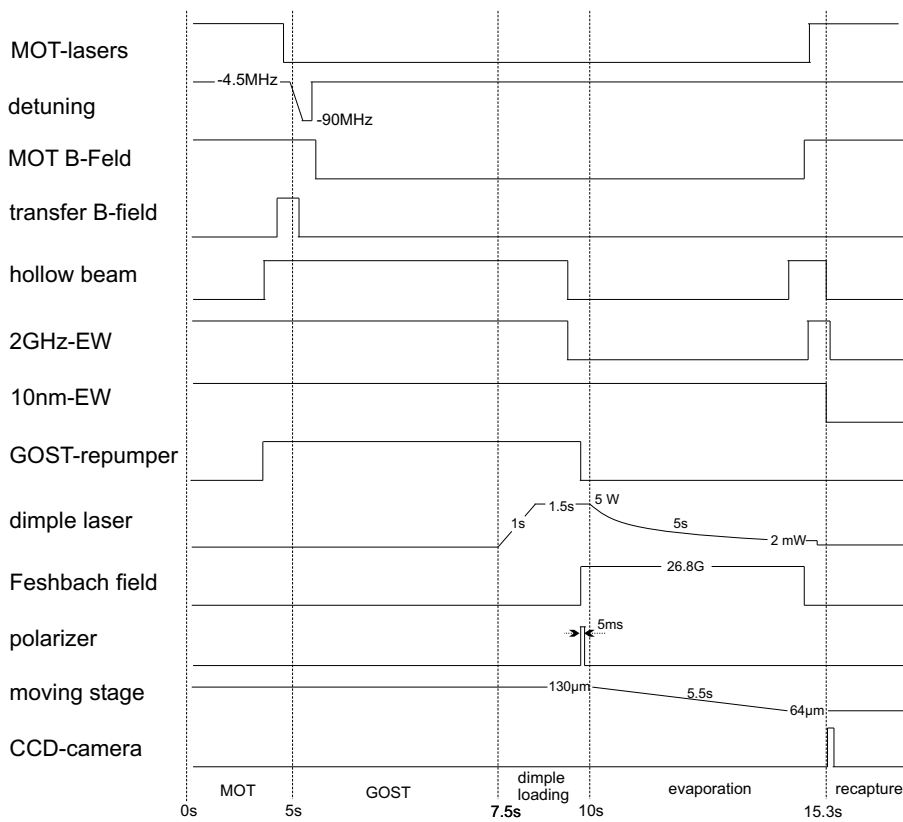


Figure 5.9: A schematic overview of the whole timing sequence. The experimental cycle consists of five parts. It takes typically 5 s to load the MOT. The cooling in the GOST follows, loading the atoms in the dimple trap. After the dimple laser power is ramped down, the moving stage stops and the evaporative cooling is finished, the atoms are recaptured into the MOT and the next cycle may follow.

currents of the CCD-chip limits the number of detectable atoms. The camera has been calibrated by using an absolute number determination by absorption imaging with an absolute error of fifty percent. Further details to absorption imaging can be found in [Ham02b, Mos99].

5.3.4 Temperature Measurement

In the GOST

The temperature measurement plays an important role in the consideration of the results, because besides the atom number it is the second quantity we can measure and then use for calculation of the density and phase-space density. Due to the trap geometry we have to distinguish between vertical and horizontal temperature, even if they are

in most cases equal. The temperature, both in the GOST and the dimple trap, is mea-

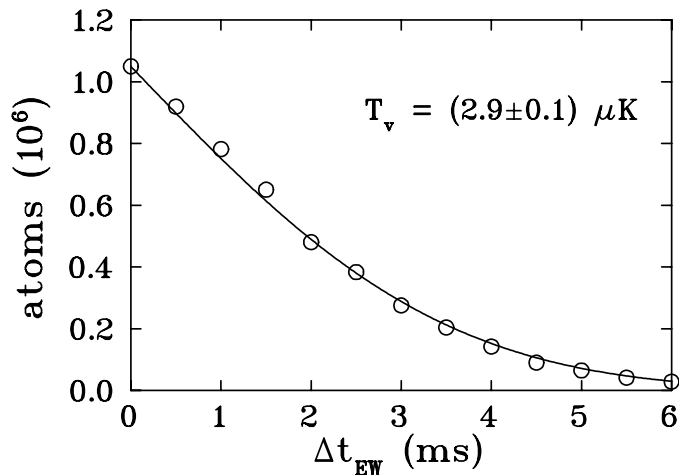


Figure 5.10: *Temperature measurement for relatively high temperature as it occurs in the GOST or in the first stage of dimple trapping. The figure plots the number of recaptured atoms after the evanescent wave was turned off for the time Δt_{ew} .*

sured by the release-and-recapture method, by which for a short time interval one of the confining potentials is removed and the sample can ballistically expand. After restoring the confinement, only a certain fraction of the atoms can be recaptured. Atoms, which are not trapped get lost, either by hitting the prism or escaping horizontally. The size of the remaining fraction is dependent on the length of the time interval and the temperature of the sample. To obtain the temperature, one must measure the remained fraction for different time intervals. The temperature can be derived as a single fit parameter from a theoretical model described for higher temperatures in [Man99].

Most temperatures given in this work are vertical temperatures measured by release-and-recapture at the evanescent wave. The horizontal temperature can be measured by switching off the laser which is responsible for the horizontal confinement, either the hollow beam or the dimple laser. If the ensemble is thermalized, the vertical and the horizontal temperatures are the same. The reason, why we use the vertical temperature to characterize the properties of the atoms is the fact, that the horizontal motion of the atom is given not only through its horizontal velocity. At lower temperatures, the vertical oscillation period is much smaller than the time it takes an atom to move vertically out of the region where it can be recaptured by the hollow beam or the dimple laser. Therefore it will be reflected many times from the evanescent wave. The horizontal motion of an atom can be described as a diffusive rather than a ballistic motion. In section 6 we will see that also impurities in the evanescent wave potential leads to modified expansion of the sample.

At low Temperatures

In principle, there is no difference in the temperature measurement in the GOST and in the dimple. But there is a difference in the temperatures reached in these two traps. At temperatures well below about one microkelvin, such as reached in the dimple, the evanescent wave can no longer be approximated as a hard wall. This can

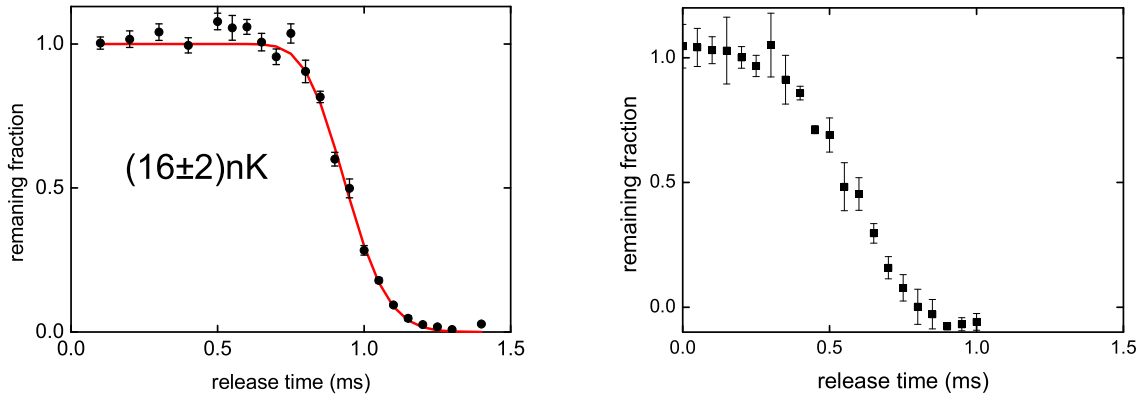


Figure 5.11: *Measurement of the release energy after evaporative cooling in the dimple trap for two different decay lengths of the evanescent wave. While the decay length in the left measurement was $1.7 \mu\text{m}$, for the right measurement we calculated a three times smaller decay length. In the left graph the fit function corresponding to a release energy of $k_B/2 \cdot 16 \text{ nK}$ is shown.*

be explained by the fact that, due to the reduced temperature the vertical extension of the sample $k_B T/mg$ is comparable or even smaller than the decay length Λ of the evanescent wave. Now, the atoms “feel” the detailed shape of the evanescent wave. To calculate the temperature, one can use the same theory, but the idealized potential of the evanescent wave has to be replaced by the realistic one. The new theoretical model has to take into account that only the atoms falling below the maximum of the vertical potential, at about $0.1 \mu\text{m}$, can’t be trapped again. Finally a numerical fit procedure yields the result for the temperature.

As depicted in figure 5.11, a characteristic for these low temperatures is a plateau at short release times. This plateau is dependent on the decay length of the evanescent wave, because due to the distance between the sample and the recapture boundary the atoms need a certain time to cover this distance in free fall. The evidence of this fact is shown in the figure 5.11, where the temperatures have been measured for two different angles of incidence of the evanescent wave. The smaller the decay length the shorter is the plateau, because the atoms are sitting closer to the surface, when the decay length

is smaller. In the case of the larger decay length the atoms need approximately $600 \mu\text{s}$ to reach the recapture boundary during their fall.

Quantum Effects

In the previous paragraphs we have seen that the temperature measurement curves are completely different for high and low temperatures. The lower the temperature is the steeper is the slope, from which the temperature information is mainly extracted. In the classical case, we would expect a step function at zero temperature, because all atoms would reach the potential maximum at the same time. But at very low temperatures the behavior of the atoms is dominated by quantum mechanics.

When the thermal energy of the ensemble becomes comparable to the vibrational energy quantum $k_B T \approx \hbar \omega_0$ the behavior must be treated quantum mechanically, because a considerable part of the atomic motion consists of the zero-point energy. As we will see in section 6.2, we have reached the case where the kinetic energy of the sample is mainly the ground state energy $\hbar \omega_0/2$. In this case the atomic motion doesn't follow ballistic expansion, but quantum mechanical rules have to be taken into account. At this point, we can't really talk about temperature measurement, but rather measurement of the kinetic or release energy of the ensemble.

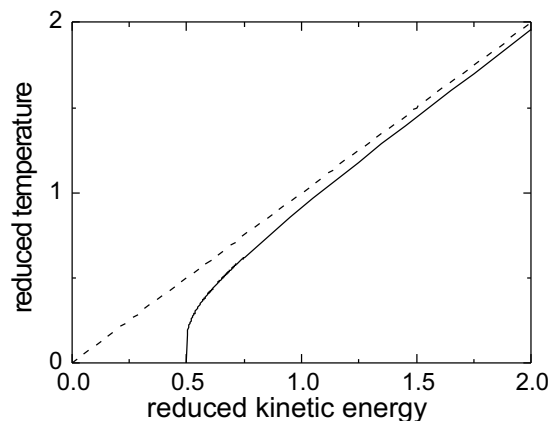


Figure 5.12: *The correction function translates for low temperatures the experimentally measured mean kinetic energy into a thermodynamic temperature. The dashed line represents the classical expectation.*

To calculate the correction of the measured "temperature" one has to derive a thermodynamical temperature T from a known mean kinetic energy \bar{E} of the quantum mechanical system. Since we are considering behavior at very low energies, where the anharmonicity of the potential can be neglected, we can assume a purely harmonic po-

tential with the oscillation frequency ω_0 . An atom can be found in a state corresponding to the energy $E_n = \hbar\omega_0(n + 1/2)$ with the probability

$$p(n) = \frac{1}{\Omega} \cdot \exp\left(\frac{\hbar\omega_0}{k_B T}(n + 1/2)\right), \quad (5.11)$$

where $\Omega \equiv \sum_{n=0}^{\infty} p(n) = \frac{1}{2} \cdot \sinh^{-1}\left(\frac{\hbar\omega_0}{2k_B T}\right)$ is the partition function.

The temperature T can be calculated from the formula for the mean energy

$$\bar{E} = -\frac{\partial}{\partial\beta}(\ln \Omega), \quad (5.12)$$

with the inverse temperature $\beta \equiv 1/k_B T$. Solving for T results in the correction formula for the true thermodynamic temperature:

$$T = \frac{\hbar\omega_0}{2k_B} \cdot \operatorname{arccoth}^{-1}\left(\frac{2\bar{E}}{\hbar\omega_0}\right). \quad (5.13)$$

Figure 5.12 shows the correction function, that translates the experimentally measured mean kinetic energy into a thermodynamic temperature. The reduced kinetic energy stands for the ratio between \bar{E} and the vibrational energy quantum $\hbar\omega_0$, while the reduced temperature relates the thermal energy to the vibrational energy and can be described by $k_B T/\hbar\omega_0$.

5.3.5 Trap Frequencies

Besides the temperature and the atom number the trap frequency is the third measurable property we need to characterize the ensemble. The method was first realized in [Fri98a] and was previously used in this experiment to measure the trap frequencies in the double-evanescent wave [Ham02a]. It is based on parametric heating of the trapped particles by a modulation of the trapping potential. This method can be used for both vertical and horizontal frequency measurement, by modulation the amplitude of the evanescent wave or the dimple laser beam respectively.

Figure 5.13 shows a typical measurement curve. After the atoms are transferred into the dimple trap and temperature equilibrium is reached by plain evaporation, the power of the evanescent wave is modulated with a modulation depth of 10%. After three second modulation we measure the number of atoms as a function of the modulation frequency. If the modulation frequency equals the vertical frequency, we observe a clear minimum of the remaining atom fraction due to efficient parametric heating at this frequency. To measure the horizontal trap frequency, one has to modulate the power of the dimple laser with typically the same modulation depth. If the horizontal trap frequency corresponds to the modulation frequency, the atoms are heated out of the trap in the same way.

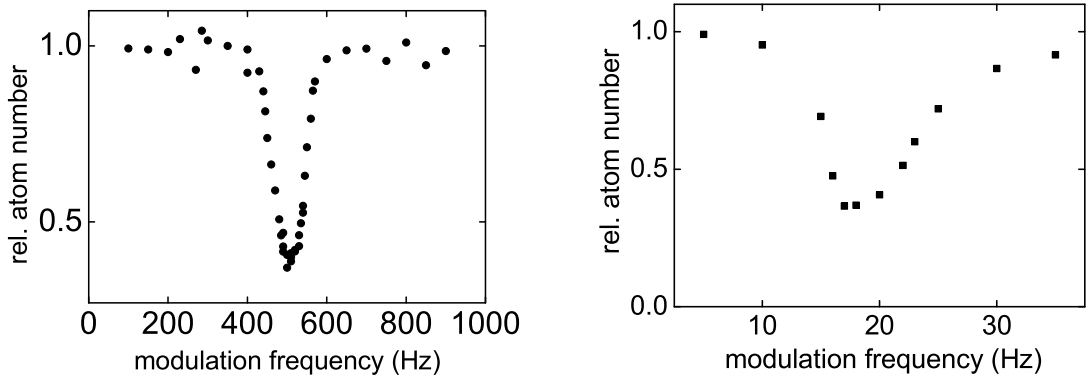


Figure 5.13: *Vertical and horizontal frequency measurement. The measured relative atom number exhibits a clear minimum when the modulation frequency matches the trap frequency. The horizontal frequency was measured after the evaporative cooling at a final power of about 5 mW and exhibits a minimum at much smaller frequency.*

Since the horizontal trap frequency is very important for the calculation of the density and the phase-space density, we use another method to check the trap depth modulation measurement. We change the horizontal position of the dimple trap by changing the modulation frequency of the AOM. Changing the modulation frequency of the AOM leads to a different diffraction angle of the first order of the incident beam and thus to a different position at the prism surface. The modulation depth of about 5% of the 200 MHz leads to spatial modulation of the dimple position of few micrometers. Measuring the number of atoms remaining in the trap reveals the same behavior as observed with the first method. The results confirm the trap depth modulation measurement.

The observed shape of the resonance in the remaining atoms depends on the temperature of the sample and in some cases it is not symmetric, which is not expected. The origin of this unsymmetry must be related to the anharmonicity of the potential which implies that the vibrational frequency changes with the atomic energy. In the case of the measurement of the horizontal trap frequency, effects like slightly elliptical shape of the dimple spot may lead to a broadening of the measured resonances. The lateral spread of the atoms in the dimple trap may also increase the width of the minima in the vertical measurement because in the outer regions of the evanescent wave the potential is less deep and thus the trap frequency is smaller than the trap frequency in the center of the evanescent wave. In addition, we assume that the peak in the resonance of the atomic loss is slightly lower than the actual frequency [RJ01].

In the vertical direction, we measure a trap frequency of 500 Hz for a 700 mW-evanescent 0.2° from the critical angle. Changing the angle of incidence to 2° from

the critical angle leads to a vertical trap frequency of 850 Hz due to the reduced decay length of the evanescent wave. Horizontally, at the end of the evaporation ramp and at a power of 1.6 mW, we measure a frequency of 10 Hz, 50-times smaller than in the vertical direction.

5.3.6 Polarized Atoms

The earlier experiments in the GOST or in the dimple trap [Man99, Ham02a] were performed with unpolarized atoms, where the atoms populate the seven magnetic substates of the ground state $F = 3$. This led to stronger losses due to inelastic collisions and thus reduced the lifetime in the trap, particularly at higher densities.

Polarizing the atoms has many advantages. As mentioned in section 2.3.4, polarizing the atoms into the $m_F = 3$ -substate makes it possible to tune the scattering length and thus alter the entire scattering behavior of the sample. Furthermore the use of the Feshbach resonance enables us to change the interaction between the particles from repulsive to attractive, leading to a collapse of the condensate. We use this property to prove the presence of the condensate (see next chapter). Since the atoms are not spread out over the seven substates, but populate only one state, polarizing the atoms leads to an increase of the phase-space density by a factor of seven. A further consequence of polarizing the ensemble is a doubling of the elastic collision rate due to the symmetrization factor of identical bosons.

In contrast to magnetic traps where the atoms have to be polarized to be trapped, an optical dipole trap can store the atoms in all magnetic substates. This leads to the disadvantage that the atoms in higher spin-states do not leave the trap immediately but may be involved in inelastic collisions and get lost. In our experiment immediately after the atoms have been loaded into the dimple trap they are polarized by optical pumping. In order to define an axis of quantization a magnetic field of about few Gauss is applied in vertical direction and then a 5 ms pulse of σ^+ -polarized laser light, resonant with the $F = 3 \rightarrow F' = 2$ -transition, pumps the atoms into the right state. As depicted in figure 5.14, the polarizer laser is sent into the chamber parallel to the magnetic field. Due to the selection rule $\Delta m_F = 0, +1$ the atoms are pumped into the "dark state" $|F = 3, m_F = 3\rangle$ where they can only be "seen" by a σ^- -polarized light. In order to reduce this depolarizing component in the polarizer laser light the beam passes only a polarizing beam splitter, producing linearly polarized light, and a quarter wave plate generating the circularly polarized light before entering the chamber. Nevertheless, a residual component of the "wrong" light can't be avoided. Also when the laser light is not perfectly parallel to the applied magnetic field the atoms see a small π -components even if the incoming laser beam would be perfectly σ^+ -polarized. The atom then sees elliptically polarized laser light. The ellipticity may be changed by tilting the axis of quantization which can be achieved by applying additional magnetic fields in the horizontal directions. In order to minimize the ellipticity one has to optimize the size

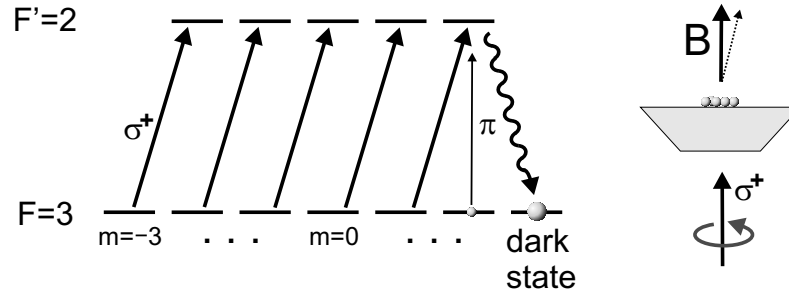


Figure 5.14: Schematic overview of the polarizing process. The atoms are pumped by σ^+ -light into the dark-state $m_F = 3$, where the atoms can't be "seen" by the polarizer light. As depicted in the schematic figure the polarizer laser is sent parallel to the magnetic field defining the axis of quantization.

of the applied horizontal magnetic field.

We measure the degree of polarization by using levitation (see next section) and vary iteratively the x- and y-component of the magnetic field until we have reached optimal polarization. Since it is not possible to make the elliptically polarized light to perfectly circularly polarized one there remains a small π -component, which in our case doesn't lead to any depolarization. Theoretically the σ^- -component can be completely compensated. For a perfectly σ^+ -polarized laser beam there would not be any depolarization effect even for large laser power, because the atoms are in a dark state and the power would not be adjusted exactly to the right value. But when there is a residual "wrong" component in the polarizer beam the atoms may be pumped via $|F' = 3, m_F = 2\rangle$ back into higher spin-states; therefore it is important to optimize the intensity of the polarizer laser beam. On the one hand in this case a too strong polarizer beam would guarantee that the atoms reach the dark state, but on the other hand the strong "wrong" polarization components would lead to depolarization and to heating-up of the sample. With a weak polarized laser beam we would suppress the depolarization components but there would not be enough σ^+ -light to pump the atoms in the dark state. In order to optimize the intensity of the laser beam we either vary the length of the polarizer pulse (typically between 2-15 ms) or change the power until we have maximized the number of polarized atoms.

The purity of the polarization and the strength of the polarizer determine only the degree of polarization and the number of scattered photons leading to heating-up of the sample, but they don't affect the depolarization in the dimple trap. Since in the optical dipole trap all magnetic substates can be trapped the atoms may depolarize without getting lost. Depolarization means that the atoms are somehow transferred from the $m_F = 3$ -state into higher spin-states, and the fraction of the atom number in these both

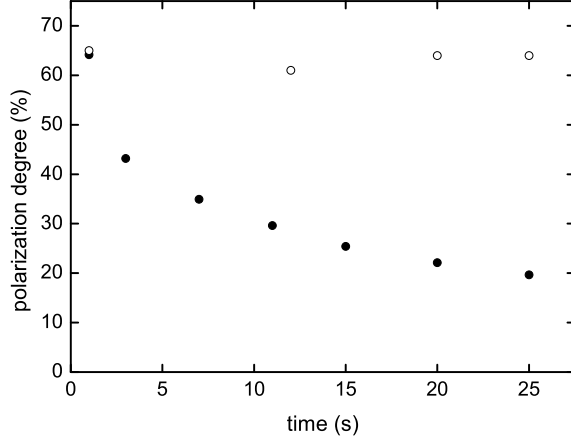


Figure 5.15: Course of the polarization degree in the dimple trap with (●) and without (○) repumper laser. The absolute number of atoms in the $m_F = 3$ -state is almost the same for both cases. In the first case the atoms are pumped back into the $F = 3$ state but not necessary in the lowest spin state. When the repumper is not present the atoms pumped in the upper hyperfine state get lost. For this measurement the evanescent wave was 1.7 nm detuned.

groups (in $m_F = 3$ and $m_F \neq 3$) of atoms decreases. The most probable process is photon scattering where the atoms are pumped in the higher sublevels after absorbing a resonant photon. This effect has been investigated in the GOST and in the dimple trap. In the GOST, we observed very fast decay of the polarization degree at a timescale of less than one second. This decay was strongly dependent on the detuning of the evanescent wave. For a detuning of 4 GHz we have observed an exponential decay of the polarization with a lifetime of 0.7 s, increasing the detuning to 12 GHz led to doubling of the lifetime. The larger the detuning the less photons are scattered and thus the smaller is depolarization rate.

In the most cases the atom doesn't return to the original magnetic substate after it has been excited, but it returns either into the upper hyperfine state $F = 4$ or into $F = 3, m_F \neq 3$. Atoms in the $F = 4$ -state are pumped back in to the $F = 3$ by the GOST-repumper. Since the GOST-repumper is randomly polarized the atoms are pumped back into the $F = 3$ -state according the selection rule $\Delta m_F = 0, \pm 1$ and do not return always into the lowest spin-state. This pumping back into the higher spin-states can be suppressed by lowering the power of the repumper. In the dimple trap we observed almost no depolarization, when the GOST-repumper was not present. The repumper changed only the ratio between atom numbers in the $m_F = 3$ and the number of atoms in the other substates, but the absolute number in $m_F = 3$ didn't change at

all, because the absolute number of all atoms in the trap decreases when the GOST-repumper is not present, because the atoms in $F = 4$ decay. We have increased the detuning up to values of about 10 nm, without observing any change in the lower curve in figure 5.15, so there must be another process transferring the atoms into the upper hyperfine level. Deeper investigations could exclude the dimple laser as a source of resonant photons. Until now we couldn't explain this process.

In order to suppress depolarization due to EW-photon scattering we increased the detuning of the evanescent wave to values up to many nanometers. During the evaporative cooling in the red GOST the EW is operated at detunings of about 10 nm where we don't observe any detuning-dependence of the reduced depolarization since the photon scattering is almost fully suppressed. We further switch off the GOST-repumper and set the scattering length to $400 a_0$, then we do not observe any depolarization, in contrast to previous measurements we observe an increase of the polarization degree during the evaporation. At the end of the evaporative cooling we observe a polarization of about 90%. The increased polarization can be explained by the fact that the higher the density of the sample the stronger are losses due to m_F -changing collisions and atoms in higher substates leave the trap, while only atoms without internal energy remain in the sample. Since the repumper is not present there seems not to be another depolarizing mechanism which would lead to increasing of the population in the higher spin-states.

5.4 Important Tools

5.4.1 Levitation

After the atoms have been polarized, it is important to know how many atoms are in the ground state $F = 3, m_F = 3$. It turned out experimentally that if less than 50% of all atoms are in the absolute ground state the evaporation doesn't work efficiently, because during the evaporation the applied magnetic field used for Feshbach tuning leads to strong losses due to inelastic collisions. Using the levitation technique, we can probe the degree of polarization and thus optimize the polarizing process by increasing the number of atoms in the ground state.

The levitation is based on a magnetic force induced by the magnetic quadrupole field and is thus dependent on the magnetic substate. The intention of this method is to compensate for gravity for atoms in the lowest spin-state substate by the levitation field. While the atoms in this state are vertically confined by the levitation field, atoms in the opposite spin-state, $m_F = -3$, experience a force parallel to gravity and thus they are pressed against the evanescent wave. Atoms populating other states experience only a weak force, the size and direction depends on the spin-state but is not strong enough to compensate the gravity. When the levitation field is present and the evanescent wave is switched off for a time longer than the time between two bounces all, atoms

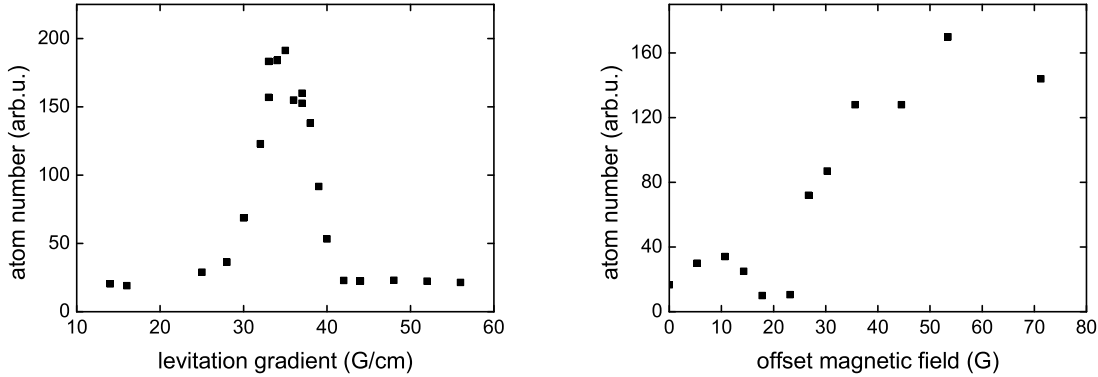


Figure 5.16: *Number of levitated atoms versus the gradient field (left picture). Changing the sign of the gradient by moving the position of the quadrupole field zero strongly affect the number of levitated atoms.*

in the “wrong” spin-state get lost, while atoms in the $F = 3, m_F = 3$ -state, hold by the levitation field, “survive” the missing vertical confinement and are observed in the recapture-MOT. The off-time of the evanescent wave has to be long enough to ensure that also the hottest atoms, hitting the evanescent wave less often, nevertheless hit the surface and get lost. For a vertical trap frequency in the range of one kilohertz a switch-off time of about 30 ms turned out to be long enough to lose even the hottest atoms (see also the subsection 5.3.4). Since the coils which generate the levitation field, are wound directly onto the main chamber and thus are not exactly symmetric, the magnetic field gradient has a component not only in the vertical direction, but also in the horizontal directions leading to a horizontal force. This makes it impossible to hold the atoms for longer than 100 ms by the levitation field, additionally, the lack of cooling of the levitation coils prevents longer operating times, because the operating current of 80 A heats up the coils to temperatures of about 70°C within few seconds.

As we have seen in section 3.3 the magnetic force depends not only on the strength and direction of the magnetic field gradient, but also on the quantum number m_F of the atom. Due to the symmetry of the quadrupole field the position of the magnetic field zero-point is important and decides whether the force on an atom with a certain m_F is parallel or antiparallel to the gravity. The position of the zero-point can be changed by applying a vertical offset field and thus one can change the direction of the gradient by shifting the zero-point below or above the atoms sitting close above the surface. The effect of the changing sign of the force is shown in left graph in figure 5.16, where the offset magnetic field versus number of levitated atoms is plotted. For this measurement the atoms have been first partly polarized into the $m_F = 3$ -state, then the levitation

field was switched on and the evanescent wave was turned off for 30 ms. Additionally, we applied a variable offset field and measured the number of levitated atoms. At magnetic fields above 25 G we observe a significant increase of levitated atoms, because the atoms in the $m_F = 3$ -state experience a force antiparallel to the gravity. In this case, the magnetic field zero is above the prism surface and the sign of the field gradient leads to a compensation of the gravitational force for atoms in this state, whereas for $B < 20$ G the zero-point is below the surface and atoms in the opposite spin-state $m_F = -3$ are levitated. At about 20 G the atoms neither in $m_F = 3$ nor $m_F = -3$ don't experience any force at all, because the zero-field crosses the prism surface. This diagram shows only the dependence on the sign of the field gradient but not on the size of the field gradient.

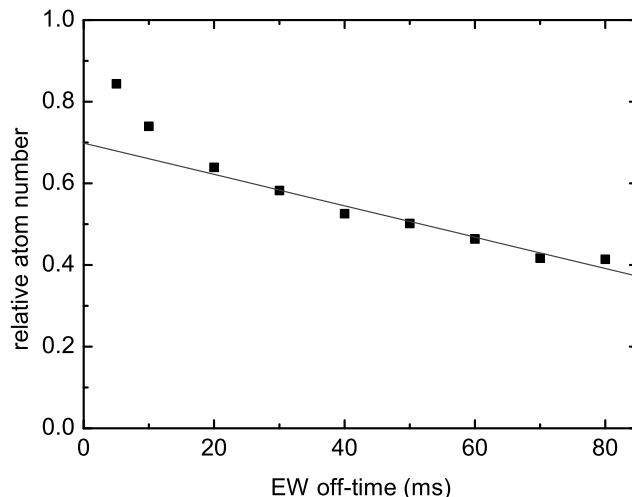


Figure 5.17: *The number of levitated atoms decreases with the levitation time respectively with the off-time of the evanescent wave. When fitting the atom numbers for $t_{off} > 20$ ms one can estimate the fraction of atoms in the levitated state.*

In order to investigate the effect of the field-gradient on the levitated number of atoms we first polarized the atoms into the $m_F = 3$ -state, then set the offset field to about 50 G and measured the number of levitated atoms for different gradient fields. In the left diagram in figure 5.16 we see a clear maximum in the atom number at a field gradient of 35 G/cm. The narrow maximum can be explained by the fact that the gravitational force is compensated only at a certain gradient. For smaller gradients the magnetic force is not large enough to compensate the gravity, for gradients above 40 G/cm the force onto the atoms in the $m_F = 3$ -state is larger than the gravitational force thus the atoms are catapulted upwards and get lost. When further increasing the levitation gradient we would observe an other peak originating from levitating atoms in

the $m_F = 2$ -state. Unfortunately the present setup doesn't allow gradient fields above 60 G/cm.

In order to determine the number of atoms in the levitated state, we varied the off-time t_{off} of the evanescent wave and measured the fraction of atoms with and without switching off the evanescent wave. As shown in figure 5.17 we observe that for off-times of less than 5 ms we lose hardly any atoms which is not surprising because at a temperature of about 10 μ K most atoms don't interact with the evanescent wave. For off-times longer than 20 ms, when all atoms would hit the surface and get lost without the levitation field, a linear decrease of the relative atom number can be observed. For times smaller than 20 ms the atom number in figure 5.17 consists of two groups of atoms, first atoms which are levitated and atoms which were not levitated but which didn't hit the surface yet and thus didn't get lost. The relative atom number for $t_{off} > 20$ ms gives us the minimal value of atoms in the levitated state. The decay is then governed by linear loss due to the imperfect shape of the field gradient. This decay is also present for off-times below 20 ms and therefore has to be taken into account when determining the number of polarized atoms. Fitting the values for $t_{off} > 20$ ms gives us the fraction of atoms populating the levitated state $F = 3, m_F = 3$. The diagram shows a value of 0.7 corresponding to a polarization of 70 %, that means that at least 70 % of all atoms populate the absolute ground state. In the current setup we reach a polarization up to about 80%. The remaining fraction of atoms populate the higher magnetic sublevels.

The polarization of the atoms is checked immediately after the polarization pulse. This procedure is made before every measurement and is repeated from time to time to check that the polarization of the atoms doesn't change. It turned out that in the daily experimental operation all settings, like polarization of the polarizer laser beam or the magnetic fields remain constant over a week and do not have to be optimized every day.

5.4.2 Feshbach Spectroscopy

The special scattering properties of cesium enable us to control the interaction between the atoms. As we have seen in section 2.3.4 when applying a variable homogenous magnetic field one can change the scattering length of an atom in the $|F = 3, m_F = 3\rangle$ -state via the Feshbach resonances. In the next chapter we will see that tuning the scattering length is very important for the evaporative cooling, since we have to set it to the right value to guarantee thermalization. We cannot directly observe the course of the scattering length, but we can observe the position of the several Feshbach resonances as increase in loss.

In order to investigate the scattering behavior we studied the dependence of loss on the applied magnetic field. First we load the dimple trap, polarize the atoms and wait for 2 s until thermal equilibrium is reached. For this measurement the temperature was 7 μ K and about 60 % of the atoms were in the lowest spin-state. Then we switch the magnetic field from an initial value of 28 G to values between 0 and 70 G and measure

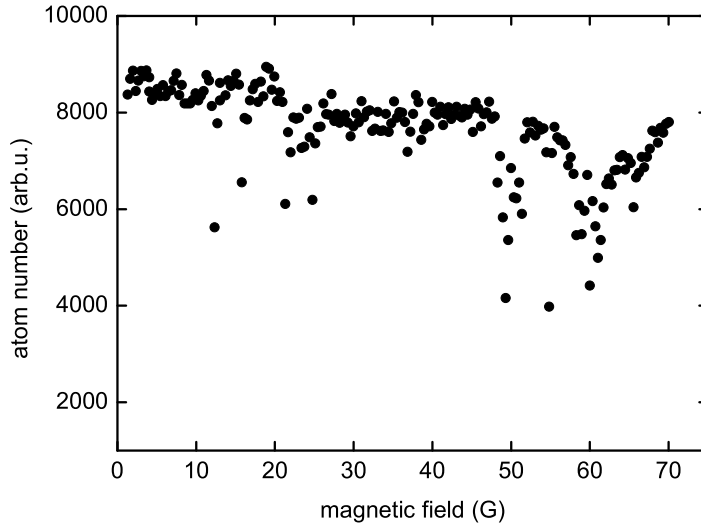


Figure 5.18: *The atom number in the dimple trap after a variable magnetic field applied for 2 s. The Feshbach resonances are relatively narrow and are therefore depicted as single dots at low atom numbers in this diagram.*

the atom number after the magnetic field was applied for 2 s. Figure 5.18 shows the measured atom number in dependence of the magnetic field. We observe many narrow dips in the atom number. Every single dip represents a Feshbach resonance, and many are not resolved in this diagram. Figure 5.19 shows a blow-up for a magnetic field between 45 G and 70 G where we resolve all resonances in this region.

For a less than completely polarized sample we expect a mixture of elastic and inelastic processes. An inelastic collision occurs when the initial scattering state couples to open channels with lower internal energy. The internal energy can be converted into kinetic energy which is in the order of the Zeeman splitting energy and thus usually larger than the trap depth. In contrast to this inelastic case, if the atoms are in the $|F = 3, m_F = 3\rangle$ -state, there is no internal energy and thus the sample is stable against binary inelastic processes when no near-resonant laser beam is present, so light induced collisions can be excluded. The only possible mechanism which allows us to observe resonances for atoms in the absolute ground state is three-body recombination. In section 3.4.2 we have seen that the three-body coefficient L_3 strongly depends on the scattering length and therefore also at densities below 10^{12} cm^{-3} the strongly enhanced scattering length leads to loss due to three-body recombination.

Since not all atoms are in the $m_F = 3$ -state and a large fraction of the remaining atoms populates also the higher spin-state $m_F = 2$, we expect to observe as well as elastic and inelastic resonances. In the range between 0 and 70 G we observe all six resonances

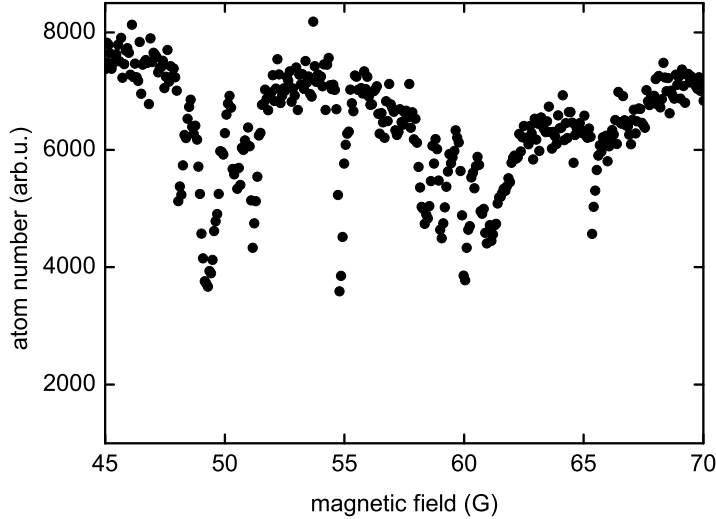


Figure 5.19: *Blow-up of figure 5.18 for magnetic fields between 43 G and 70 G, where we observe at least ten Feshbach resonances. Most of them are $|3, 3\rangle + |3, 2\rangle$ - resonances, which occur when the sample is not completely polarized and atoms in the two different spin-states collide with each other.*

for atoms in the $|3, 3\rangle$ -state, as observed in [Vul99] and [Web02]. As depicted in figure 5.19 between 45 G and 70 G we observe two of them at 47.7 G and 53.4 G. The other dips represents $|3, 3\rangle + |3, 2\rangle$ resonances originating from collisions between the atoms in the lowest spin state and atoms in $m_F = 2$, they have been already investigated in [Chi01a]. The dip at about 64.3 G indicates also a $|3, 3\rangle + |3, 2\rangle$ resonance, but it has not been observed previously.

During the evaporation we are working at 26.8 G, corresponding to a scattering length of $400 a_0$ which is large enough to provide thermalization of the sample but small enough to keep three-body processes small.

Chapter 6

Bose-Einstein Condensate in a highly anisotropic Surface Trap

In this chapter I will present and interpret the experimental results. The first Section, 6.1, is dedicated to evaporative cooling where I will show the evaporation path and all important trap and sample parameters. Then in section 6.2 I will discuss the data we obtained after the evaporative cooling before in Section 6.3 I will introduce two different methods of proving that the two-dimensional gas we observe at the end of the evaporation is a Bose-Einstein condensate. Finally in the last section, I will discuss the limitations of the present setup.

6.1 Evaporative cooling

After the atoms were pre-cooled in the MOT and in the GOST, they are ready to be loaded into the dimple trap, where the main part of the experiment happens. In the dimple trap we have to increase the phase-space density by almost 5 orders of magnitude to reach quantum degeneracy. Evaporative cooling in the dimple trap represents a very efficient cooling method and has already been used in [Web02] to realize Bose-Einstein condensation. The combination of the dimple and the vertical wedge potential is very favorable, leads to a strong density-increase when lowering the temperature and leads to a stronger compression than in the GOST. Due to the high anisotropy of the dimple trap, a regime can be reached, where the release energy falls below the vibrational quantum energy of the trap in vertical direction, leading to freezing out this degree of freedom and realization of a two-dimensional gas. In this section I will show how the important parameters change during the evaporation.

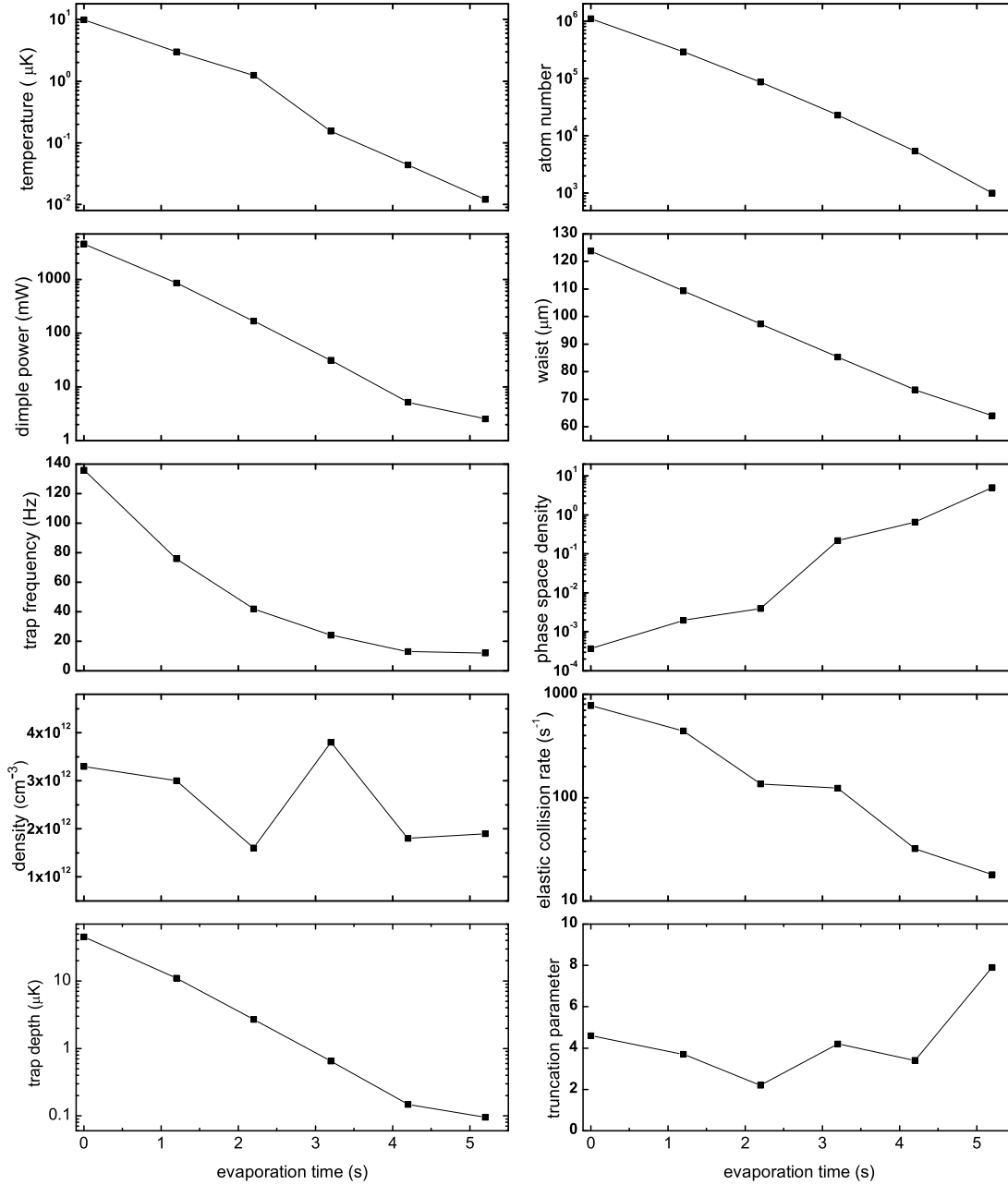


Figure 6.1: During the ramp, the atom number, the trap frequency, the waist of the dimple laser, its power and the temperature have been measured to calculate the density, phase-space density, trap depth, elastic collision rate and the truncation parameter. The ramp starts at 0 s and ends at 5 s. The final value was measured 200 ms after the end of the ramp to wait for thermalization.

Five seconds after loading the atoms into the GOST about 10^7 atoms were cooled to a temperature of $10\ \mu\text{K}$ by Sisyphus-cooling. The peak-density of the sample of $3 \times 10^{11}\ \text{cm}^{-3}$ corresponds to an elastic collision rate of about $10\ \text{s}^{-1}$ which is large enough to load the dimple trap within one second. 3.5 s after the atoms are in the GOST the red-detuned laser beam is ramped up to 4.75 W within a second to adiabatically load the dimple, then we wait for 1 s until it is fully loaded. Immediately afterwards the reservoir is removed by switching off the GOST-lasers and the atoms are polarized into the $|F = 3, m_F = 3\rangle$ -state by a 5 ms long pumping pulse. After the atoms have been polarized we measure in the dimple 1.1×10^6 atoms at about the same temperature as the reservoir, but with a phase-space density of $3.7 \cdot 10^{-4}$ which is about 40-times higher than the phase-space density of the reservoir. This increase is based on the "dimple-trick", discussed in section 5.2.1 and also the fact that the atoms are polarized.

After polarizing the atoms the magnetic bias field is switched to 26.8 G, corresponding to a scattering length of $a = 440\ a_0$. Experimentally it turned out that this value is optimal for the whole evaporation ramp and therefore it is kept constant until the end of the experimental cycle. At this scattering length losses through three-body recombination are moderate [Web03b] and the initial elastic collision rate of $\sim 700\ \text{s}^{-1}$ is large enough to guarantee fast thermalization.

To initiate forced evaporative cooling the power of the dimple laser is exponentially ramped down. The ramp consists of two subsequent exponential ramps, which has historical reasons. All results presented in this work have been achieved with this ramp. The first part of the ramp lowers the power from initially 4.75 W to 470 mW within 1.5 s, then the second ramp reduces further the power to 2.55 mW within 3.5 s. A single exponential ramp ramping the power from the initial to the same final value within 5 s gives the same evaporation efficiency.

In order to increase the loading volume and thus the loading efficiency, the dimple has an initial waist of $130\ \mu\text{m}$, but during the evaporation the waist is approximately linearly ramped down to a final value of $64\ \mu\text{m}$ within 5.5 s. 0.5 s before ramping down the dimple power the compression ramp is initialized, so both ramps end at the same time.

Figure 6.1 shows the characteristic trap and sample parameters. As we can see, the temperature decreases exponentially by almost three orders of magnitude at the cost of three orders of magnitude of atom number, leading to a phase-space density increase of 4 orders of magnitude. The figure shows that the truncation parameter η , which is the ratio between the trap depth U and the temperature T , is about 4 and approximately constant during the first part of the evaporation. At the end of the ramp it increases and reaches a value of 8 which can be explained by the relatively high uncertainty of the power measurement for low values. Comparing the truncation parameter to other experiments [Web] shows that in our case it is relatively small which results from the short life time and the reduced evaporation efficiency.

In figure 6.1 is plotted the phase-space density against the atom number during

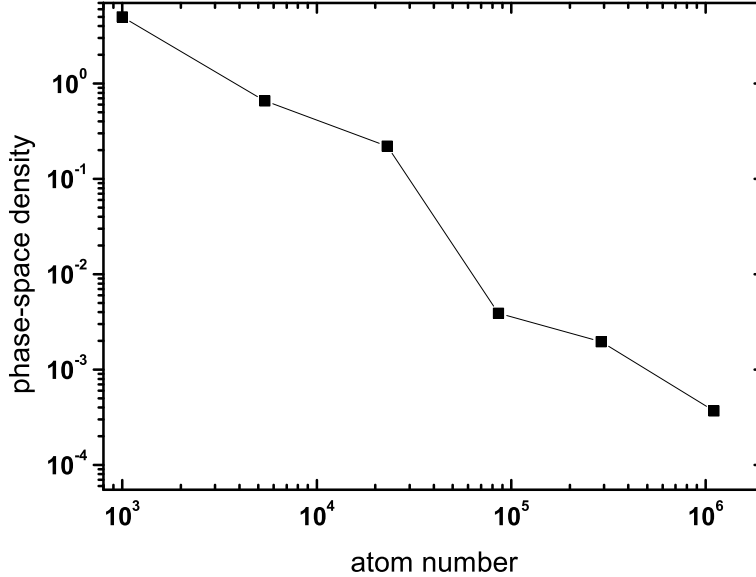


Figure 6.2: *The plot shows the increase the phase-space density in relation to the number of atoms. The slope of the connection lines corresponds to the evaporation efficiency. For the whole evaporation cycle we calculate an evaporation efficiency of 1.4.*

the evaporative cooling, starting with 10^6 atoms and reaching the phase-space density of 1 with about three thousand atoms. The connection lines between the data points correspond to the evaporation efficiency, defined in section 3.5. In this measurement we calculate an efficiency of the whole evaporation cycle of 1.4. In the measurements presented in sections 6.2 and 6.3 we had better starting conditions, and the evaporation efficiency was about two. That means that we increased the phase-space density by two orders of magnitude by losing one order of magnitude of atoms. The evaporation efficiency strongly depends on the starting conditions which are from day to day a little different, so the measurements presented in following sections were obtained with the same evaporation ramp but slightly better efficiencies.

It turned out that the evaporation efficiency is sensitive to the applied bias field. For values below 26.8 G the smaller scattering length leads to smaller elastic cross sections and thus to reduced thermalization. When the scattering length is too large, three-body recombination increases and leads consequently to reduced evaporation efficiency. Also the length of the evaporation ramp seems to be a crucial parameter, where both shorter and longer evaporation ramps lead to a decreased evaporation efficiency. The evaporation efficiency gets even worse when the waist of the dimple laser remains constant. In contrast to magnetic traps where the trap frequency remains constant during the evaporation, in our optical dipole trap the trap frequency decreases when lowering the

intensity of the dimple laser (see figure 6.1). Therefore both the initial and the final size play a major role. The larger the initial size of the dimple the more atoms can be loaded, but the dimple trick works less effectively. On the other hand a small initial dimple leads to worse starting conditions due to the poor spatial overlap with the reservoir.

6.2 Two-dimensionality

In the subsequent experiments we have used the same loading and evaporation procedure as explained in the previous section. Since the course of the evaporation depends on the starting conditions, not all presented data in this chapter have been measured under the same conditions. The results presented in this and in section 6.3 were achieved with better starting conditions and an evaporation efficiency of about 2.

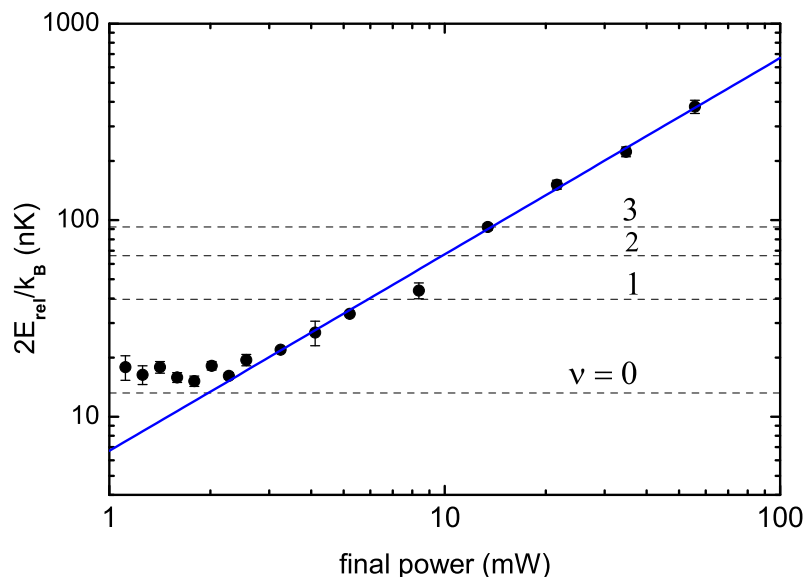


Figure 6.3: *The measurement of the vertical release energy versus the final power of the evaporation ramp shows that below about 2.5 mW the release energy doesn't further decrease. The horizontal dashed lines indicates the energies of the lowest three vibrational levels.*

In order to investigate the dependence of the temperature on the trap depth, we kept all parameters constant except the final value of the second evaporation ramp and measured the temperature at the end of the ramp. When ramping to very low final power we reach a regime where the quantum nature of the particle motion becomes important. The classical regime, where many motional states are occupied, ranges down to temperatures of about 100 nK, and in this regime, where effects of the quantized vertical

motion can be neglected, the release energy E_{rel} is directly related to the temperature as $E_{rel} = \frac{1}{2}k_B T$. In the case of BEC the release energy consists of two contributions, the kinetic energy and the mean-field energy. In the next section I will discuss the weight of these two contributions.

Figure 6.3 shows the release energy as a function of the final power P_{fin} of the second evaporation ramp. We see that the release energy first decreases linearly with the final power. The solid line illustrates the proportionality to the trap depth and shows that the evaporative cooling takes place at a constant truncation parameter, which is about six. As already observed in figure 6.1, below a certain trap depth the release energy doesn't decrease and the truncation parameter becomes larger, as the potential depth is lowered. For $P_{fin} < 3$ mW we observe that the release energy levels off at about $\frac{1}{2}k_B \times 16$ nK. A comparison to the energies $E_\nu = (\nu + \frac{1}{2})\hbar\omega_z$ of the quantum states of the vertical motion with the oscillation frequency $\omega_z = 550$ Hz shows that the release energy is limited by the zero point energy $\frac{1}{2}\hbar\omega_z = k_B \times 13$ nK, and thus the release

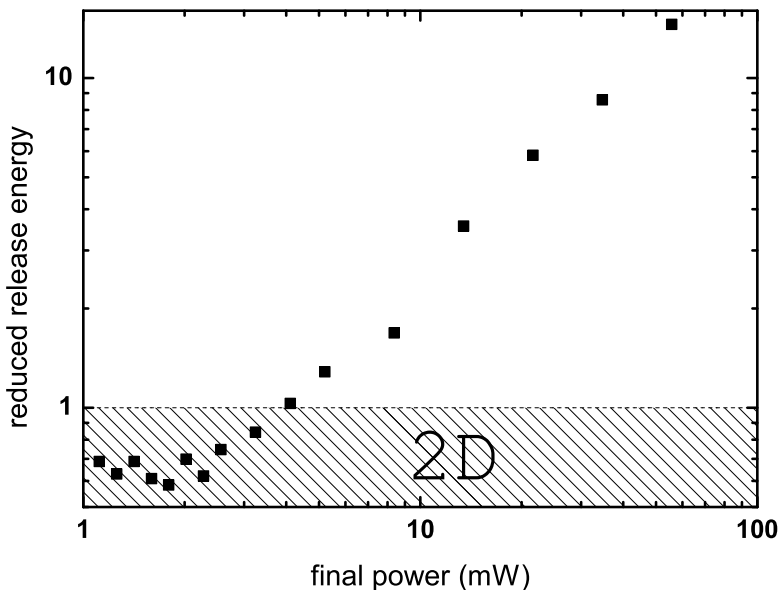


Figure 6.4: At a final power of about 4 mW the ensemble enters into a two-dimensional regime, where the reduced release energy takes a value of one. For $P_{fin} < 2$ mW we reach the lowest attainable value of $\tau = 1/2$.

energy cannot fall below this value. Since for P_{fin} below 3 mW the vibrational quantum energy $\hbar\omega = k_B \times 26$ nK is well above the measured release energy, the atoms don't have enough energy to reach the first excited state, motion in the vertical direction is "frozen out" and is limited to the ground state, a two-dimensional gas is realized. The

trap with an aspect ratio of about 50 : 1 shapes the ensemble to an atomic "pancake" with a height of 750 nm and a diameter of about 50 μm .

When the condition of two-dimensionality ($E_{rel} \approx \hbar\omega_0$) is gradually reached it is useful to introduce a reduced release energy $\tau \equiv E_{rel}/\hbar\omega_0$ which relates the release energy to the vibrational quantum energy. In figure 6.4 the reduced release energy is plotted against the final power. We see that at about 4 mW, when $\tau \sim 1$, the gas enters into the two-dimensional regime. Below 2.5 mW the lowest attainable value of the reduced release energy of $\tau = \frac{1}{2}$ is reached. When the expansion energy is equal to the ground state energy $\frac{1}{2}\hbar\omega_0$, almost all atoms of the ensemble populate the ground state of the vertical motion.

6.3 Bose-Einstein condensation

Until now we have seen that we have produced a two-dimensional quantum gas, but we haven't seen any evidence that this gas is Bose condensed. According to calculations of the phase-space density from the temperature and the experimentally determined trap frequency, the onset of the BEC is expected at a final power of about 10 mW.

In the most experiments the striking proof of the presence of a condensate is the observation of the typical two-component distribution, where the condensate can be clearly distinguished from the thermal cloud. Unfortunately, in our setup the release-and-recapture method doesn't provide sufficient information to extract such a two-component distribution of the ensemble. And also in the data shown in figure 6.3 and 6.1 we don't observe any evidence of a phase transition. Later we will see that we don't expect to observe such evidence for a transition in the measurement of the release energy. In order to prove the presence of the condensate we have developed two indirect methods which I will explain in the following paragraphs.

A Bose condensed atomic gas differs from a thermal gas in the mean-field interaction, where in the case for the condensed atoms $E_{int} \gg E_{kin}$. As lifetime measurements have shown in a very dilute thermal gas the atoms don't really "care" about the sign of the scattering length and their decay depends only on the size of the scattering length. But in a degenerate quantum gas, due to the enhanced density, the negative sign of the scattering length leads to an attractive interaction between the atoms and thus to a collapse of the condensate. Our method to prove the presence of a BEC is based on such a controlled collapse of the trapped ensemble [Rob01b]. For cesium, the scattering length becomes negative for values below 17 G and takes very large values for small bias fields. After the evaporation which took place at a bias field of 26.8 G, we hold the dimple power at the final value of 1.6 mW, switch the magnetic field within about 10 ms to a variable bias field between 0 G and 70 G for 20 ms, and switch it back to 26.8 G within next 10 ms. The measured atom number after this procedure is normalized to the atom number measured when repeating the cycle without ramping the magnetic field.

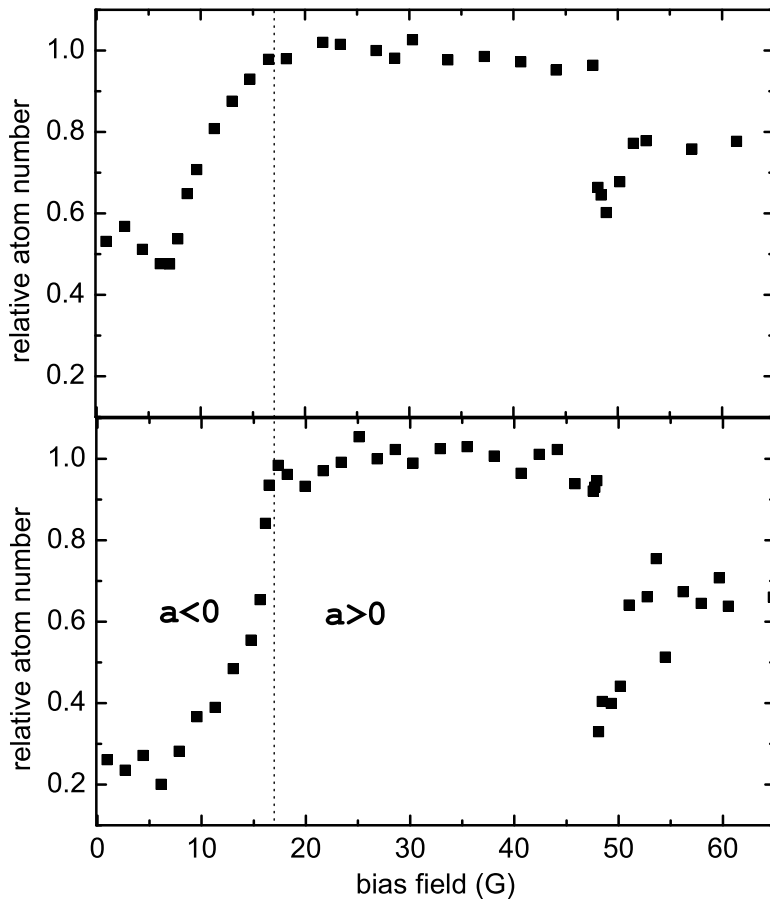


Figure 6.5: Atom number versus magnetic field applied for 20 ms for two different release energies. The lower graph shows the collapse of an ensemble with a release energy of $\frac{1}{2}k_B \times 16$ nK, whereas the upper graph shows the same measurement for a thermal cloud with a temperature of 170 nK. Due to a large Feshbach resonance at 47.7 G we observe a significant loss at this magnetic field value in both cases.

The lower diagram in figure 6.5 shows the relative atom number against the magnetic field, applied for the short interval. We see that switching the magnetic field to values between 17 G and 47 G, corresponding to a positive scattering length between 0 and $\approx 1000 a_0$, doesn't lead to any loss. When ramping the field below 17 G, the scattering length becomes negative and a rapid decrease in the atom number can be observed. Already at 14.75 G, where $a = -150 a_0$, almost half of the atoms are lost.

In the upper graph of figure 6.5 we see the same measurement for a thermal cloud, where no rapid loss can be observed. This shows that the sudden loss of atoms in the lower graph cannot be explained by the usual three-body loss, because at this scattering

length the three-body loss coefficient is relatively small [Web03b]. This loss can only be explained by the huge density increase occurring during the condensate collapse, after which three-body recombination leads to the rapid loss. The drop of the atom number in the thermal cloud below 14 G can be explained by the very large negative scattering length, where the three-body loss coefficient becomes significant. Also above 47 G we

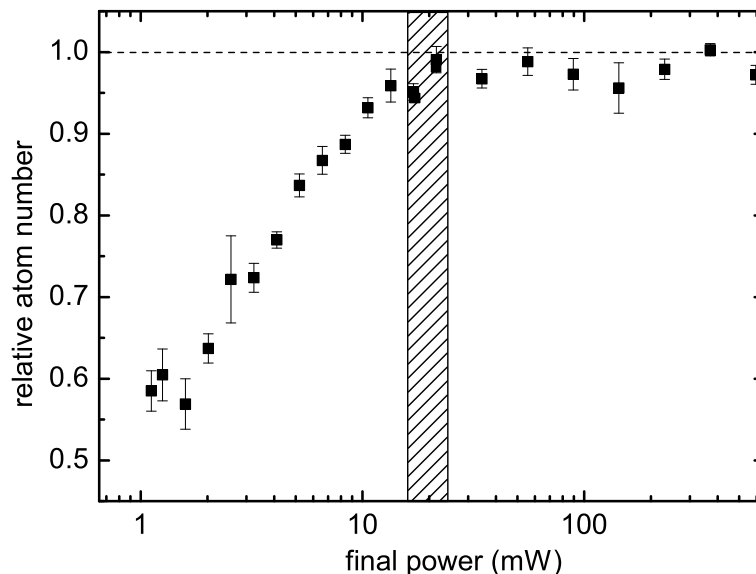


Figure 6.6: Observation of a phase transition at about 20 mW, where the relative atom number decreases after the scattering length has been adjusted to $a = -150 a_0$ for 20 ms at the end of the evaporation ramp.

can observe a reduced atom number. This can be explained by the presence of a narrow Feshbach resonance at 47.7 G, where the scattering length becomes negative and the condensate collapses. Atom numbers above 48 G, where $a > 900 a_0$, are reduced due to the fact that the magnetic field is ramped relatively slowly over the narrow Feshbach resonance and most atoms get lost in that time. Another big difference between the thermal and condensed sample is the relative loss. At the 47.7 G-resonance for example, we lose about 40 % of the atoms in a thermal cloud, whereas in the condensed sample we lose 70 %, demonstrating the greatly increased density.

The fact that we don't lose all atoms of the condensed sample, when making the scattering length negative, may be explained by the fact that the condensate is not pure. There are some atoms in the thermal cloud which are not affected by the negative scattering length. But even for pure condensates one doesn't expect that all atoms are lost after a collapse [Don01, Web02].

To show the final power at which the condensate occurs we measured the induced

collapse loss as a function of the final power. For this measurement we kept the length of the evaporation ramp constant and varied only the final value of the second part of the ramp. At the end of the evaporation we ramped the magnetic field for 20 ms to 14.75 G, where for the condensed ensemble we observed a loss of almost 50%. Figure 6.6 displays the relative atom number against the final power of the evaporation ramp. For values above 20 mW no significant loss is observed as we expect for a thermal gas, where the negative scattering length doesn't lead to any significant effect. Decreasing the power below 20 mW leads to increasing loss which can be explained with a collapse of a condensate which becomes larger with decreasing power. Now, we can see that the phase transition takes place at a final power of slightly below 20 mW, where we have 15000 atoms left at a temperature of 150 nK. This value lies in the error range of the calculated temperature for the transition we expect at roughly 10 mW.

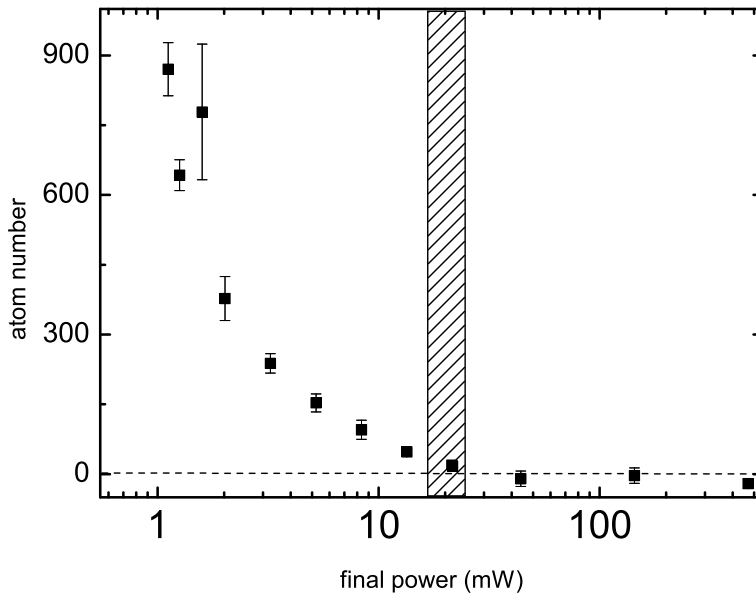


Figure 6.7: *Horizontal release-and-recapture measurement, which shows the remaining atom number after 400 ms horizontal expansion without horizontal confinement versus the final power of the evaporation ramp. Ramping below 20 mW leads to increased number of recaptured atoms, what can be led back to modified expansion behavior of the sample.*

In order to investigate the behavior of the ensemble we studied its horizontal expansion by using a horizontal release-and-recapture method. We expect that a condensate expands much slower than a thermal gas. The same evaporation ramp, with variable final value, as used in the previous measurement prepared a cold sample. The magnetic field was kept at 26.8 G during the evaporation and the expansion measurement. At

the end of the evaporation the horizontal confinement was switched off by blocking the dimple laser and the atoms expanded horizontally. After 400 ms the dimple laser was turned on again to a fixed power of 22 mW and the remaining atoms were recaptured.

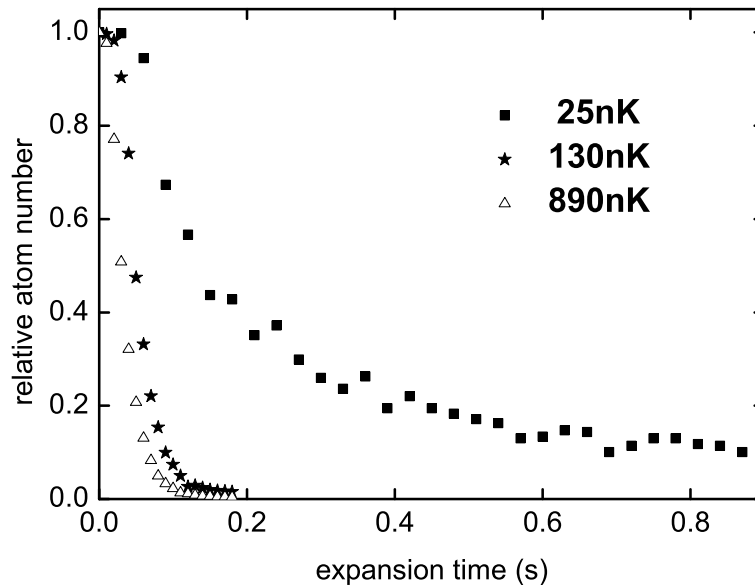


Figure 6.8: *The horizontal release-and-recapture measurements for ensembles with different vertical expansion energies. The Bose condensed and the two thermal ensembles can be clearly distinguished.*

As shown in figure 6.7, no atoms are recaptured when the final power is larger than 20 mW. After this 400 ms no thermal atoms remain in the dimple region, but for a deeper evaporation, where $P_{fin} < 20$ mW, the atom number increases. This behavior can be explained by the much slower expansion of the fraction of the condensed atoms, which becomes larger for decreasing final power. The fact that the recapture signal appears at the same final power as the collapse of the sample (figure 6.6) strongly supports the interpretation that this transition can be explained by the formation of a condensate.

An important question is whether this effect can be explained by the fact that the sample becomes colder with decreasing power and then this increased fraction of cold atoms expands more slowly than hot atoms at higher final power, leading to increased recapture signal. The total number of atoms at the end of the evaporation ramp strongly decreases with decreasing final power. When ramping the power to 50 mW we observe about 25000 atoms, while for $P_{fin} \sim 1.1$ mW the atom number is reduced by more than a factor of ten. For the horizontal release-and-recapture measurement we recapture the horizontal expanding atoms into a dimple with a constant power of 22 mW. So the atoms have to travel a distance of typically 100 μm to leave the recapture area during the

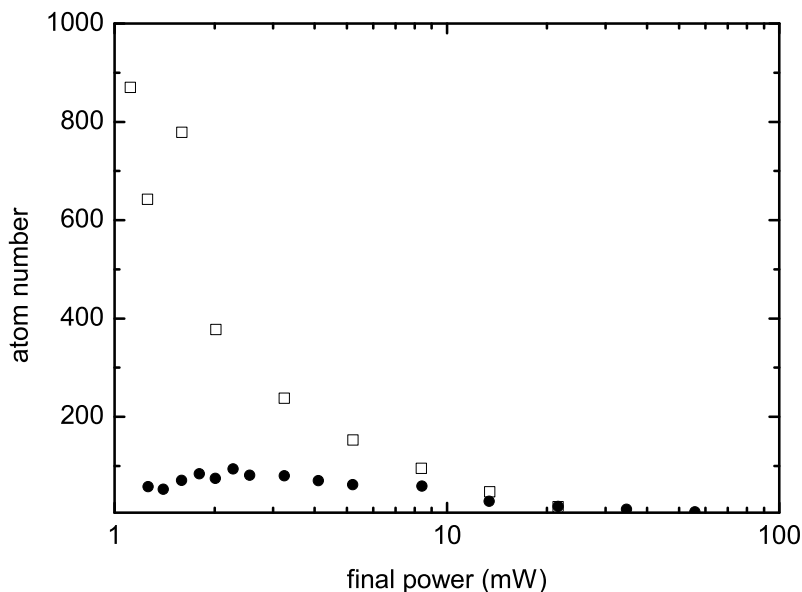


Figure 6.9: *The estimated number of atoms with a release energy smaller than 2 nK (filled circles) and the atom number recaptured after 400 ms of horizontal expansion (see also figure 6.7). We assumed a thermal gas and calculated the number of cold atoms for ensembles we observed at the end of the evaporation ramp before the dimple laser was turned off.*

400 ms . Assuming a thermal cloud, we can estimate the velocity and thus the expansion energy of atoms which are recaptured by the dimple. Atoms with velocities larger than $250\text{ }\mu\text{m/s}$, corresponding to an kinetic energy of $k_B \times 2\text{ nK}$, get lost. Assuming a Maxwell-Boltzmann distribution we can estimate the number of atoms with a kinetic energy smaller than 2 nK . As we can see in figure 6.9, the calculated atom number in the relevant region ($P_{fin} < 10\text{ mW}$) is much smaller than the atom number recaptured after the expansion. For a final power of 1.1 mW the calculated atom number is more than a factor of ten smaller than we observe, which shows that the recaptured atom number cannot be explained by the fraction of cold atoms expanding very slowly. Also the dependence of the calculated atom number on the final power shows that for $P_{fin} < 8\text{ mW}$ this fraction of cold atoms levels off and doesn't increase for smaller values of the final power.

Figure 6.8 shows a typical horizontal expansion of atom ensembles for three different vertical release energies. The left curve shows a relative atom number (the atom number is normalized by the atom number without removing the horizontal potential) for different expansion times for a sample at a temperature of $0.89\text{ }\mu\text{K}$. Also for the 130 nK -ensemble after 150 ms there are almost no atoms recaptured by the dimple, even if the initial number of atoms is ten-times higher than for the Bose condensed sample with

an release energy of $\frac{1}{2}k_B \times 25$ nK, where even after 400 ms of horizontal expansion 20 % of the original atoms are left. For smaller release energies, we observed small number of atoms even after several seconds of free horizontal expansion on the evanescent wave without the confining dimple beam. Such long expansion times can be explained by the fact that due to the geometry of the sample, the condensed atoms expand predominantly in the vertical direction; in the horizontal direction, there is almost no expansion.

Now, we return back to figure 6.3 and analyze under which condition the transition takes place. At a final power of about 20 mW, where the phase-transition happens, we measure a release energy in the range of 100 nK. At this energy the atoms populate about five vertical states and thus the transition takes place in a 3D regime. With decreasing power, the fraction of condensed atoms increases and at about 4 mW, where the release energy is equal to the vibrational quantum energy and more than 60 % of all atoms populates the ground state, the condensate enters the 2D-regime. For $P_{fin} < 2$ mW a two-dimensional BEC is formed. Further decrease of the potential depth leads to increased atom number in the fraction of condensed atoms, where the release energy is dominated by the zero-point energy.

Roughness of the evanescent wave

For temperatures of about one microkelvin the vertical oscillation period is much smaller than the time it takes an atom to move from the perimeter of the dimple laser. Therefore it will experience many reflections from the evanescent wave before getting away, and thus the horizontal expansion cannot be considered as a pure ballistic motion but has rather a diffusive character. In a real experiment the roughness of the evanescent wave is sufficient to cause diffuse rather than specular reflection. There are several mechanisms responsible for the roughness of the evanescent wave. The most important is the surface roughness, which is on the angstrom scale and is comparable to the evanescent wave roughness [Hen97]. Furthermore, residual stray light, originating from defects on or below the prism surface or from reflections, may interfere with the evanescent wave, leading to random spatial variations of the evanescent wave potential. Experimentally we can vary only the decay length of the evanescent wave to affect the roughness of the evanescent wave. The larger is the decay length the better the roughness of the prism surface can be compensated and the fewer distortions in the potential.

For the subsequent measurement we reduced the decay length of the evanescent wave by changing the angle of incidence. All other measurements presented in this chapter have been performed in a dimple trap, where the evanescent wave angle of incidence was set to about 0.25° above the critical angle. This angle corresponds to a decay length of $\Lambda = 1.4 \mu\text{m}$. Setting the angle to 2° above the critical leads to a three times smaller decay length of the evanescent wave. While in the first case the atoms were sitting about $4 \mu\text{m}$ above the surface, at this relatively large angle the atoms sit about $2 \mu\text{m}$ closer to the surface.

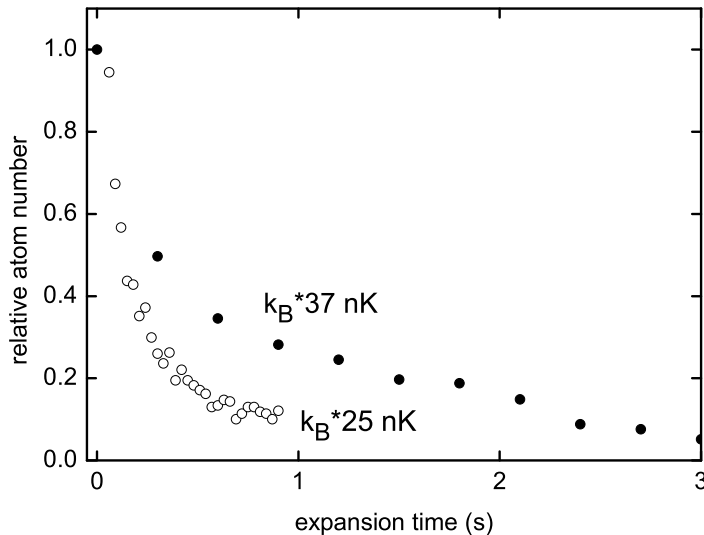


Figure 6.10: *The relative atom number versus the expansion time for two different decay lengths of the evanescent wave. While the sample with a release energy of $k_B \times 25 \text{ nK}$ (on an evanescent wave with $\Lambda = 1.4 \mu\text{m}$) decays relatively fast, in the other case ($\Lambda = 0.5 \mu\text{m}$) we observe a small fraction atoms even after several seconds of horizontal expansion. Both samples were Bose condensed and the vertical potential was approximately the same in both measurements. Further we see that the vertical release energy doesn't really affect the horizontal expansion.*

We have observed that for the same vertical trap depth as in the previous measurements we trapped about five times less atoms. We had to decrease the detuning by about a factor of four in order to get the same atom number. This fact may be explained by shallow wells in the evanescent wave where the potential depth is not sufficient to prevent the atoms hitting the prism surface. We have also observed that at this reduced angle of incidence the adjustment of the position of the dimple laser is much more sensitive since there seems to be many more surface defects leading to leaks in the evanescent wave potential.

In horizontal release-and-recapture measurements we have observed that for condensed atoms the horizontal expansion was even slower than in the previous measurements (figure 6.8), we observed a considerable number of atoms, even after few seconds of free horizontal expansion. On the other hand the expansion time of a thermal cloud was not really affected by changing the decay length of the evanescent wave. The fact that changing the decay length, the most important property of the evanescent wave, affects the horizontal expansion behavior may be explained by corrugations in the evanescent wave which only affect the expansion of condensed atoms. The increased expansion times may be due to a trapping effect which could emerge from a pinning of the conden-

sate wave function to such defects. The larger these corrugations and the more often they occur the more the horizontal expansion would be affected by this trapping effect. But we can exclude the possibility that the sample is divided into many fractions in small potential wells. The atom number of such a fragmented condensate would be too small to lead to a collapse, when changing the sign of the interaction.

We have repeated the measurement displayed in figure 6.3 in order to study the influence of the changed decay length onto the two-dimensionality. As expected, the small decay length leads to higher vertical trap frequency of 850 Hz and thus to larger spacing between the quantum energies for the vertical motion. We observe the same behavior as depicted in 6.3, with release energy levels at about $\frac{1}{2}k_B \times 37$ nK, slightly above the zero-point energy of $\frac{1}{2}\hbar\omega_z = k_B \times 20$ nK. Also in this case we observe the same signature for the presence of a two-dimensional gas. Collapse measurements confirm that the gas is Bose condensed. The number of atoms we observed at the end of the evaporation was smaller than in the previous measurements which may be explained by the reduced lifetime and the reduced detuning of the evanescent wave and thus increased scattering rate.

It turned out that it is possible to realize a 2D-BEC in a dimple trap with reduced distance to the surface at the cost of reduced detuning and thus smaller atom number. The realization seemed to be more difficult due to the high sensitivity to surface defects and also the behavior of the atoms, for example their horizontal expansion, was strongly influenced by the modified potential of the evanescent wave.

Role of the Chemical Potential

In the trap the total energy of the atoms consists of three contributions, the potential energy in the harmonic potential, the kinetic energy and the interaction energy. To measure the release energy the vertical trapping potential is non-adiabatically turned off, so the first contribution suddenly vanishes and the remaining two are transformed into pure kinetic energy of the expanding cloud. This quantity represents the actually release energy we measure. Usually, as in the most BEC experiments, in the Thomas-Fermi regime the interaction energy dominates the release energy and the kinetic energy part can be neglected. In our case the weight of the two contributions to the release energy strongly depends on the size of the condensed fraction and on the dimensionality of the system. In the three-dimensional case the interaction energy strongly contributes to the release energy, but when reaching the 2D-regime the dominant ground-state energy makes the interaction energy less important.

The behavior of the atoms in this regime can be considered a following: while in the vertical direction the release energy is dominated by the zero-point energy, horizontally many motional quantum states are occupied. When the gas freely expands the evolution is strongly dependent on the confinement. Whereas in the vertical direction the size of the expanding cloud increases rapidly as a consequence of the repulsive effect associated

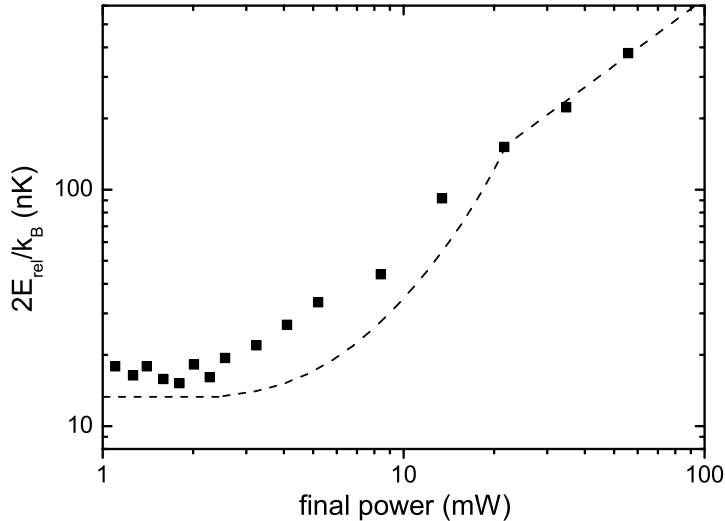


Figure 6.11: *The measured release energy versus the final power (as already shown in figure 6.3). The dashed line represents schematically the release energy predicted for a finite number of non-interacting bosons. The measured data matches with the theory for a thermal cloud ($P_{fin} > 20$ mW) and in the two-dimensional regime. The discrepancy for $P_{fin} \sim 3 - 20$ mW can be explained by the interaction energy.*

with the gradient of the density, in the horizontal direction the expansion proceeds very slowly. In our trap the aspect ratio is about 50, so the condensed sample expands predominantly in the vertical direction. That means that the vertically measured release energy reflects essentially the whole interaction and the vertical kinetic energy of the sample.

Figure 6.11 shows the measured release energy (as already shown in figure 6.3) and a schematic illustration of the release energy we expect for the case of non-interacting Bose gas after lowering the potential with constant truncation parameter and considering T/T_c [Pit03]. We can divide the curve into three regimes: for $P_{fin} > 20$ mW, where we observe only a thermal gas, we expect a linear dependence. At the critical power of about 20 mW the gas begins to condense and the curve becomes steeper. This transition regime leads to the two-dimensional regime where the release energy is dominated by the ground-state energy. We see that in the transition regime the measured data points are slightly above the dashed line corresponding to a non-interacting gas. This deviation can be explained by the interaction energy, which is included in the measured release energy. For $P_{fin} < 3$ mW the measured data points are slightly above the expected curve, since the interaction energy in the two-dimensional regime becomes less important and the release energy mirrors the zero-point oscillations. This small difference between the measured and expected curves can be explained by the inhomogeneous evanescent wave

which leads to the fact that the atoms sit at different heights above the prism and thus the release energy measurement is slightly falsified.

In the transition regime we can calculate the chemical potential and thus the interaction energy of the condensate as a function of the final power. For the calculation of the chemical potential we use the formula 2.16 introduced in the second chapter. We can use this formula only for the case where the condensate is three-dimensional. For P_{fin} below approximately 3 mW the Thomas-Fermi approximation is no longer valid since the contribution of the ground-state energy to the release energy becomes larger and dominates in this region. As we have seen in section 6.2 we reach the real 2D regime at about 2.5 mW where the chemical potential has to be treated two-dimensionally. In this case an exact solution is quite complicated. But we can assume that the density of the gas is reduced as a consequence of the fixed vertical extension of the cloud (as discussed in section 2.2.2). Thus we can assume that the chemical potential becomes smaller with decreasing power and can be even neglected at very small final power.

In order to calculate the interaction energy for the three-dimensional regime we have to estimate the atom number in the condensate, since with our image technique we are not able to measure the fraction of condensed atoms. Typically at about one third of the critical power one obtains a pure condensate and the atom number in the thermal cloud can be neglected [Web]. In our case at about 7 mW we expect a pure condensate. Now we can estimate the interaction energy in the transition regime. At $P_{fin} = 5.2$ mW we observe about 6000 condensed atoms and calculate an interaction energy of $E_{int}/k_B = 4/7\mu = 15$ nK. We see that in this region the gap between the data points and the schematic curve can be approximately explained by the interaction energy. The presence of the interaction between particles leads to discrepancy between the measured data and the prediction for an ideal gas, therefore it is hardly possible to observe any sign of a phase transition in figure 6.11.

In [Ens96] a measurement of the release energy as a function on the scaled temperature T/T_C has been performed in a magnetic trap, where the dependence of the release energy on the scaled temperature showed a smooth sign of a transition at the critical temperature. In a system with a large interaction energy, as it is the case for ensembles with a large scattering length, the dependence is expected to be even smother and one does not expect to observe an evidence for a phase-transition.

6.4 Limitations

In order to be able to observe and investigate the behavior of the condensate in the 2D-regime we need more atoms in the condensed fraction. Therefore we investigated the limitations of the current setup and how the trap properties affect the evaporation and finally the number of condensed atoms. We already know that the polarization of the atoms play a crucial role during the evaporation. For a polarization degree of

less than 60 % we don't reach quantum degeneracy because due to the increased loss the evaporation efficiency is less than 1. We have further observed that the evanescent wave also plays an important role, not only in its detuning, which determines the atom number after the evaporation, but also in the decay length of the evanescent wave which affects the properties of the optical potential. In the next paragraphs I will present the investigation of the influence of the evanescent wave and the magnetic field on the evaporation.

6.4.1 Evanescent Wave

As we have seen in the previous section the quality of the evanescent wave is very important in respect to the atom number and lifetime of the sample and thus determines the efficiency of the evaporative cooling. Even a small imperfection in the evanescent

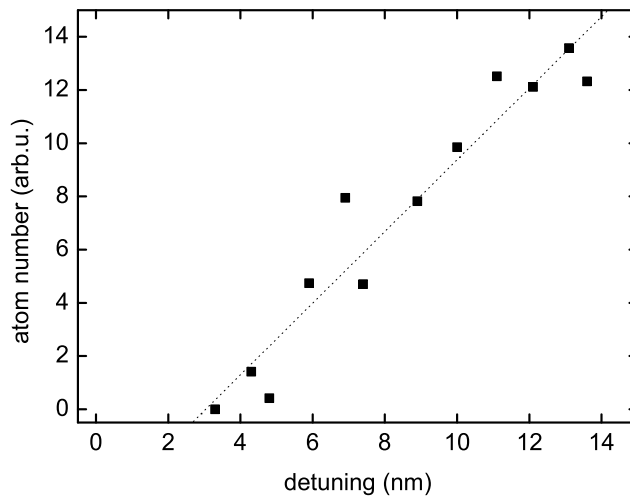


Figure 6.12: *The plot shows the dependence on the number of atoms after the evaporation for different evanescent wave detunings at a constant vertical potential.*

wave potential leads to strong loss and thus to reduced evaporation efficiency and finally to reduced number of condensed atoms. Not only is the roughness of the evanescent wave important, the stray light originating from defects on or below the surface may lead to reduced lifetime due to photon-scattering. Since such stray light cannot be fully avoided experimentally, therefore we have to reduce its influence on the trapped sample. We investigated the influence of the detuning of the evanescent wave on the atom number at the end of the evaporation.

Changing the detuning of the evanescent wave leads to two important effects: when the detuning is decreased at a constant power of the laser beam, the potential depth becomes larger but the number of inelastic light assisted collisions also increases. The

later effect is especially unfavorable at high densities and low potential depths as is the case during and at the end of the evaporation ramp. In order to investigate the influence of the detuning on the number of atoms at the end of the evaporation ramp we changed the detuning but kept the potential of the evanescent wave constant to separate these two effects.

For this measurement we used the same 5 s long evaporation ramp, keeping the final value at 1.6 mW and the bias magnetic field constant. Then at the end of the evaporation we measured the atom number for different detunings of the evanescent wave. In figure 6.12 we see that the smaller the detuning the fewer atoms remain in the trap after the evaporation. Since density of the ensemble is 10^{12} - 10^{13} cm^{-3} during the evaporation the number of inelastic light induced processes strongly increases, as the detuning is lowered, the reduced atom number for small detunings can be explained by an increased loss due to light induced collisions.

Considering figure 6.12 in this region there seem to be a linear correlation between the atom number and the detuning. Since we are limited in the power of the evanescent wave, an increase of the detuning above 14 nm is not possible without decreasing the potential depth. In the future experiment it would be more favorable to work at even larger detunings and higher powers of the evanescent wave.

6.4.2 Magnetic Field

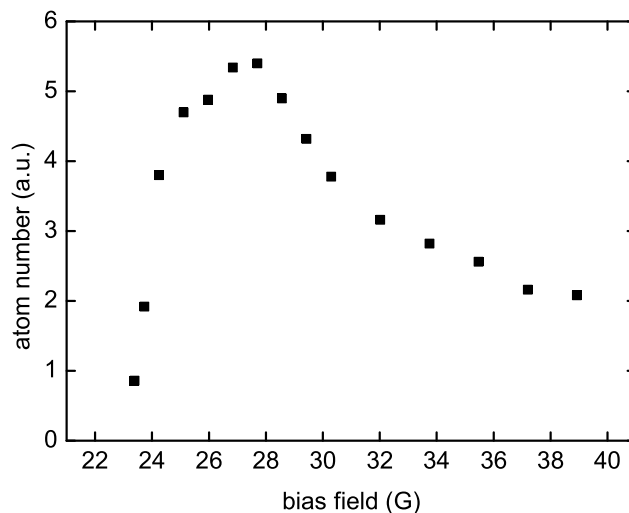


Figure 6.13: *Number of atoms after evaporation and 200 ms horizontal expansion versus the applied bias field. We observe a clear maximum at 27 G corresponding to a scattering length of $440 a_0$.*

In order to find an optimum value for the bias field, applied during the evaporation,

the fraction of atoms in the condensate as a function of the bias field was investigated. For this measurement we used the standard evaporation ramp with a final value of 1.6 mW, at the end of which we turn off the dimple beam for 200 ms and observe the number of recaptured atoms after horizontal expansion. The number of recaptured atoms is

proportional to the atom number in the condensate. As we can see in figure 6.13, the number of atoms exhibits a clear maximum at about 27 G. For higher magnetic fields the corresponding scattering length is higher and leads to stronger loss due to three body recombination and therefore to reduced evaporation efficiency. For scattering lengths below $440 a_0$ the elastic cross section is too small, and the ensemble cannot thermalize during the evaporation.

This maximum shifts slightly when varying the length of the evaporation ramp. For short ramps the maximum is broadened to higher fields because higher bias field correspond to larger scattering length and thus to higher thermalization rate which is needed for small cut-off parameters. This measurement showed that for our standard ramp a bias field of 27 G is an optimal value, where the elastic cross section is large enough to ensure sufficient thermalization during the evaporative cooling and small enough to keep the three-body loss moderate.

Chapter 7

Outlook

In the last chapter we have seen that due to the low number of atoms in the condensate a deeper investigation of the two-dimensional degenerate quantum gas was hardly possible. Further the control of magnetic fields limited a deeper investigation of the properties of the sample. In order to increase the number of condensed atoms we must first increase the initial number of atoms in the dimple trap. Measurements of the transfer efficiencies show that we lose most atoms during the transfer from the MOT into the GOST, where only a few percent of the atoms released from the MOT are trapped. This can be explained by the relatively large release height and poor spatial overlap of the compressed MOT and the GOST. In order to increase the number of atoms in the condensate there have to be done several technical improvements which are summarized in Section 7.1 before in Section 7.2 the future experiments will be explained.

7.1 Technical Improvements

The present setup consisting of a large steel chamber, with limited number of viewports, limits the exact control of magnetic fields and the optical access. For these reasons the old chamber will be replaced by a newly designed glass cell which has many advantages and will open new avenues of investigation to the experiment in the future.

Control of Magnetic Fields

As has been previously mentioned, the control of the magnetic fields plays a crucial role in the experiment. It is important to switch the magnetic field within a few milliseconds allowing large magnetic gradients to be generated while also keeping the applied magnetic field stable with an accuracy of less than one percent. Due to eddy-currents and residual magnetization of the steel chamber these requirements could not be fulfilled in the present setup. The new setup consisting of a glass cell will allow many coils to be precisely arranged very close to the sample allowing us to trap the atoms magnetically.

Magnetic trapping and transport into the GOST would increase the number of transferred atoms and thus improve the starting conditions for evaporative cooling. With adiabatic transfer into the GOST, a cool atom reservoir could be prepared without the need for Sisyphus-cooling in the evanescent wave and also without the associated two orders of magnitude loss in atom number.

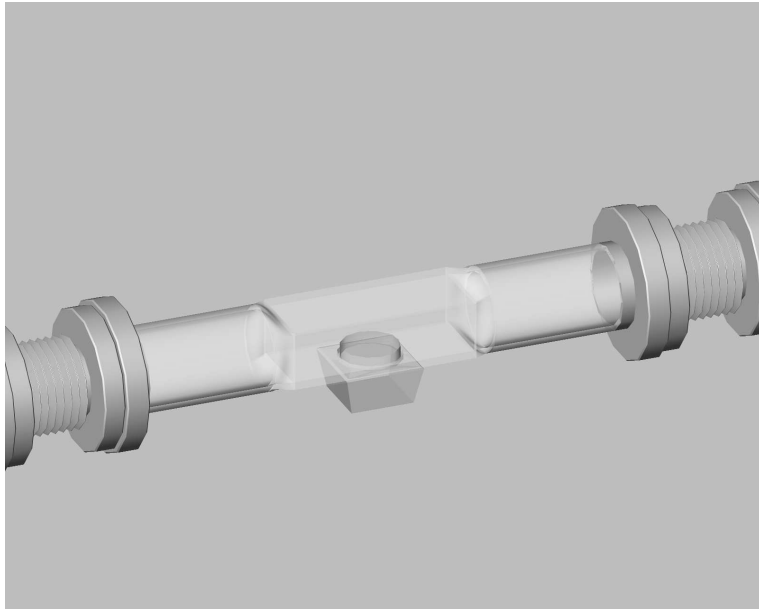


Figure 7.1: *Schematic picture of the new designed glass cell. The prism in the shape of a frustum of pyramid is glued to the bottom side of the cell. This glass cell will replace the main chamber while the rest of the vacuum setup will remain the same (see figure 4.1).*

Further, a better control of the magnetic fields would offer the possibility of applying an exact magnetic levitation field to compensate for gravity, enabling us to lift the cloud and then to observe free expansion after releasing the atoms. Such a “time-of-flight” method is a standard technique in many BEC-experiments to measure even very low release energies. For enhancing the anisotropy of the trap, the atoms can be magnetically pressed against the evanescent wave by applying an opposing magnetic field gradient to that which we use for levitation. This enables us to enter into the two-dimensional regime at higher release energies.

The absence of eddy-currents, when using a glass cell, makes it possible to switch the magnetic fields very rapidly and precisely which is important when releasing the atoms or when ramping over a Feshbach resonance in order to create molecules [Her03].

Optical Access and New Trapping Schemes

In the present setup optical access to the prism was limited to the 13 relatively small viewports. When using a glass cell, where the prism will serve as the bottom of the cell, the position of the incoming laser beams need not be restricted to the viewports, and an additional camera for absorption imaging can be installed. This will make it possible to directly measure the density and expansion properties of the atoms.

The better optical access and a new prism in the shape of a frustum of a pyramid will also make it possible to create novel potentials. Retro-reflection of the evanescent wave would produce an interference pattern also leading to strong confinement also in one horizontal direction. One could additionally freeze out the motion in this strongly confined direction and create a one-dimensional degenerate quantum gas. When using an additional evanescent wave created by a laser sent from the other prism side one could realize an optical surface lattice, leading to strong confinement in both horizontal directions (see figure 7.2).

Lifetime

In the present experiment the lifetime of the sample is limited mostly by two processes: inelastic two-body collisions due to the presence of small fractions of atoms in higher magnetic substates, and by the loss of atoms through “holes” in the evanescent wave. Employing a magnetic transfer of the atoms into the GOST will lead to a fully polarized sample. This will not only increase the lifetime and thus increase the efficiency of the evaporative cooling, but it will also improve the tunability of the sample.

As we have seen in the previous chapter, the horizontal expansion is strongly influenced by the quality of the evanescent wave. Imperfections on the dielectric surface where they seem to locally reduce the potential depth of the EW potential lead to further reduced lifetime. Using a high quality glass substrate and super-polished prism surface would reduce defects both below the surface, producing stray light, and at the surface leading to corrugations in the optical potential. This would increase the lifetime and reduce stray light coming from such scattering spots.

7.2 Future Experiments

The highlighted improvements will enable us to increase the number of atoms in the condensate. With such a two-dimensional condensate we will then have the unique possibility to investigate the properties of quantum systems with reduced dimensionality.

In the three-dimensional case the phase-coherence of the condensate has a global character whereas in a system with reduced dimensionality the atomic gas exhibits phase fluctuations, as is the case in very elongated 3D trapped Bose gases [Det01]. In a 2D system, at finite temperatures, the coherence length is smaller than the extension of

the ground state wave function. Observing the interference pattern between two clouds, simultaneously ejected from different parts of the sample, allows the reconstruction of the spatial coherence properties of the sample. The trapped two-dimensional condensate will enable us to study its coherence properties, in particular how this properties change during the transition from 3D into the 2D regime. Since the phase fluctuations are dependent on temperature [Pet00], it is of interest to observe how the phase-fluctuations change with decreasing temperature. Furthermore it would be possible to study ele-

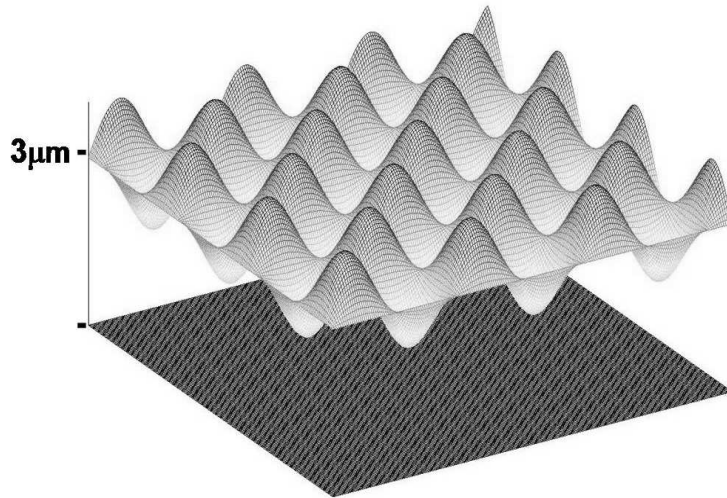


Figure 7.2: *Interference between two evanescent waves produced by two retro-reflected laser beams sent into the prism perpendicular to each other produces an optical surface lattice.*

mentary excitations such as vortices and solitons in the 2D regime. These excitations are expected to exhibit striking differences to the 3D case. For example in 2D they are believed to be much more stable, whereas in 3D, vortices can bend and solitons suffer from kink instabilities. The character and spectrum of the collective oscillations are proposed to be qualitatively different for example single vortices performing circular motion are predicted to decay via sound emission [Lun02]. The striking advantage of our experimental setup is that we have one large “pancake-condensate” instead of many stacked pancakes as is the case in a standing wave. This will allow us to excite and to observe such collective oscillations in the 2D regime without averaging over many “pancakes”.

With the modified apparatus we will be able to create an optical surface lattice by using two retro-reflected evanescent waves. There we could study quantum phase transitions such as the transition from the superfluid phase to the Mott insulator phase [Jak98, Gre02] in a system consisting of atoms with repulsive interaction between atoms

hopping through the lattice potential. In such a surface lattice the atoms in the lattice sites are allowed to tunnel only in two directions which is expected to modify the behavior of the system and strongly affect the phase transition. The tunability of the scattering length will be very helpful in changing the interaction energy without affecting the tunneling of the atoms between the lattice sites. Even more ambitious would be a realization of weakly interacting gas in a one-dimensional configuration, i.e. 1D gas “pipes”. Such a gas of “impenetrable bosons”, also called Tonks-Girardeau gas, could be realized at very low densities [Kag87] by using one retro-reflected evanescent wave producing an interference pattern only in one direction. Again, individual 1D gas pipes could be studied in contrast to an average over many similar pipes.

Bibliography

- [And95] M. H. Anderson, J. R. Ensher, M. R. Matthews, C. E. Wieman, and E. A. Cornell, *Observation of Bose-Einstein Condensation in a Dilute Atomic Vapor*, Science **269**, 198 (1995).
- [And97] M. R. Andrews, C. G. Townsend, H.-J. Miesner, D. S. Durfee, D. M. Kurn, and W. Ketterle, *Observation of Interference Between Two Bose-Einstein Condensates*, Science **275**, 637 (1997).
- [Arl98] J. Arlt, P. Bance, S. Hopkins, J. Martin, S. Webster, A. Wilson, K. Zetie, and C. J. Foot, *Suppression of collisional loss from a magnetic trap*, J. Phys. B **31**, L321 (1998).
- [Arn97] M. Arndt, M. B. Dahan, D. Guéry-Odelin, M. W. Reynolds, and J. Dalibard, *Observation of a Zero-Energy Resonance in Cs-Cs Collisions*, Phys. Rev. Lett. **79**, 625 (1997).
- [Ask62] G. Askar'yan, Sov. Phys. JETP **15** (1962).
- [Blo00] I. Bloch, T. W. Hänsch, and T. Esslinger, *Measurement of the spatial coherence of a trapped Bose gas at the phase transition*, Nature **403**, 166 (2000).
- [Bog47] N. Bogoliubov, *On the theory of superfluidity*, J. Phys. **11**, 23 (1947).
- [Bon02] K. Bongs and K. Sengstock, *Introduction to Bose-Einstein Condensation*, in: M. Weidemüller and C. Zimmermann (Eds.), *Interactions in Ultracold Gases*, Wiley-VCH, Weinheim, 2002.
- [Bou94] P. Bouyer, *Confinement par Laser D'Atomes froids dans une cavité Gravitationnelle et dans un piège à pompage optique*, Ph.D. thesis, Ecole Normale Supérieure, Paris (1994).
- [Bou02] I. Bouchoule, M. Morinaga, C. Salomon, and D. Petrov, *Cesium gas strongly confined in one dimension: Sideband cooling and collisional properties*, Phys. Rev. A. **65**, 033402 (2002).

- [Bra95] C. C. Bradley, C. A. Sackett, J. J. Tollett, and R. G. Hulet, *Evidence of Bose-Einstein Condensation in an Atomic Gas with Attractive Interactions*, Phys. Rev. Lett. **75**, 1687 (1995), *ibid.* **79**, 1170 (1997).
- [Bra97] C. C. Bradley, C. A. Sackett, and R. G. Hulet, *Bose-Einstein Condensation of Lithium: Observation of Limited Condensate Number*, Phys. Rev. Lett. **78**, 985 (1997).
- [Cas48] H. B. G. Casimir and D. Polder, *The Influence of Retardation on the London-van der Waals Forces*, Phys. Rev. **73**, 360 (1948).
- [Chi00] C. Chin, V. Vuletic, A. J. Kerman, and S. Chu, *High Resolution Feshbach Spectroscopy of Cesium*, Phys. Rev. Lett. **85**, 2717 (2000).
- [Chi01a] C. Chin, *Cooling, Collisions and Coherence of Cold Cesium Atoms in a Trap*, Ph.D. thesis, Stanford University (2001).
- [Chi01b] C. Chin, V. Leiber, V. Vuletić, A. J. Kerman, and S. Chu, *Measurement of an electron's electric dipole moment using Cs atoms trapped in optical lattices*, Phys. Rev. A **63** (2001).
- [Cor00] S. L. Cornish, N. R. Claussen, J. L. Roberts, E. A. Cornell, and C. E. Wieman, *Stable ^{85}Rb Bose-Einstein Condensates with Widely Tunable Interactions*, Phys. Rev. Lett. **85**, 1795 (2000).
- [Cou96] J.-Y. Courtois, J.-M. Courty, and J. Mertz, *Internal dynamics of multilevel atoms near a vacuum-dielectric interface*, Phys. Rev. A **53**, 1862 (1996).
- [Dal99a] F. Dalfovo, S. Giorgini, L. P. Pitaevskii, and S. Stringari, *Theory of Bose-Einstein condensation in trapped gases*, Rev. Mod. Phys. **71**, 463 (1999).
- [Dal99b] J. Dalibard, *Collisional Dynamics of ultra-cold atomic gases*, Proceedings of the international school of physics "Enrico Fermi" 321 (1999).
- [Dav95] K. B. Davis, M.-O. Mewes, M. R. Andrews, N. J. van Druten, D. S. Durfee, D. M. Kurn, and W. Ketterle, *Bose-Einstein Condensation in a Gas of Sodium Atoms*, Phys. Rev. Lett. **75**, 3969 (1995).
- [Det01] S. Dettmer, D. Hellweg, P. Ryytty, J. Arlt, W. Ertmer, K. Sengstock, D. Petrov, G. Shlyapnikov, H. Kreutzmann, L. Santos, and M. Lewenstein, *Observation of Phase Fluctuations in Elongated Bose-Einstein Condensates*, Phys. Rev. Lett. **87**, 4 (2001).

- [Don01] E. A. Donley, N. R. Claussen, S. L. Cornish, J. L. Roberts, E. A. Cornell, and C. E. Wieman, *Dynamics of collapsing and exploding Bose-Einstein condensates*, Nature **412**, 295 (2001).
- [Ens96] J. R. Ensher, D. S. Jin, M. R. Matthews, C. E. Wieman, and E. A. Cornell, *Bose-Einstein Condensation in a Dilute Gas: Measurement of Energy and Ground-State Occupation*, Phys. Rev. Lett. **77**, 4984 (1996).
- [Fol00] R. Folman, P. Krüger, D. Cassettari, B. Hessmo, T. Maier, and J. Schmiedmayer, *Controlling Cold Atoms using Nanofabricated Surfaces: Atom Chips*, Phys. Rev. Lett. **84**, 4749 (2000).
- [For02] J. Fortagh, H. Ott, S. Kraft, A. Günther, and C. Zimmermann, *Surface effects in magnetic microtraps*, Phys. Rev. A **66**, 041604 (2002).
- [Fri98a] S. Friebe, C. D’Andrea, J. Walz, M. Weitz, and T. Hänsch, *CO₂-laser optical lattice with cold rubidium atoms*, Phys. Rev. A, Rapid Comm. **57**, 4 (1998).
- [Fri98b] D. G. Fried, T. C. Killian, L. Willmann, D. Landhuis, S. C. Moss, D. Kleppner, and T. J. Greytak, *Bose-Einstein Condensation of Atomic Hydrogen*, Phys. Rev. Lett. **81**, 3811 (1998).
- [GO98a] D. Guéry-Odelin, J. Söding, P. Desbiolles, and J. Dalibard, *Is Bose-Einstein condensation of atomic cesium possible?*, Europhys. Lett. **44**, 26 (1998).
- [GO98b] D. Guéry-Odelin, J. Söding, P. Desbiolles, and J. Dalibard, *Strong evaporative cooling of a trapped cesium gas*, Optics Express **2** (1998).
- [Gör01] A. Görlitz, J. Vogels, A. Leanhardt, C. Raman, T. Gustavson, J. Abo-Shaeer, A. Chikkatur, S. Gupta, S. Inouye, T. Rosenband, and W. Ketterle, *Realization of Bose-Einstein Condensates in Lower Dimensions*, Phys. Rev. Lett. **87**, 4 (2001).
- [Gre02] M. Greiner, O. Mandel, T. Esslinger, T. W. Hänsch, and I. Bloch, *Quantum phase transition from a superfluid to a Mott insulator in a gas of ultracold atoms*, Nature **415**, 39 (2002).
- [Gre03] M. Greiner and D. S. J. C. A. Regal, *Emergence of a molecular Bose-Einstein condensate from a Fermi gas*, Nature **537** (2003).
- [Gri00] R. Grimm, M. Weidemüller, and Y. Ovchinnikov, *Optical dipole traps for neutral atoms*, Adv. At. Mol. Opt. Phys. **42**, 95 (2000).
- [Gro61] E. P. Gross, *Structure of a Quantized Vortex in Boson Systems*, Il Nuovo Cimento **20**, 454 (1961).

- [Hak00] H. Haken and H. C. Wolf, *Atom- und Quantenphysik*, Springer-Verlag, Berlin, Heidelberg, New York, 2000, 7th ed.
- [Ham] M. Hammes, *Diploma thesis, University Heidelberg* .
- [Ham02a] M. Hammes, *Optical Surface Microtraps based on Evanescent Waves*, Ph.D. thesis, Universität Innsbruck (2002).
- [Ham02b] M. Hammes, D. Rychtarik, H.-C. Nägerl, and R. Grimm, *Cold-atom gas at very high densities in an optical surface microtrap*, Phys. Rev. A **66**, 051401(R) (2002).
- [Han01a] D. J. Han, M. T. DePue, and D. S. Weiss, *Loading and compressing Cs atoms in a very far-off-resonant light trap*, Phys. Rev. A **63**, 9 (2001).
- [Hän01b] W. Hänsel, P. Hommelhoff, T. W. Hänsch, and J. Reichel, *Bose-Einstein condensation on a microelectronic chip*, Nature **413**, 498 (2001).
- [Har91] S. Haroche, *Fundamental Systems in Quantum Optics*, Proceedings of the Les Houches Summer School (1991).
- [Hen97] C. Henkel, K. Moelmer, R. Kaiser, N. Vansteekiste, C. I. Westbrook, and A. Aspect, *Diffusive atomic reflection at a rough mirror*, Phys. Rev. A **55**, 1160 (1997).
- [Her03] J. Herbig, T. Kraemer, M. Mark, T. Weber, C. Chin, H.-C. Nägerl, and R. Grimm, *Preparation of a Pure Molecular Quantum Gas*, Science **301**, 1510 (2003), published online 21 Aug 2003 (10.1126/science.1088876).
- [Hes86] H. F. Hess, *Evaporative cooling of magnetically trapped and compressed spin-polarized hydrogen*, Phys. Rev. B **34**, 3476 (1986).
- [Hop00] S. A. Hopkins, S. Webster, J. Arlt, P. Bance, S. Cornish, O. Maragò, and C. J. Foot, *Measurement of elastic cross section for cold cesium collisions*, Phys. Rev. A **61**, 032707 (2000).
- [HS82] D. T. und H.L. Stoermer and A. Gossard, *Two-Dimensional Magnetotransport in the Extreme Quantum Limit*, Phys.Rev.Lett **48**, 1559 (1982).
- [Jak98] D. Jaksch, C. Bruder, J. I. Cirac, C. W. Gardiner, and P. Zoller, *Cold Bosonic Atoms in Optical Lattices*, Phys. Rev. Lett. **81**, 3108 (1998).
- [Joc03] S. Jochim, M. Bartenstein, A. Altmeyer, G. Hendl, S. Riedl, C. Chin, J. H. Denschlag, and R. Grimm, *Bose-Einstein condensation of molecules*, Science **302**, 2101 (2003).

- [Kag87] Y. Kagan, B. Svistunov, and G. Shlyapnikov, *Sov. Phys. JETP* **66**, 480 (1987).
- [Kaz73] A. Kazantsev, *Sov. Phys. JETP* **36** (1973).
- [Ket96] W. Ketterle and N. J. van Druten, *Bose-Einstein condensation of a finite number of particles trapped in one or three dimensions*, *Phys. Rev. A* **54**, 656 (1996).
- [Ket99] W. Ketterle, D. S. Durfee, and D. M. Stamper-Kurn, *Making, probing and understanding Bose-Einstein condensates*, in: M. Inguscio, S. Stringari, and C. E. Wieman (Eds.), *Proceedings of the International School of Physics - Enrico Fermi*, 67, IOS Press, 1999.
- [Leo98] P. J. Leo, E. Tiesinga, P. S. Julienne, D. K. Walter, S. Kadlecek, and T. G. Walker, *Elastic and Inelastic Collisions of Cold Spin-Polarized ^{133}Cs Atoms*, *Phys. Rev. Lett.* **81**, 1389 (1998).
- [Leo00] P. J. Leo, C. J. Williams, and P. S. Julienne, *Collision Properties of Ultracold ^{133}Cs Atoms*, *Phys. Rev. Lett.* **85**, 2721 (2000).
- [Lun02] E. Lundh, *Multiply quantized vortices in trapped Bose-Einstein condensates*, *Phys. Rev. A* **65**, 043604 (2002).
- [Man99] I. Manek, *Gravito-optical Surface Trap for Cesium Atoms*, Ph.D. thesis, Ruprecht-Karls Universität, Heidelberg (1999).
- [Mar97] M. Marinescu, A. Dalgarno, and J. F. Babb, *Retarded long-range potentials for the alkali-metal atoms and a perfectly conducting wall*, *Phys. Rev. A* **55**, 1530 (1997).
- [Mas88] N. Masuhara, J. M. Doyle, J. C. Sandberg, D. Kleppner, T. J. Greytak, H. Hess, and G. P. Kochanski, *Evaporative Cooling of Spin-Polarized Atomic Hydrogen*, *Phys. Rev. Lett.* **61**, 935 (1988).
- [Met99] H. J. Metcalf and P. van der Straten, *Laser cooling and trapping*, Springer-Verlag, New York, 1999.
- [Mod01] G. Modugno, G. Ferrari, G. Roati, R. J. Brecha, A. Simoni, and M. Inguscio, *Bose-Einstein Condensation of Potassium Atoms by Sympathetic Cooling*, *Science* **294**, 1320 (2001).
- [Mon90] C. Monroe, W. Swann, H. Robinson, and C. Wieman, *Very Cold Trapped Atoms in a Vapor Cell*, *Phys. Rev. Lett.* **65**, 1571 (1990).

- [Mon93] C. R. Monroe, E. A. Cornell, C. A. Sackett, C. J. Myatt, and C. E. Wieman, *Measurement of Cs-Cs Elastic Scattering at $T = 30\mu K$* , Phys. Rev. Lett. **70**, 414 (1993).
- [Mos99] U. Moslener, *Weiterentwicklung der gravitooptischen Oberflächenfalle (GOST)*, Diploma thesis, Universität Heidelberg and Max-Planck-Institut für Kernphysik (1999).
- [Mul97] W. J. Mullin, *Bose-Einstein Condensation in a Harmonic Potential*, J. Low Temp. Phys. **106**, 615 (1997).
- [Ott01] H. Ott, J. Fortagh, G. Schlotterbeck, A. Grossmann, and C. Zimmermann, *Bose-Einstein Condensation in a Surface Microtrap*, Phys. Rev. Lett. **87** (2001).
- [Ovc91] Y. B. Ovchinnikov, S. Shul'ga, and V. Balykin, *An atomic trap based on evanescent light waves*, J. Phys. B: At. Mol. Opt. Phys. **24**, 3173 (1991).
- [Pet00] D. S. Petrov, M. Holzmann, and G. V. Shlyapnikov, *Bose-Einstein Condensation in Quasi-2D Trapped Gases*, Phys. Rev. Lett. **84**, 2551 (2000).
- [Pet02] C. J. Pethick and H. Smith, *Bose-Einstein Condensation in Dilute Gases*, Cambridge University Press, 2002.
- [Pin97] P. W. H. Pinkse, A. Mosk, M. Weidemüller, M. W. Reynolds, T. W. Hijmans, and J. T. M. Walraven, *Adiabatically Changing the Phase-Space Density of a Trapped Bose Gas*, Phys. Rev. Lett. **78**, 990 (1997).
- [Pit61] L. P. Pitaevskii, *Vortex lines in an imperfect Bose gas*, Sov. Phys. JETP **13**, 451 (1961).
- [Pit03] L. Pitaevskii and S. Stringari, *Bose-Einstein Condensation*, Oxford Press, Oxford, 2003, 1st ed.
- [Raa87] E. L. Raab, M. Prentiss, A. Cable, S. Chu, and D. E. Pritchard, *Trapping of Neutral Sodium Atoms with Radiation Pressure*, Phys. Rev. Lett. **59**, 2631 (1987).
- [RJ01] N. P. R. Jauregui, G. Roati, and G. Modugno, *Anharmonic parametric excitation in optical lattices*, Phys. Rev. A **64** (2001).
- [Rob01a] A. Robert, O. Sirjean, A. Browaeys, J. Poupard, S. Nowak, D. Boiron, C. I. Westbrook, and A. Aspect, *A Bose-Einstein Condensate of Metastable Atoms*, Science **292**, 461 (2001).

- [Rob01b] J. L. Roberts, N. R. Claussen, S. L. Cornish, E. A. Donley, E. A. Cornell, and C. E. Wieman, *Controlled Collapse of a Bose-Einstein Condensate*, Phys. Rev. Lett. **86**, 4211 (2001).
- [Ryc00] D. Rychtarik, *Evaporative Kühlung in der Gravito-optischen Oberflächenfalle*, diploma thesis, Ruprecht-Karls Universität, Heidelberg (2000).
- [Saf98] A. I. Safonov, S. A. Vasilyev, I. S. Yasnikov, I. I. Lukashevich, and S. Jaakkola, *Observation of Quasicondensate in Two-Dimensional Atomic Hydrogen*, Phys. Rev. Lett. **81**, 4545 (1998).
- [Sak94] J. J. Sakurai, *Modern Quantum Mechanics*, Addison-Wesley, 1994, revised ed.
- [Sch01] F. Schreck, L. Khaykovich, K. L. Corwin, G. Ferrari, T. Bourdel, J. Cubizolles, and C. Salomon, *Quasipure Bose-Einstein Condensate Immersed in a Fermi Sea*, Phys. Rev. Lett. **87**, 080403 (2001).
- [SK98] D. M. Stamper-Kurn, M. R. Andrews, A. P. Chikkatur, S. Inouye, H.-J. Miesner, J. Stenger, and W. Ketterle, *Optical Confinement of a Bose-Einstein Condensate*, Phys. Rev. Lett. **80**, 2027 (1998).
- [Söd98] J. Söding, D. Guéry-Odelin, P. Desbiolles, G. Ferrari, and J. Dalibard, *Giant Spin Relaxation of an Ultracold Cesium Gas*, Phys. Rev. Lett. **80**, 1869 (1998).
- [Ste02] D. A. Steck, *Cesium D Line Data*, <http://steck.us/alkalidata> , revision 1.5 (2002).
- [Tak03] Y. Takasu, K. Maki, K. Komori, T. Takano, K. Honda, M. Kumakura, T. Yabuzaki, and Y. Takahashi, *Spin-Singlet Bose-Einstein Condensation of Two-Electron Atoms*, Phys. Rev. Lett. **91** (2003).
- [Vul99] V. Vuletić, A. J. Kerman, C. Chin, and S. Chu, *Observation of Low-Field Feshbach Resonances in Collisions of Cesium Atoms*, Phys. Rev. Lett. **82**, 1406 (1999).
- [Wal92] H. Wallis, J. Dalibard, and C. Cohen-Tanoudji, *Trapping Atoms in a Gravitational Cavity*, Appl. Phys. B **54**, 407 (1992).
- [Web] T. Weber, *PhD thesis, University Innsbruck* .
- [Web02] T. Weber, J. Herbig, M. Mark, H.-C. Nägerl, and R. Grimm, *Tunable Bose-Einstein Condensate of Cesium*, submitted for publication (2002).

- [Web03a] T. Weber, J. Herbig, M. Mark, H.-C. Nägerl, and R. Grimm, *Bose-Einstein Condensation of Cesium*, *Science* **299**, 232 (2003), published online 5 Dec 2002 (10.1126/science.1079699).
- [Web03b] T. Weber, J. Herbig, M. Mark, H.-C. Nägerl, and R. Grimm, *Three-body recombination at large scattering lengths in an ultracold atomic gas*, *Phys. Rev. Lett.* **91**, 123201 (2003).
- [Wen00] M. Wenin, *Adiabatische Phasenraumdichteänderung in einem zeitabhängigen Potential*, Diploma thesis, Universität Innsbruck (2000).
- [Wu96] W.-C. Wu and A. Griffin, *Quantized hydrodynamic model and the dynamic structure factor for a trapped Bose gas*, *Phys. Rev. A* **54**, 4204 (1996).
- [Wyl84] J. M. Wylie and J. E. Sipe, *Quantum electrodynamics near an interface*, *Phys. Rev. A* **30**, 1185 (1984).

Publications

Two-dimensional Bose-Einstein condensate in an optical surface trap

D. Rychtarik, B. Engeser, H.-C. Nägerl, and R. Grimm

Phys. Rev. Lett. in press, cond-mat/0309536

Evanescent-wave trapping and evaporative cooling of an atomic gas at the crossover to two dimensions

M. Hammes, D. Rychtarik, B. Engeser, H.-C. Nägerl, and R. Grimm

Phys. Rev. Lett. 90, 173001 (2003)

Cold-atom gas at very high densities in an optical surface microtrap

M. Hammes, D. Rychtarik, H.-C. Nägerl, and R. Grimm

Phys. Rev. A 66, 051401(R) (2002).

Two-dimensional gas of cesium atoms confined by evanescent wave

M. Hammes, D. Rychtarik, B. Engeser, H.-C. Nägerl, and R. Grimm

In “Interactions in ultracold gases”, Wiley-VCH, edited by M. Weidemüller and C. Zimmermann.

Evaporative cooling of cesium atoms in the gravito-optical surface trap

M. Hammes, D. Rychtarik, and R. Grimm

C.R. Acad. Sci. Paris 2, IV, 625 (2001), proceedings of the Euroconference on “Atom Optics and Interferometry”, Cargèse, Corsica, France, 26 - 29 July 2000, edited by A. Aspect and J. Dalibard.

Optical and evaporative cooling of cesium atoms in the gravito-optical surface trap

M. Hammes, D. Rychtarik, V. Druzhinina, U. Moslener, I. Manek-Hönninger, and R. Grimm

J. Mod. Opt. 47, 2755 (2000), special issue Fundamentals of Quantum Optics V, edited by F. Ehlotzky.

Evanescent-wave cooling of cesium atoms at high densities

M. Hammes, D. Rychtarik, V. Druzhinina, U. Moslener, I. Manek-Hönninger, and R. Grimm

Laser Spectroscopy XIV, edited by R. Blatt, J. Eschner, D. Leibfried, F. Schmidt-Kaler (World Scientific, Singapore, 1999), p. 330.

Danksagung

An dieser Stelle möchte ich mich bei allen bedanken, die zum Gelingen dieser Arbeit beigetragen haben und mir in jener oder anderer Art und Weise Schützenhilfe leisteten:

Rudi, der mich in den letzten fünf Jahren desöfteren aus der Sackgasse führen musste und mich während dieser Zeit hervorragend betreute.

Bastian und Markus, die nicht nur meine tschäschischen Angewohnheiten über sich ergehen lassen mussten, sondern auch lange Messnächte mit mir aushielten oder wie Markus mit mir ein abwechslungsreiches Bergprogramm absolvierte.

Tino für die zahlreichen IT-Beratertätigkeiten und Diskussionen über das Leben danach.

Insbesondere Selim und Cheng for the many fruitful physical discussions.

Gavin and George for the proof-read and making the thesis readable.

und auch alle anderen Jungs aus den Nachbarlabors Jens, Christoph, Michael H&M, Tobias, Markus B., Gerhard, Alexander, Stefan, Johannes, Matthias, Gregor, Klaus, Mattias und Peter für ihre Hilfsbereitschaft und eine äusserst unterhaltsame Arbeitsatmosphäre.

Christine, die mir mit ihrer sehr freundlichen und hifsbereiten Art half alle bürokratischen Hürden zu beseitigen, ebenfalls nicht zu vergessen Frau Moser und Frau Köhle.

Toni und Stefan für technische Unterstützung aller Art.

hlavně mim rodičum, který mi vždy umožnili dělat to, co jsem chtěl a který mi poskytl domov, do kterého jsem se vždy rád vracel.

mé mojce Evulce, která mi otevřela oči a ukázala, že su v životě ešte iné, krajši a dôležitejši věci, a ktorá bola pre mna vždy tu, keď som potreboval.